Materials Science & Engineering R 154 (2023) 100738

Contents lists available at ScienceDirect

Materials Science & Engineering R

journal homepage: www.elsevier.com/locate/mser

Alignment engineering in thermal materials

Bin Xie [a], Weixian Zhao [b], Xiaobing Luo [b,*], Run Hu [b,*]

[a] School of Mechanical Science and Engineering, Huazhong University of Science and Technology, Wuhan 430074, China
[b] School of Energy and Power Engineering, Huazhong University of Science and Technology, Wuhan 430074, China

ARTICLE INFO

Keywords:
Alignment techniques
Advanced thermal functionalities
Microstructures design
Thermal interfacial materials
Radiative cooling
Solar vapor generation

ABSTRACT

Thermal management has become increasingly critical in a broad range of applications, including cooling electronic devices, regulating body temperature, harvesting solar energy, and so on. To achieve effective thermal management, thermal materials are essential platform that enables various thermal functions such as conduction, insulation, radiation, and absorption. However, it remains challenging to tune these properties in thermal materials by traditional mixing strategy. Alignment engineering has emerged as a promising approach for designing and fabricating thermal structures with extraordinary performance, but hasn't been systematically summarized yet. In this review we summarize the recent progress in the emerging field of alignment-engineered thermal materials. The state-of-the-art alignment strategies are introduced, and various thermal materials, including alignment-engineered conductive, insulative, emissive, and absorptive materials, are discussed with emphasis on the correlations between alignment approaches and thermal functionalities, and the dynamic balance between ideal structure and practical engineering. Finally, we outline some perspectives on the challenges and opportunities for alignment engineering toward advanced thermal materials and practical applications.

1. Introduction

The concept of heat has been known for a long time, and heat transfer processes occur all around us, such as cooling a drink with ice, warming ourselves with sunlight, drying hair with hot air, etc [1–3]. Some thermal phenomena are even unnoticed as we go about with our lives. For example, the active thermal management of human body by sweating. This sometimes make us forget how difficult it is to manipulate the heat flux for specific applications, because heat transfer phenomena always occur spontaneously in nature, driven by thermal non-equilibrium [4,5]. Heat manipulation, including heat transfer reinforcement, mitigation, or even reversal, has become a crucial demand for various application areas [6–10]. For instance, for most electronic devices such as smart phones, vehicle electronics, and data servers, heat dissipation enhancement is demanded to maintain a relatively low working temperature for their core components [11–14]. For devices working in extreme environment, such as bathyscaphes and spacecrafts, thermal insulation is strongly needed to prevent their autogenous heat transfer with the surrounding environment [15,16]. For efficient solar energy harvesting, selectively thermal absorption is pursued [17–19]. In addition, for thermal camouflage and radiative cooling purpose in special applications, the pursuit of selective thermal emission has emerged recently [20–23].

To realize above-mentioned supernatural reality, the recent increasing importance of artificial materials (also called "metamaterials") with advanced thermal characteristics, such as enhanced or suppressed thermal conductivity, selective thermal emission, or thermal absorption, are emphasized in both fundamental science and practical needs. Thus, the search for material engineering approaches has greatly promoted the development of fundamental material physics, functional material chemistry as well as applied material engineering. Among various artificial structures, sophisticated but well-ordered structures, i.e., aligned structures, are proven to be effective for purposive heat manipulation. Interestingly, most of the artificially aligned thermal materials can be found in biological organisms or systems, which have been tested by the cruel yet effective "survival of the fittest" rule. For example, thermal conduction materials inspired by spider silk, [24] thermal insulation materials inspired by penguin feathers and polar bear fur, [25,26] and thermal emission materials inspired by Saharan silver ants, [27] etc.

After learned from the amazing complexity of natural materials, researchers have devoted themselves to the engineering of artificial thermal materials, particularly the alignment engineering for realizing highly ordered microstructures with superior thermal properties. As

* Corresponding authors.
E-mail addresses: luoxb@hust.edu.cn (X. Luo), hurun@hust.edu.cn (R. Hu).

https://doi.org/10.1016/j.mser.2023.100738
Received 1 March 2023; Received in revised form 9 May 2023; Accepted 9 May 2023

shown in Fig. 1, numerous alignment approaches including the mechanical force-based alignment, [28–31] template-assisted alignment, [32–35] and 3D printing-based alignment have been proposed [36–39]. With these techniques, distinct thermal purposes were realized. Thus, in this review, the research overviewed falls into one of the following four thermal management aspects that are realized by alignment engineering:

Thermal conduction. The increasing power consumption and ever-shrinking size in modern electronics have triggered rising demand for effective heat dissipation at the material level. In the heat transfer route, interfaces between constituent materials are critical because they induce interfacial phonon scattering as well as air gaps, resulting in severe thermal resistances [40,41]. Therefore, thermal interfacial materials (TIMs) which consist of polymer matrix and thermally conductive fillers, are filled in these interfaces for thermal conduction promotion [42]. Fabricating an effective TIM is quite challenging. To realize efficient heat dissipation, as many as highspeed heat conduction pathways that are parallel to the heat dissipation direction should be established within these materials. For this purpose, we emphasis two alignment strategies for making a high-performance thermal conduction material. One is to align polymer chains themselves [43–45]. For example, the chain-aligned PE films with thermal conductivity up to 62 $Wm^{-1}K^{-1}$. [45] The other is to align thermally conductive fillers within polymer matrix [46–48]. For example, the horizontally aligned graphene framework which leads to directional thermal conductivity of 117 $Wm^{-1}K^{-1}$ [48].

Thermal insulation. Featuring opposite purpose with thermal conduction, thermal insulation is to prevent any spontaneous heat transfer process between an object and its surroundings. To achieve excellent thermal insulation, all the heat transfer phenomena including conduction, convection, and radiation, should be blocked [49,50]. In this aspect, we focus on the thermal insulation materials with well-aligned thermal barriers along the heat flow direction, including 1D-aligned fibrous structures, 2D-aligned hierarchical structures, and 3D-isolated porous structures. For example, thermal insulators with ultralow thermal conductivity achieved by aligned porous fibers, [51] lamellar-structured ceramic aerogels, [52] and graphene-based closed-cellular foams, [53] etc.

Thermal emission. Every object with temperature above 0 K emits and perceives infrared (IR) radiation to/from its surroundings. With this unique feature, thermal emission process can be utilized for the purposes of communication, detection, camouflage, thermal management, etc. Currently, IR camouflage and IR radiative cooling are undoubtedly the most attractive applications for thermal emission engineering. IR camouflage, which helps to disguise or hide an object in the background, can be realized by engineering either the surface emissivity or temperature field of objects [54,55]. IR radiative cooling is a passive yet energy-efficient cooling technology to maintain lower temperature of an object by enhancing its IR emissivity within the transparency window. [56–58] We found that alignment approaches are widely adopted in these applications to realize selective thermal radiation, such as the alignment of surface texture, [27] meta-fibers, [59] and polymer-ceramic composite with micro-hump profiles [60].

Thermal absorption. Efficient solar energy harvesting is valuable for many applications, such as solar energy storage, [61,62] solar vapor generation, [63–67] and biomedical applications [68–71]. To achieve remarkable photo-thermal conversion, materials with strong solar energy absorption as well as heat confinement characteristics are of great significance. Among various thermal absorbing materials, those with aligned nanostructures have shown their potential in efficient light-to-heat conversion, such as single-directional aligned porous

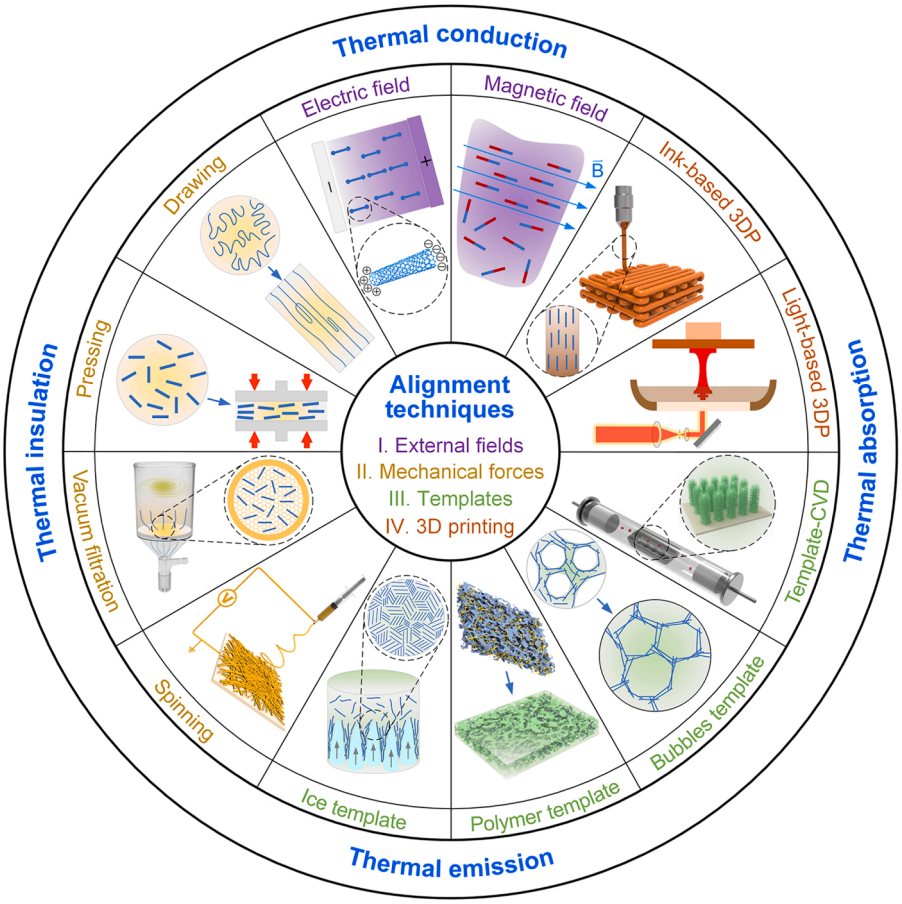

Fig. 1. Alignment techniques for fabricating advanced materials with various thermal functions.

structures, [72] aligned micro-funnel structures, [73] and template-derived aligned plasmonic channels [74].

Overall, in the above-mentioned thermal applications, alignment engineering plays a prominent role for tuning the specific properties of artificially thermal materials. In this review, we start with an introduction of fundamental design and fabrication strategies of alignment engineering for advanced thermal materials. Then, we discuss the specific thermal applications of aligned thermal materials, and the state-of-art emerging applications of alignment-based thermal manipulation. This is a domain in which significant progress has been achieved in the past few decades but has not been reviewed systematically. By this review, we hope to push forward the detailed understanding of alignment mechanisms and facilitate the development of emerging thermal applications.

2. Alignment techniques for thermal materials

To realize exceptional thermal properties that are rare to find in traditional metals, ceramics and polymers, the architecture of single or composite material, which is the combination of distribution, orientation, and continuity design, is critical for realizing desired thermal functions of materials. Specifically, distribution design can be divided into homogenous and non-homogenous types. Orientation control of anisotropic zero-dimensional (0D) nanoparticles, one-dimensional (1D) nanotubes/nanowires, and two-dimensional (2D) nanosheets is a key process to realize selective thermal response to external stimuli. Continuity design determines the scale of thermal interaction between reinforcements and matrix. Therefore, architecture design provides a bridge for microscale structures and the macroscale performances. In this section, alignment techniques for building multi-level aligned structures were introduced and discussed, as illustrated in Fig. 1.

2.1. External fields assisted alignment

Electric field. An electric current has the potential of controlling the structure of electrically conductive materials, since the transport of atoms, ions, and holes in a material can be controlled through electrophoresis [75]. Therefore, electric field can be utilized to arrange the alignment and distribution of electrically conductive filler networks. Usually, some electrically conductive fillers such as metals and carbon-based derivates (carbon nanowire/nanotube, graphene, etc.) also feature superior thermal conduction properties [29,76,77]. Thus, the alignment of these thermally conductive materials can be realized by applying electric field. Fig. 2a shows the schematic setup of electric

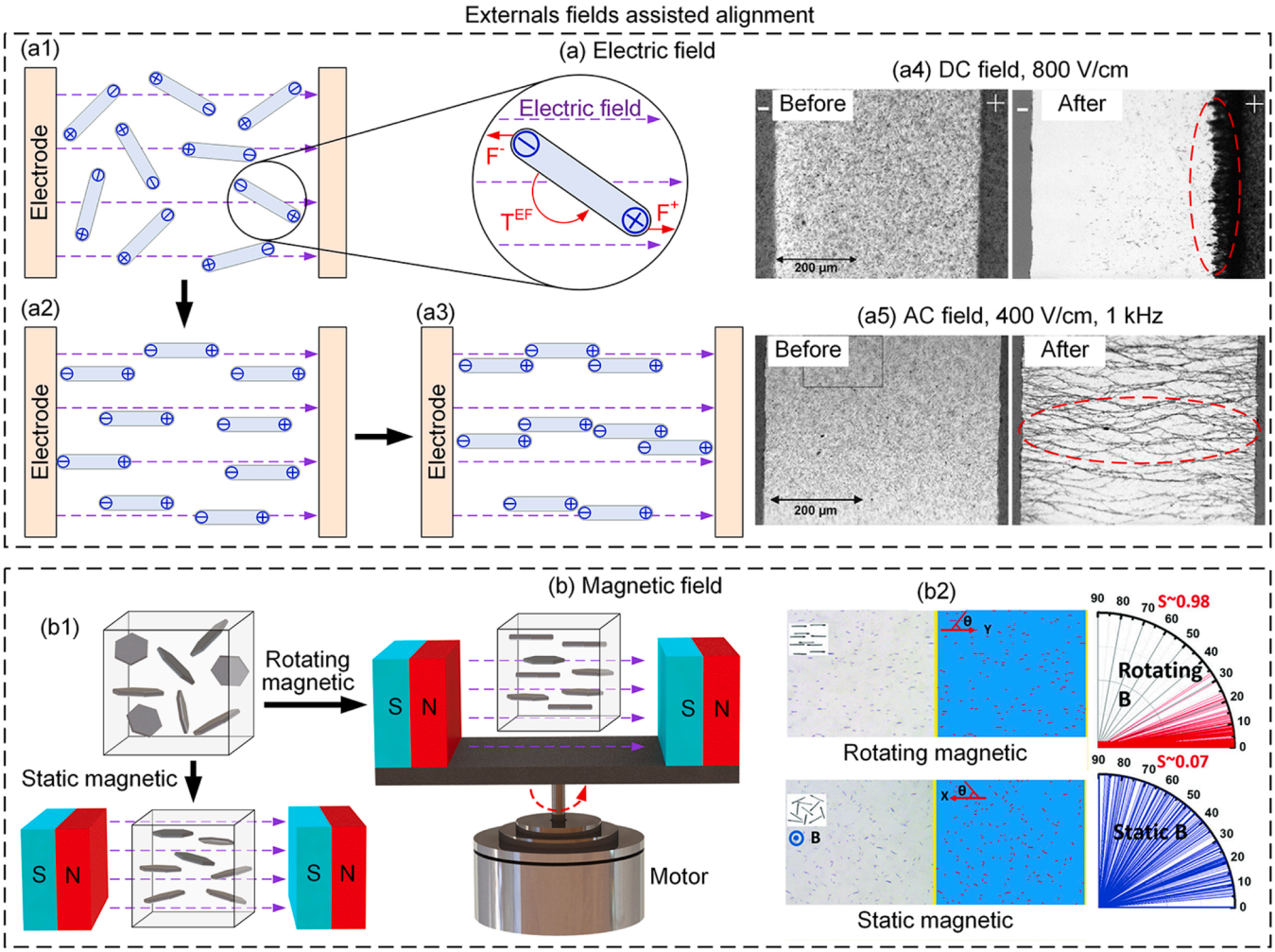

Fig. 2. a) Electric field-induced alignment. a1-a3) indicate the fillers alignment processes under electric field. a4) Electrophoresis of 0.2% CNF dispersed in amine curing agent before and after 17 min treatment of a DC electric field of 800 V/cm. a5) Alignment of 0.2% CNF dispersed in amine curing agent before and after 30 min treatment of an AC electric field of 400 V/cm and 1 kHz. b) Magnetic field-induced alignment. b1) indicates the fillers alignment under static magnetic and rotating magnetic. b2) Microscopic images and polar histograms of rotating angle of graphene aligned with rotating (upper) and static (lower) magnetic field. The order parameter (defined as $S = < 2\cos^2\theta\text{-}1 >$) of graphene in the rotating field reaches 0.98, which is higher than that in static field (0.07).
(a) Reproduced with permission [80]. Copyright 2003, Elsevier. (b) Reproduced with permission [102]. Copyright 2018, Wiley-VCH.

field-assisted alignment of filler network. Typically, a voltage is applied to the mixture of matrix and fillers, where the fillers are randomly distributed and oriented. When an electric field is applied, the filler will be polarized, resulting in a redistributed surface charge near the filler ends. With the driving force of the electric field torque (T^{EF}), the charged fillers gradually rotate toward the direction paralleling with the electric field, and some fillers move closer toward each other due to their opposite surface charges, forming an interconnected bundle. In the meantime, in-situ curing of the matrix induce the formation of cross-linked filler network. Electric field-induced alignment of fillers can be conducted either by direct current (DC), [78] or alternating current (AC), [79] whereas the influence of DC or AC on the assembly of fillers is different. The DC field results in the physical movement of charged fillers in the direction paralleling to the surface under the electrophoresis effect. Consequently, the fillers aggregation occurs at the electrode surface carrying the opposite charge to that on the filler surface (Fig. 2a4). The AC field usually results in an aligned filler network formed between the electrodes, driven by the frequency-dependent dielectrophoresis and orientation phenomena (Fig. 2a5). [80] There are three types of motion when fillers are under an AC field, namely rotation, translation, and migration. Rotation indicates the orientation of filler's longitudinal axis parallel to the direction of electric field, which is caused by the anisotropic electric polarizability of filler. When applying an electric field, a dipole is created at the ends of filler because of the shift of charge, and a torque is then created by the electric field that leads to the rotation of filler. Translation refers to the offset of a filler due to the tail-to-head attraction by another adjacent filler. This is the most critical motion for building percolated filler network within the matrix, even under an extremely low filler concentration of 0.002 wt%. [81] Migration is easily observed under a DC field where the charged fillers move toward the electrode featuring the opposite charge. [82] When the fillers are close enough to the electrode to allow charge transfer, they discharge and then aggregate onto the electrode. Further, tips of fillers on the electrode surface function as high electric field sources and locations for absorbing more fillers. Consequently, dendritic filler network structures are formed around the electrode.

There are two main points of focus in the electric-field assisted alignment of fillers, one is the effective movement of fillers, and the other is the anti-agglomeration during the movement of fillers. Remillard et al. provided an overview of various parameters that may influence the fillers' movement phenomenon of electric field-assisted alignment, [83] such as the electrode material and spacing, the filler type and concentration, the matrix material, the electric field voltage and frequency, and the exposure time to the electric field. Because of the wide variety in experimental designs, it is hard to conclude an optimal experimental condition for all electric field-based system. However, some qualitative design principles can be summarized for efficient alignment of fillers by electric field. In all cases, the polarizing force induced by the electric field (F_{EF}) is the most influential parameter for filler alignment. F_{EF} is proportional to the gradient of the electric field, the matrix permittivity, and the electrophoretic polarization of the filler. Therefore, increasing the applying voltage, choosing matrix with high permittivity and filler with high polarization are beneficial for efficient filler alignment. Although polarizing force provides the driving force, additional factors such as matrix viscous drag, matrix advection and filler inertia can also influence the final distribution of the fillers. For AC electric field, a higher frequency helps to form a filler network with higher degree of alignment, dispersion, and uniformity within less time duration [79]. Besides, increasing the filler concentration can also increase the overall filler alignment, since the formation of dipoles in individual filler also induces the polarization of neighboring filler [84]. Despite successful alignment under appropriate electric field conditions, the fillers still facing the issue of agglomeration in the matrix, especially under high filler concentration. [85] To solve this issue, two solutions were proposed. One is the surface chemical modification of filler by introducing functional groups onto the filler surface. As an example, Ma et al. demonstrated that the oxidization of multi-wall carbon nanotubes (MWCNTs) not only prevent the filler agglomeration but also enhance the alignment of MWCNTs in polymeric matrices under AC electric field. [86] The other solution is to cure the composites immediately after the aligned filler network is formed, so that the aligned fillers are fixed before agglomeration. For example, Park *et al.* proposed an electric field-assisted alignment system with in-situ light curing subsystem. [87] The cured composites with aligned single-wall carbon nanotube (SWCNT) demonstrates outstanding improvement in electric conductivity and dielectric property. Zhu et al. also validated the effectiveness of fast curing method on freezing the lateral aligned CNT network to some extent [84].

Magnetic field. Similar with electric field, magnetic field also has the ability of manipulating the orientation and distribution of fillers. [88] Theoretically, all materials respond to magnetic field, and atomic scale magnetic moments are generated inside the material, which are originated from both the orbital motion of electrons around the nuclei and the spin of electrons themselves. Nuclei spin also contributes to magnetic moment, while this moment is much less than that of electron spin and electron orbital motion due to the relatively large mass of nuclei [89]. The time and space average of the magnetic moments within a material is defined as its magnetization. Under the effect of magnetic field, the magnetic moments torque generated in each atom may cause a tendency for parallel or anti-parallel alignment of the magnetic moments with the external magnetic field, and the material presents a net magnetization. This behavior can be utilized to distinguish the paramagnetic materials and diamagnetic materials. Fig. 2b shows the schematic setup of magnetic field-assisted alignment of filler network. However, conventional diamagnetic and paramagnetic materials show low magnetic susceptibly which is far from enough to driven them responsive to the applied magnetic field. In other words, a large magnetic field (nearly 1 T) is needed to drive certain diamagnetic or paramagnetic fillers. [88] Recently, an attractive solution is to decorate the fillers with superparamagnetic nanoparticles such as iron oxides, [90, 91] irons, [92] cobalt, [93] manganese, [94] and nickel, [95] etc., so that the modified fillers can be manipulated with small magnetic fields in magnitude of mT. These superparamagnetic nanoparticles are usually functionalized by a surfactant and suspended in a base fluid such as water to form a ferrofluid. [96,97] The combination of filler and superparamagnetic nanoparticles can be realized by an electrostatic self-assembly process, in which the ferrofluid is positively charged and the fillers are negatively charged. [98].

After solving the magnetic response issue of fillers, the applied magnetic field should also be carefully designed. Static and rotating magnetic field are adopted by researchers for fillers alignment [99–101], of which the former can be realized by static magnet and the latter by either rotating magnetic field (via magnet rotation or sample rotation) or Helmholtz coil system. [102,103] A static magnetic field can be utilized for assembling nanoparticle fillers. When a magnetic field is on, it induces magnetic moments in fillers $m = \chi HV$, where χ is the magnetic susceptibility of the filler, H is the magnetic field strength, and V is the filler volume, respectively. Then, magnetic force is generated between two fillers, which finally assemble the particles into chains paralleling with the external magnetic field. By applying prolonged time, this approach can produce scalable and complex nanostructures. While, when the external magnetic field is turned off, the assembly of nanostructures may return unordered. A simple but effective solution for this issue is to cure the matrix immediately after the alignment. Besides, functionalizing the magnetic nanoparticles with polymers such as polyethyleneimine (PEI) can also lock the aligned chains of magnetic nanoparticles, and thus retain the ordered structure even if the field is switched off. [104] In a rotating magnetic field, the fillers are easily oriented and aligned because their least magnetically susceptible axis (namely the hard axis) becomes parallel to the axis of rotation of the magnetic field. As displayed in Fig. 2b2. [102] Frenkel has shown for the first time that a magnetic nanoparticle rotates synchronously under

uniform magnetic field with a specific range of the external magnetic field frequency f, and the nanoparticles stop rotating at some critical frequency f_c. [105] Therefore, by designing the rotating frequency of external magnetic field, some aligned nanostructures that are difficult to obtain by static field can be realized by applying the rotating field. Compared with electric field, magnetic field has greater ability to penetrate materials, thus can be utilized to manipulate target materials from a distance in a non-contact manner. In addition, the chemical cleanliness of magnetic field enables the non-contact and non-destructive application over a prolonged time. However, the drawback to this method is the rapid drop of the magnetic strength on the macroscopic scale. Consequently, the alignment can only be

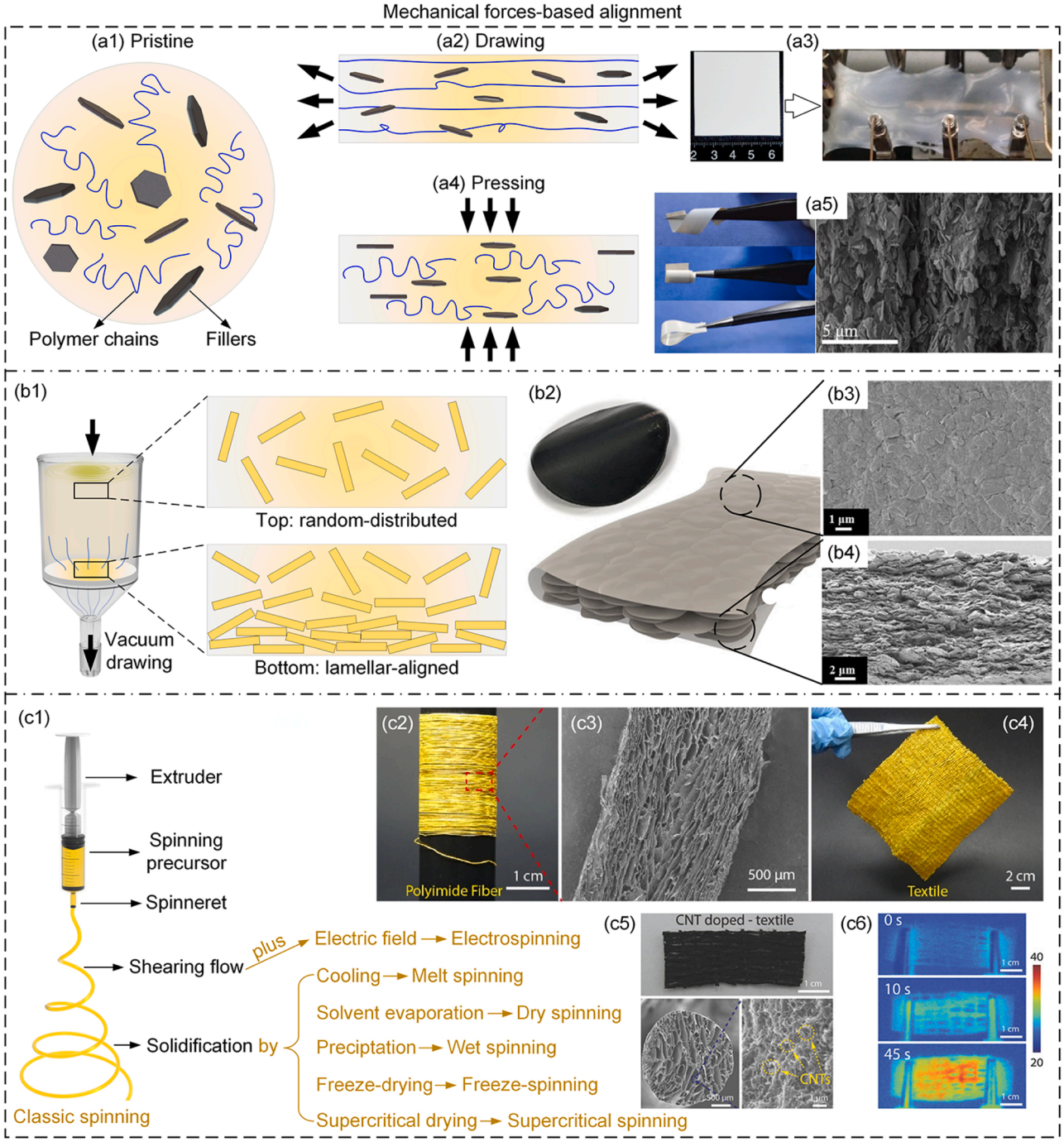

Fig. 3. Mechanical forces-induced alignment. a1) Schematic showing the pristine state of polymer composites. a2) Schematical illustration of polymer composites under drawing process. a3) A PE/BN film prepared by extruding the mixed powders of PE and BN, and the PE/BN film undergoing uniaxial drawing. a4) Schematic showing the polymer composites under pressing process. a5) Photographs and SEM image of a hot-pressed PVA/BN film. b2) Photograph and schematic diagram of a fluorinated graphene/PVA film prepared by VAF. b3) and b4) display the SEM images of this film from top- and side-view, respectively. c1) Schematic diagram of various spinning techniques. c2-c4) Photographs and SEM image of a thermally insulating PI fiber/textile obtained by the freezing-spinning technique. c5) Photograph and SEM images of a CNT-doped silk textile by freezing-spinning. c6) Infrared images of the CNT-doped textile during the heating process.
(a) Reproduced with permission [110]. Copyright 2020, Elsevier. (b) Reproduced with permission [116]. Copyright 2021, Elsevier b1) Schematic showing the VAF process. (c) Reproduced with permission [123]. Copyright 2019, American Chemical Society. (d) Reproduced with permission [151]. Copyright 2020, Elsevier. (e) Reproduced with permission [51]. Copyright 2018, Wiley-VCH.

controlled at distances no longer than ~15 cm from the magnet, although this is not a critical limit for many applications.

2.2. Mechanical forces assisted alignment

Mechanical shear forces are powerful in driving the alignment of thermal materials, including both fillers and polymer matrices. [106–108] In practice, thermal material alignment through mechanical force is mainly realized by drawing, hot-pressing, vacuum assisted filtration, and spinning. The alignment mechanisms of these strategies are discussed as follows.

Drawing. Drawing (or stretching) has been proven simple but robust for aligning both polymer chains and thermal fillers. [109,110] The shear force provided by the stretching process helps reducing the entanglements between polymer chains and creating ordered nanostructure. Recently, metal-like thermal conductivity of polymer materials achieved by the stretching approach were frequently reported, such as the ultra-drawn polyethylene (PE) nanofibers with thermal conductivity of 104 $Wm^{-1}K^{-1}$and lengths up to tens of millimeters, [108] the stretched ultrahigh molecular weight film with thermal conductivity as high as 65 $Wm^{-1}K^{-1}$, [109] and the scale-up PE films with thermal conductivity of 62 $Wm^{-1}K^{-1}$, [45] etc. Although the precise mechanism that govern the thermal conductivity in these polymers remain poorly understood, it is a consensus that such a high thermal conductivity is attributed to the restructuring of the polymer chains along the stretching direction, which improves the fiber quality toward an ideal single-directional aligned fiber, as illustrated in Fig. 3 a1, a2. Therefore, the stretching ratio plays a critical role in this approach. According to past efforts of morphological studies on the stretched polymers, [111, 112] in the initial stretching process where the stretching ratio is low, small crystalline blocks gradually transfer into microfibrils along the stretch direction. In this stage, the crystalline blocks are stacked and interconnected by taut tie molecules which originate from the partial unfolding of polymer chains. With further stretching, the microfibrils turn into fully extended interfibrillar tie molecules, and finally lead to extended chains. The growing extended chains volume fraction will form a larger average crystal size, which will enhance the thermal properties of polymer samples. Even after a stretch ratio of 110, there was still no sign of saturation in the increase of thermal conductivity, suggesting the huge room for further conductivity enhancement by this method [45]. Despite these promising results, the extremely thin nanofibers or films produced at very high stretch ratios may limit their applications in practical mass manufacturing. Stretching approach can also be utilized for aligning the thermal fillers in composite materials. During the stretching process of composite materials, both the polymer chains and thermal fillers aligned along the stretching direction, resulting in oriented lamellae nanostructures. Due to the incorporation of thermal fillers, the stretched composite materials can achieve a metal-like thermal properties under a rather low stretch ratio than that of polymers [113]. For example, under a boron nitride nanosheets (BNNS) fraction of 15 wt% and stretching ratio of 5, the PE/BNNS nanocomposite films achieved an extremely high thermal conductivity of 106 $Wm^{-1}K^{-1}$ (Fig. 3 a3), [110] which demonstrates the immense potential of the stretching approach for the scalable production of cost-effective, high-performance thermally conductive composites materials.

Pressing. Similar with stretching approach, hot-pressing is another highly efficient approach to achieve aligned fillers whose direction are perpendicular to the pressing direction. The alignment is mainly realized through the repetitive stacking of limited fillers, and the shear force provided by the flowing of melting polymer matrix under high temperature and high pressure. [114,115] Besides, the high pressure eliminates internal pores and results in a densely packed composites, which is beneficial for the interconnection of filler-filler and filler-polymer, thus further improve the thermal as well as mechanical performance of composite materials. By using the hot-pressing strategy, researchers have fabricated various thin film composites with high in-plane thermal conductivity. For example, the polyvinyl alcohol (PVA)/BNNS composites film with in-plane thermal conductivity of 19.99 $Wm^{-1}K^{-1}$ and thickness of 30 μm at BNNS fraction of 40 wt%, [116] the aligned graphite flakes/Cu foil composites with in-plane thermal conductivity of 741 $Wm^{-1}K^{-1}$ at graphite flakes fraction of 70 vol%, [117] the Graphitized blocks with 86 wt% natural graphite and 14 wt% mesophase pitch with in-plane thermal conductivity of 522 $Wm^{-1}K^{-1}$, [118] etc. One remarkable advantage of this method is, by controlling the solution concentration and filler feeds, the filler incorporation fraction in the composite can reach an extremely high level (up to 95 wt%), [107] while keeping the mechanical flexibility of composite film. This characteristic is hardly attainable by using other external-field-assisted alignment approaches like magnetic field or electric field, because the external force is unable to conquer the huge moving resistance caused by the overloaded fillers. Generally, a higher hot-pressing pressure exerted on the composite motivates the rearrangement and orientation of fillers along the in-plane direction and decreases the distance of adjacent fillers, which enhance the thermal properties. however, for the hot-pressing temperature, it is found that an optimal temperature exists around the glass transition temperature point of polymer matrix, which contributes to the highest thermal transport ability of composite materials [119].

Vacuum assisted filtration (VAF). Filtration method has been developed in an early time, to align multiwalled carbon nanotubes (WCNTs) which showed strongly anisotropic properties [120]. As displayed in Fig. 3 b1, the components needed for establishing the filtration system are quite simple, including a filtration membrane, a vacuum pump, and a container. Under the continuous vacuum pumping, the diluted, surfactant-based suspension of randomly-distributed fillers pass through the membrane, and leave the fillers on the membrane surface, forming a homogeneous and lamellar-aligned filler network on the membrane. After washing away the surfactant, the fillers can be transferred to the desired substrate by multiple techniques. [121] The VAF approach has several advantages. Firstly, the thickness of film is easily controlled by the filler concentration and volume of the suspension. Secondly, the homogeneity of the film can be guaranteed by the filtration itself. Since the filtrated fillers act as a filter cake to impede the permeation rate, while there is a thicker region, their local permeation rate and associated deposition rate slow down, resulting in a balance of thickness. When aligning 2D fillers such as boron nitride nanosheets or graphene, [122, 123] the filtration process can be roughly conducted, since the fillers always tend to lie flatly on the membrane surface due to the shearing flow and gravity, and the in-plane orientation of fillers has neglectable influence to the thermal properties of the final film. Even with high filler content, the 2D fillers can still be well-aligned. As demonstrated by Wang et al., a fluorinated graphene/PVA film with 93 wt% of graphene still shows a well-organized brick-and-mortar structure in the in-plane direction (Fig. 3 b2-b4), with a thermal conductivity of 61.3 $Wm^{-1}K^{-1}$. [123] Whereas, for the alignment of 1D fillers such as nanowires or nanotubes, [124–126] the filtration process should be carefully designed, since the in-plane alignment of fillers also contribute greatly to the final performance of the film. He *et al.* adopted a slow-VAF approach to fabricate the highly packed CNTs film where the CNTs are rigidly aligned within $\pm$ 1.5°. [127] They also found that the ideal alignment of CNTs is influenced by several critical factors, such as the filter membrane surface charge, the concentration of surfactant, the concentration of CNTs, and the filtration speed. Detailed discussion of all these factors is not overviewed here. However, one critical factor should be highlighted, i.e., the surface charge properties of the filter membrane. If the surface of fillers and membrane feature like charges (both negative or positive), the fillers would face an energy barrier due to the electrostatic repulsion from the approaching membrane surface. In the same time, the fillers also attracted by the surface due to van der Waals forces from the surface. Thus, the competition between these two forces will create a potential well near the membrane surface where

fillers are confined in a narrow layer and an ordered 2D alignment appears [128]. We believe this mechanism will open new door for the ideal alignment of 1D fillers. On the other hand, the VAF features the disadvantage of time-consuming, especially when polymers are involved or thick films are desired, which makes it less attractive for industrial applications than other approaches. Besides, the viscosity of suspension must be controlled at a low level to allow efficient filtration. Thus, only polymers with low-molecular weight are applicable for the VAF process, such as the polyvinyl alcohol (PVA), [129,130] Chitosan, [131] Sodium alginate (SA), [132] poly(diallyldimethy lammonium chloride), [133] and polyurethane (PU) [134].

Spinning. Spinning is a shear-flow based method for producing synthetic, cellulosic fibers or thin films with anisotropic characteristics. As depicted in Fig. 2 c1, there are various spinning techniques, including melt spinning, [135] dry spinning, [136] wet spinning, [137] dry-wet hybrid spinning, [138] and electrospinning, [139,140] which are divided by the variation of their application purpose and raw-material properties (such as the melting point, melt stability, and solubility in solvents). Generally, the raw-material is first molten or dissolved to produce a spinning precursor. Then, the precursor is extruded through a spinneret to produce a high shearing flow, which enable the directional alignment of polymer chains (and/or fillers). Finally, the extruded filaments are solidified by means of cooling, solvent evaporation, or precipitation in an antisolvent, which are referred to as melt-, dry-, and wet-spinning, respectively. While, for an electrospinning process, a viscos suspension of polymer molecules dissolved in solvent (with or without fillers) is fed to the tip of a sharp syringe needle, and a high voltage is applied between the needle and a grounded collector. Due to the influence of the strong electric field, the suspension forms a Taylor cone from which a jet is accelerated towards the grounder collector. Due to the large surface area to volume ratio of the jet, the solvent evaporates quickly and leaves a solid fiber on the collector surface. [141] The spinnability, which indicates the filament forming ability of a precursor, is affected by several factors, such as flow behavior, rheology, crystallization, melt flow index, phase transition, and structure development. Choosing an optimal spinning technique requires consideration of both the spinnability and intended application. For example, the synthetic polymers such as polyester (PET), [142] PE, [143] polyamide (PA, nylon), [144] and polypropylene (PP) [145] are typically melt-spun, which is based on a simple extrusion process without the participation of solvent, but it requires melt processability of precursor. For the alignment of cellulose derivatives such as cellulose nanofibrils (CNF) that can be dissolved in various solvents, dry-spinning and wet-spinning are the mostly used techniques. [146,147] While, electrospinning can be adopted to align any polymers as long as they can be dissolved or melted, though an extra electric field is needed. By using above-mentioned spinning approaches, researchers always obtained aligned thermal materials with reinforced thermal transport properties. Recently, by replacing the conventional drying process of these spinning techniques with freeze-drying [148,149] or supercritical drying, [150] aerogel fibers with aligned pores along the fiber axis could be fabricated, which is difficult to achieve by other methods. For instance, a textile woven with such a 'polar bear hairs'-like polyimide (PI) fibers shows excellent thermal insulation property and good breathability (Fig. 3 c2-c4). [151] It is seen that well-aligned pores are obtained in the fiber by freeze-spinning, and a large piece of textile (~100 cm^2) are woven with the as-prepared PI fiber, reflecting its potential for scalable fabrication. Moreover, after doped with other electro heating materials such as CNTs (Fig. 3 c5), these textiles can also work as a wearable heater to realize fast and uniform electro-heating, which can make a temperature rise of ~12 ℃ within 45 s under an applied voltage of 5 V (Fig. 3 c6). [51].

2.3. Template-directed alignment

Ice-templated alignment. Ice-templating is also known as directional freeze-casting, which introduces ice crystals as templates to align fillers in an aqueous solution into macroscopic network with controlled morphology. There are two kinds of ice-templating, namely the unidirectional freeze-casting (UFC, Fig. 4 a1) and bidirectional freeze-casting (BFC, Fig. 4 a2), depending on the number of temperature gradients created in the system. The UFC approach was first proposed to develop sophisticated porous and layered-hybrid materials inspired by natural species such as nacre. [152] Typically, to create a temperature gradient, the UFC system contains a cold metal finger whose temperature is controlled by a liquid nitrogen bath, and the aqueous slurry involving fillers is placed onto the cold finger. As a result, a constant temperature gradient is formed in the vertical direction from lower to upper, and then drives the ice crystals growth along this direction. Simultaneously, the fillers will be trapped by the moving ice-crystals front as well as aligned in the vertical direction. Under steady-state conditions, the ice crystals from a lamellar microstructure, with the lamellae thickness depending mainly on the speed of the freezing front. After freezing, the ice template is removed by freeze-drying under low temperature and pressure, such that a scaffold that negatively replicate the microstructure of ice crystal is produced. Thus, by controlling the anisotropic growth kinetics of ice crystals, it is flexible to build homogeneously scaffolds with long-range aligned filler microstructure. A wide range of 1D and 2D fillers such as nanowires, [153,154] nanotubes, [155] graphene derivatives, [156, 157] and nanoplatelets, [158,159] can be assembled into composites with two methods, i.e., the in-situ method and the *ex-situ* method. In the in-situ method, the fillers and polymer resin/monomer are premixed in an aqueous solution, followed by freeze-casting, while in the *ex-situ* method, the fillers in an aqueous solution are first freeze-casted into a porous skeleton, followed by infiltration of polymer. Due to the single temperature gradient created by the UFC, alignment can be only achieved along a single direction (the ice growth direction), and the fillers in other directions are randomly distributed because of the random nucleation of ice crystals.

On the basis of UFC, the BFC method was developed by creating an extra temperature gradient to allow the formation of ice crystals along two directions. The BFC setup can be easily established base on the typical UFC system, for example, by placing a polydimethylsiloxane (PDMS) wedge onto the cold finger. [160] Fig. 4 a3, a4 show the typical morphology of nanocomposites prepared by these two methods, where highly ordered lamellar structures were created by BFC with the growth of ice crystals along two orthogonal directions, due to the existence of dual temperature gradients. [161] Different from the randomly distributed nanostructures in the transverse direction created by UFC, the BFC created large domains of long-range ordered lamellar nanostructures in both longitudinal and transverse directions. [162] It is worth mentioning that by carefully designing the second temperature gradient of BFC, other fascinating aligned structures can be obtained. For example, Wang et al. reported on a radially aligned graphene oxide (GO) aerogel by using a copper mold with radial structures. [163] This methodology can be easily expanded to other configurations, and many other ice-templated nanostructures that are coupled with special thermal purposes (such as the targeted cooling) can be achieved.

To precisely control the final morphology of aligned nanostructures by freeze-casting, main parameters including size of fillers, the binders, and the freezing kinetics of ice crystals should be engineered. Generally, small fillers are disadvantageous for being entrapped and aligned by the moving ice crystals front [152]. As an illustration, unidirectional graphene aerogels (UGAs) prepared using ultra-large GO (UL-GO) shows better alignment and properties than those made from small GO (S-GO) [164]. In most cases, binders are necessary for maintaining the mechanical strength of aerogels prepared by freeze-casting, especially for those made with small-size fillers. Sodium carboxymethylcellulose (SCMC), [165] PVA, [159] PU, [161] or GO [166] can be adopted as binders to obtain highly stable aerogels. Besides, the freezing kinetics of ice crystals determines the wall thickness and pore size of the obtained nanostructures, which can be engineered by tuning the freezing temperature, [167] by adding antifreezes, [168] or by varying the type and

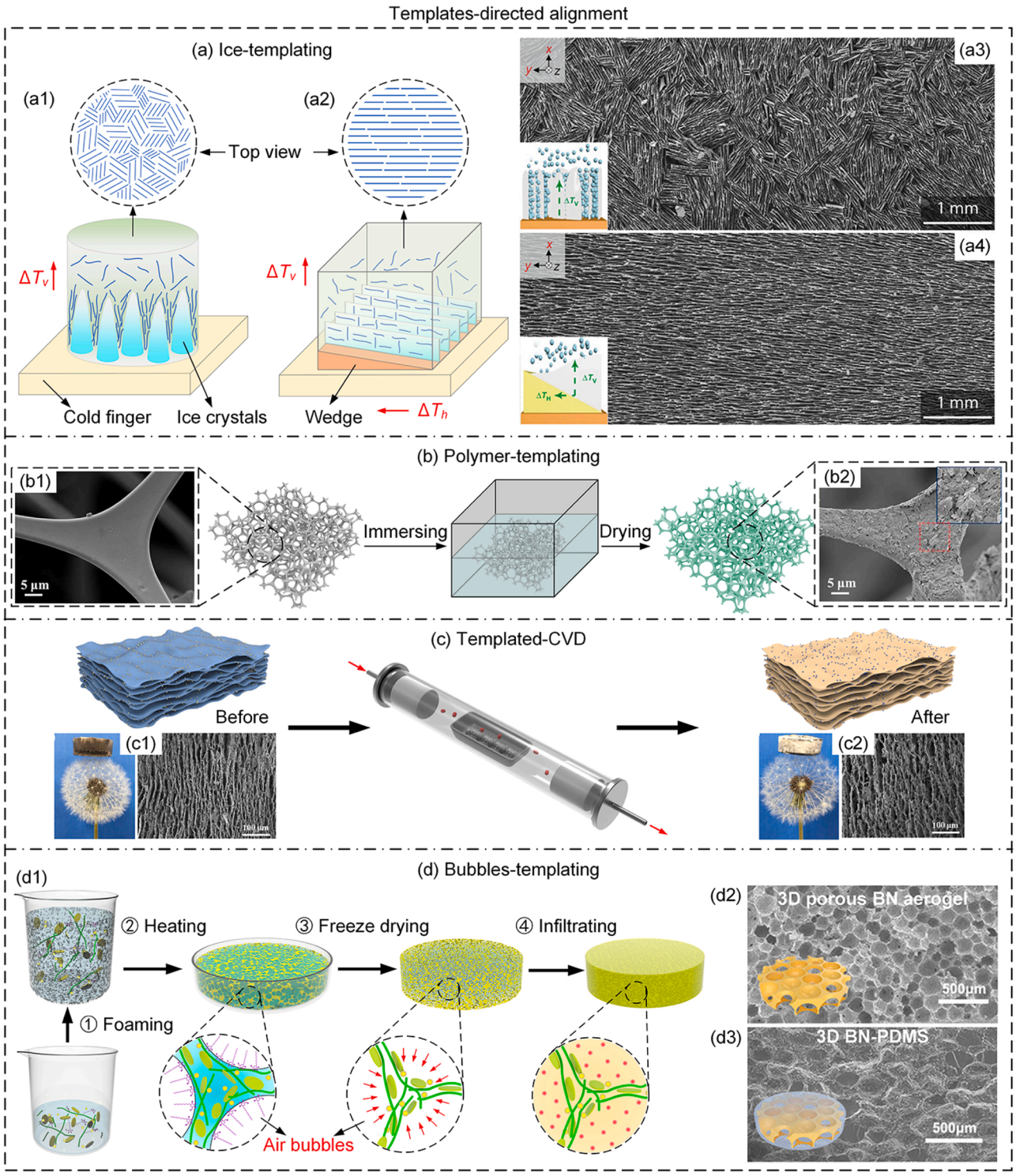

Fig. 4. Templates-directed alignment techniques. a) Ice-templating. a1) and a2) show the schematical setup and expected morphology of UFC and BFC, respectively, where ΔT_v and ΔT_h indicate the vertical temperature gradient and horizontal temperature gradient created in the system, respectively. a3) and a4) show the top-view SEM images of microstructures created by UFC and BFC, respectively. b) Schematic diagram showing the polymer-templating process. b1) SEM image of a MF foam as polymer template. b2) SEM image of MF/BN skeleton based on the template in b1). Inset shows the high-magnification image. c) Schematic diagram showing the fabrication process of templated-CVD. c1) Photograph and SEM image of a vertically aligned GO (VA-GO) sheet scaffolds. c2) Photograph and SEM image of a VA-SiC sheet scaffolds prepared by the CVD technique based on the VA-GO template. d) Bubbles-templating. d1) Schematic diagram showing the fabrication process of bubbles-templating method. d2) and d3) show a 3D BN aerogel prepared by bubbles-templating and a BN-PDMS composite after filling the voids in the aerogel by PDMS, respectively. Reproduced with permission.
(a) Reproduced with permission [160]. Copyright 2015, American Association for the Advancement of Science. (b) Reproduced with permission [172]. Copyright 2018, Elsevier. (c) Reproduced with permission [182] .Copyright 2020, American Chemical Society. (d) Reproduced with permission [187]. Copyright 2022, Elsevier. [186] Copyright 2020, American Chemical Society.

concentration of ions in the aqueous solution [169].

Polymer-templated alignment. Polymer foams are polymorphous and cost-effective templates with 3D interconnected nanostructures. By attaching fillers onto the surface of foams framework, the fillers can easily realize 3D-aligned morphology which duplicates the 3D network of foams. The most common templates are PU [170,171] and melamine (MF), [172,173] both of which are in adequate supply from industry. As displayed in Fig. 4b, the whole fabrication process consists of several simple procedures, including immersing foams into fillers solution, removing solvent (by centrifugation or drying), and removing foams skeleton (by etching or heating, if necessary) [174]. It should be noticed that the pore size of the above-obtained 3D network is determined by the inherent pores of commercial polymer foams. As an example, the pore size of the as-prepared MF/BN skeleton barely changes during the preparation (Fig. 4 b1, b2) [172]. To achieve a more precise control of the 3D nanostructures, researchers also developed custom-made polymer templates, such as the 3D-printed acrylonitrile butadiene styrene (ABS) template [175]. Based on this template, a highly conductive and stretchable graphene honeycomb (GHC) possessing long-range ordered hexagonal porous structure with ultralow density (3.25 mg/cm^3) and excellent electrical conductivity (72 S/m) was achieved.

Template-directed CVD alignment. Many materials such as graphene, [176,177] BNNS, [178,179] and transition metal dichalcogenide (TMDs) like MoS_2 and WS_2 [180] can be deposited onto metal templates (Cu, Ni, Fe, Co, etc.) through chemical vapor deposition (CVD) approach, since these materials are soluble in metal, depending on the depositing temperature. Therefore, the template-assisted CVD (templated-CVD) process based on commercially available metal foams can also realize a 3D-aligned fillers network. Fig. 4c shows the schematic diagram of this technique. Take the typical fabrication process of graphene foams as an example, [181] carbon precursor was introduced into a nickel foam by decomposing CH_4 at 1000 ºC, and then graphene films were precipitated on the surface of the nickel foam. Next, a thin layer of poly(methyl methacrylate) (PMMA) was deposited onto the surface of graphene film to avoid the collapse of the nickel skeleton, and the nickel foam was removed by etching with hot acid (HCl or $FeCl_3$/HCl) solution. Finally, a free-standing graphene foam which inherited the original morphology of metal foam was obtained after dissolving the PMMA layer with acetone. The templated-CVD alignment method is quite similar with the polymer-template alignment method. Although time- and cost-consuming, the templated-CVD method could fabricate 3D foams that duplicate the original microstructure of template, demonstrating ultralight, high mechanical strength, and excellent thermal characteristics (Fig. 4 c1, c2). [182].

Bubbles-templated alignment. Different from the polymer-templating alignment and the templated-CVD alignment that depend on the ready-made templates, bubbles-templating alignment approach provides another route for generating 3D templates by the generation of massive air bubbles. [183,184] As shown in Fig. 4d, in this method, the fillers are firstly dispersed in aqueous solution, and then plenty of air bubbles are produced by stirring the solution intensively. During this process, the fillers are excluded into the narrow gap between those closely packed air bubbles, resulting in face-to-face aligned fillers network on the boundary of each air-bubble. After that, the expanded emulsion is freeze-dried to form 3D-fillers network templated by regular air bubbles. Following this route, 3D networks such as graphene aerogel [183–185] and BN aerogel [186,187] with superior mechanical and thermal properties can be prepared. In the work of Li et al., a 3D-interconnected thermal-conductive BN network is constructed by the bubbles-templating technique, which achieves a thermal conductivity of 1.58 Wm^{-1}K^{-1} at a low BN content of 25.4 wt% (Figure 4d2, d3) [186]. One of the advantages of this method is, the pore structure and morphology of the as-prepared 3D aerogels can be easily controlled by tuning the air bubbles in the foaming process. As demonstrated by Zhang et al., the foaming volume is proportional to the stirring speed, and more air bubbles were formed with the increasing stirring speed [185]. Besides, the viscosity of mixture also influences the formation of stable and closely packed air bubble template. Low viscosity would decrease the stability of air bubbles, while high viscosity would result in a gel-like slurry that is not suitable for the formation of foams. It should be emphasized that, foaming agent (such as alkyl polyglucoside, APG) and gelling agent (such as curdlan), which help to generate and stabilize the air bubbles network, respectively, are also necessary in the low-filler-concentration cases.

2.4. 3D printing alignment

The 3D printing (3DP) is also known as additive manufacturing, which involves a wide range of ink- and light-based printing techniques that build bridges for the digital design and fabrication of 3D entities. [188–190] In traditional 3DP, a translation stage moves a pattern-generating device which is in the form of laser optics or an ink-based printhead, to build a patterned layer of targeted objects at a time. In the meantime, the patterned regions are solidified to generate the desired 3D architecture. Compared with traditional manufacturing methods that need molds, dies or lithographic masks, the digital assembly strategy of 3DP makes it possible to rapidly convert computer-aided designs (CADs) to complex 3D objects. Owing to its huge digital-designing freedom, the 3DP technique enables the complex construction of biomedical devices, [191] human tissues, [192,193] and optical/electronic devices [194–196] that are hard to be realized by other techniques.

Beyond classic 3DP, the combination of nanotechnology and 3DP opened a new door for manufacturing functional materials with ordered architecture across various length scales. For example, the incorporation of nanofillers into 3DP not only improve the functionality of the 3D object, it may also result in a better printability. [197] Different types of fillers such as metal nanofiller, [198] nanoclay [199] and carbonaceous nanofillers, [200] have been added into both thermoplastics and thermosetting resins to realize improved properties. Thus, this strategy is eminently suitable for printing synthetic analogues of natural composite materials such as nacres, [201] bones, [202] and woods, [203] in which the spatial organization and alignment of reinforcing fillers within polymers are well controlled. Here, we mainly focus on the 3DP techniques through which fillers were incorporated for the fabrication of aligned macro- and micro-structures.

Light-based 3DP. The incipient 3DP methods use light to fabricate 3D architectures based on either the stereolithography (SLA) of photo-hardening polymers (Fig. 5a), [204] or the selective laser sintering (SLS) of polymeric powders (Fig. 5b). [205] In SLA, a liquid-type photocurable polymer is exposed to ultraviolet (UV) light and then solidified from the surface. The thickness and spatial distribution of the solidified layer is controlled by the UV intensity and exposure time, and exposure area, respectively. Subsequently, a new polymer layer is introduced and crosslinked with the previous layer in locally illuminated regions. By repeating these procedures layer-by-layer, the desired 3D object is obtained. Based on this original concept, some evolutional techniques, including continuous liquid interface production (CLIP), [206] digital lithography projection (DLP), [100] and two-photon polymerization (2PP) [207] are developed to realize much faster printing speed or higher lateral resolution. When incorporating fillers into the photocurable polymers, these newer 3DP methods are able to print 3D objects in which the fillers are spatially aligned within polymer matrices.

As a promising approach termed as magnetic 3DP, the external magnetic fields are introduced in DLP to control the fillers' distribution and orientation in photo-hardening resins [206]. The printer is firstly modified by three electromagnetic solenoids placed around its periphery, and the fillers are coated with superparamagnetic nanoparticles (such as iron oxide nanoparticles) to response to external fields along a prescribed vector in 3D space. The magnetic 3DP requires additional steps to align the composite fillers during the print process. First, elements within each print layer are separated into groups according to

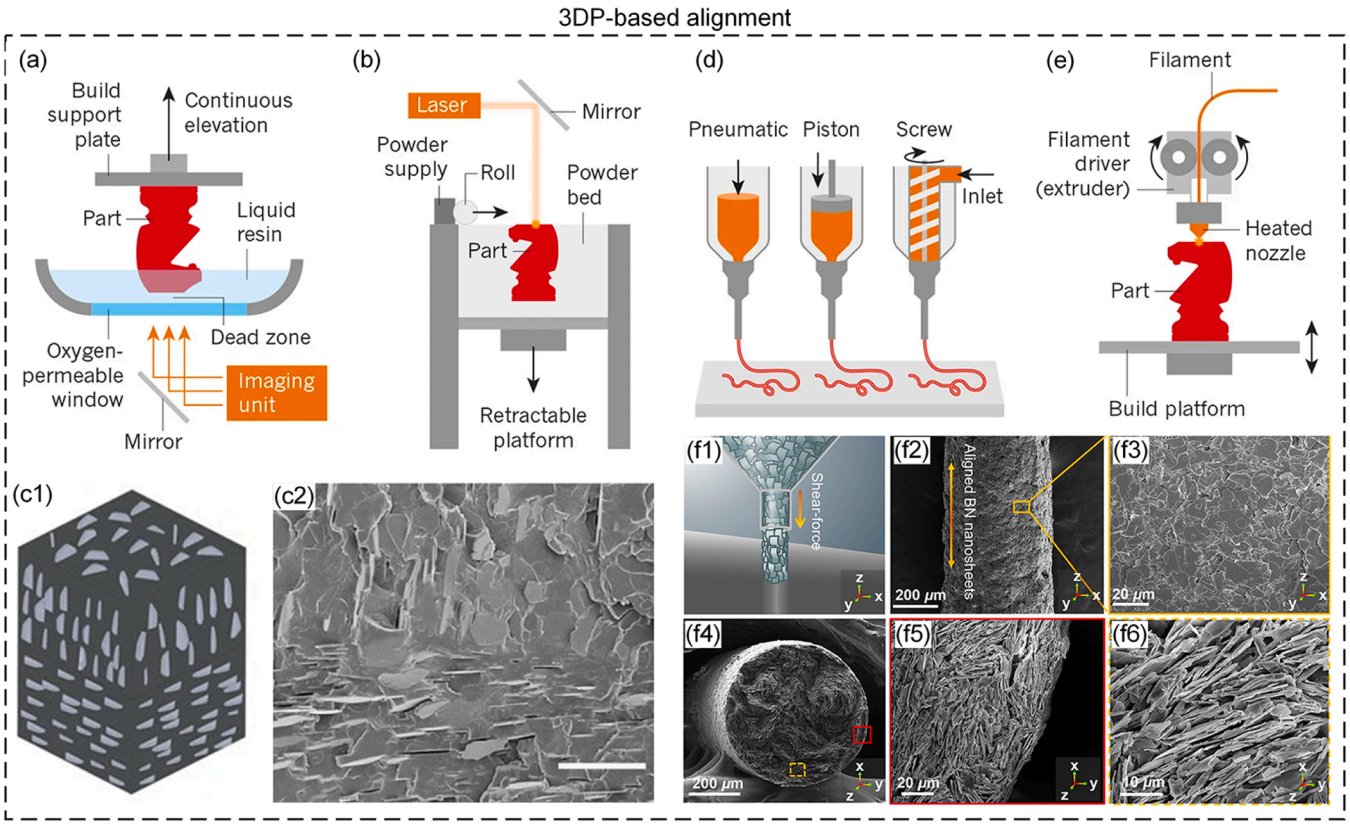

Fig. 5. 3DP-directed alignment. Light-based 3DP: a) SLA and b) SLS. c1) Desired layered architecture and c2) the printed microstructure created with magnetic 3DP. Scale bar, 25 μm in c2). Ink-based 3DP: d) DIW and e) FDM. f) 3D vertical printing of BN rods and arrays with highly aligned BN nanosheets. f1) Schematic showing the orientation and alignment of BN nanosheets under the shear force induced by the extrusion of BN ink. f2, f3) SEM images of the surface morphology of a BN rod. f4-f6) Cross-sectional SEM images of a BN rod. These images show that the BN are well-aligned and densely packed along the extrusion direction.
a), b), d), e), reproduced with permission [188]. Copyright 2016, Nature Publishing Group. c1), c2), reproduced with permission [100]. Copyright 2015, Nature Publishing Group. f), reproduced with permission [210]. Copyright 2019, American Chemical Society.

their desired orientation. Then, a dynamic magnetic field is applied to align the fillers, where the alignment time varies with the field strength, solution viscosity, fillers geometry and nanoparticles coverage. After that, the aligned elements are polymerized by the DLP. By repeating these procedures, complex aligned architectures that deliver enhanced material properties compared with monolithic structures can be fabricated. The feature size of printed polymer voxel can be narrowed to ~90 μm based on fillers of ~10 μm, as displayed in Figure 5c1, c2. [100] However, this strategy also has its limitation in aligning high-concentration fillers, which is quite similar with traditional magnetic field-assisted alignment technique.

Ink-based 3DP. Due to the necessary photocuring procedure, the light-based printing techniques are limited to printing either photocurable polymers or thermoplastic polymer powders. The ink-based 3DP approaches, including direct inkjet writing (DIW), [188] fused deposition modeling (FDM), [208] and powder bed fusion (PBF), [209] can print numerous soft materials that are composed of wide range of molecular, polymeric or particulate categories, in the form of printable inks. In these methods, soft matters are placed by printheads which are quite like those in the document's printer. Under low viscosity condition such as that in DIW (Fig. 5d), the ink is in the form of droplet and is extruded by pressure from a nozzle tip to generate the designed printing path. The ink droplet materials in DIW are typically designed to rapidly solidify after leaving the nozzle. When incorporating thermally functional fillers into the printable inks, the flow field introduced by the nozzle generates shear force and drives the fillers to align along the flowing direction, thus reinforced thermal properties can be produced. For example, Liang *et al.* reported a vertically aligned structure of BN rod with high through-plane thermal conductivity of 5.65 $Wm^{-1}K^{-1}$ for pure BN rod, and 1.5 $Wm^{-1}K^{-1}$for BN-poly(dimethylsiloxane) (PDMS) composite via DIW (Fig. 5f) [210]. However, the rheology properties of the ink may be affected by the additional fillers. The ink droplet formation is decided by both the ink material properties and the printing parameters, including the viscosity, density, surface tension and feature size (i.e., the droplet diameter in most cases) of ink, and the velocity of the ejected droplet and the nozzle size. Therefore, it is improbable to jet complex fluids such as high-density polymer solutions, or solutions containing fillers with large size or high concentration.

Compared with droplet-based approaches, the extruded filament printing methods are more suitable for dealing with complicated inks. Take FDM as an example, thermoplastic filaments are first melted and fed through a hot extrusion head, and then solidified after cooling below their glass transition temperature [211]. FDM is easy to scale up and can be used to manufacture structural materials containing high-filling-load fillers. For example, Guo *et al.* reported the formation of asymmetrically aligned structure of graphene filled thermoplastic polyurethane (TPU) composites via FDM, and the through-plane thermal conductivity reached up to 12 $Wm^{-1}K^{-1}$ at 45 wt% graphene content [212]. The high TC is mainly attributed to the flat-aligned and vortex-aligned graphene sheets in each extruded microfilament. However, due to the limitation of maximum temperature of the heat chamber, the feedstock filaments in FDM are limited to those thermoplastic polymers, such as acrylonitrile butadiene styrene (ABS), polylactic acid (PLA), etc. Besides, the technical issues such as the distortion of the parts and the generation of voids due to the rapid heating and cooling cycles that may deteriorate the thermal and mechanical properties should be investigated and resolved [213].

Fig. 6 concludes the relationship between above-mentioned

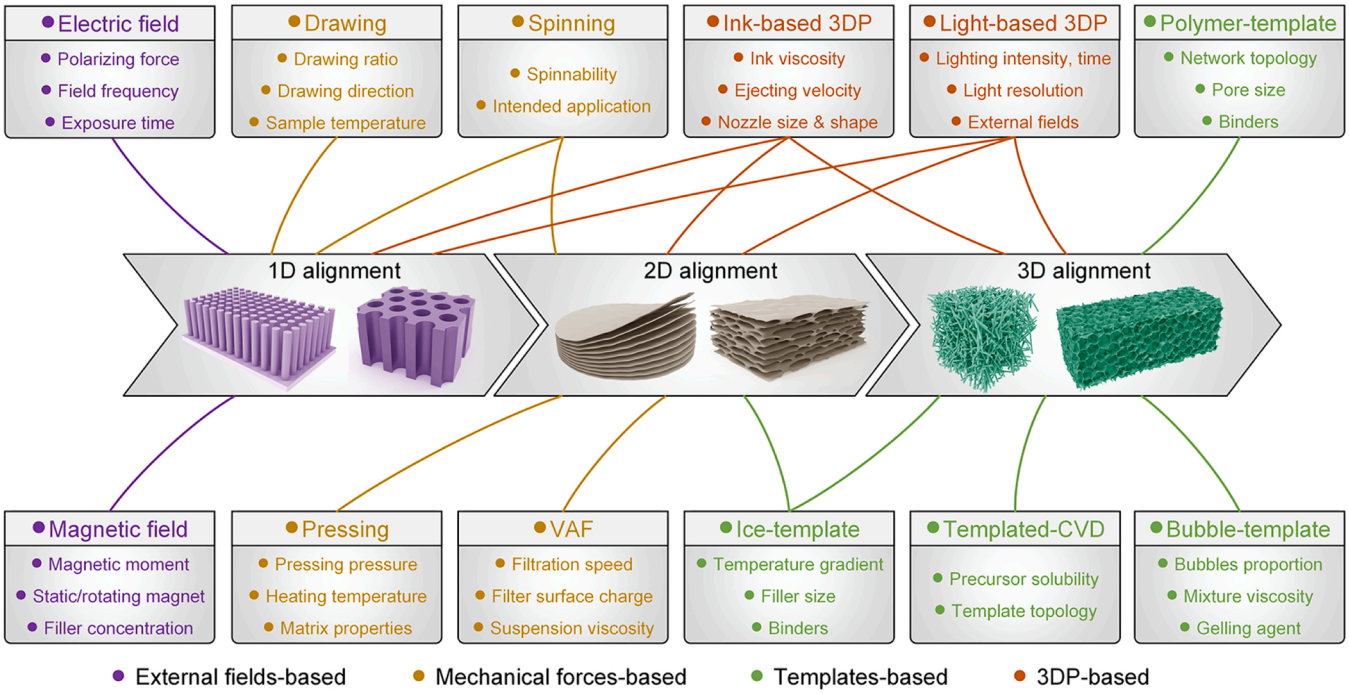

Fig. 6. Relationship between aligned structures and alignment techniques.

alignment techniques and their attainable aligned structures, along with the key parameters in each technique. Generally, the external fields-based techniques including the electric field- and magnetic field-based alignment are suitable to realize 1D alignment, because their driving forces are rigidly one-directional. The mechanical forces-based techniques can achieve both 1D and 2D aligned structures, since their driving forces can be single-directional (such as drawing), planar (such as pressing and VAF), or switchable (such as spinning), according to the specific processing setup. For the templates-based alignment techniques, the attainable aligned structure is determined by the pristine morphology of templates. Therefore, the ice-templating can realize both 2D and 3D aligned structures owing to the versatile microstructure of ice crystals. While, other techniques can only achieve 3D structures due to the limitation of their own templates. It is worth noting that the 3DP-based alignment techniques demonstrate the widest design freedom over other methods, which enable them to realize full-directional alignment control toward fillers.

3. Alignment engineering for thermal conduction

The sharply increasing packaging density and driving power within microelectronic devices have brought one of the most vital requirements for thermal materials, i.e., the high thermal conductivity characteristic for the purpose of efficient cooling or heating. Polymer composites consisting of polymer matrix and thermal reinforcement fillers are commonly used thermal interface materials (TIMs) for rapid heat removal from heat sources to the heat sinks. However, traditional TIMs are suffering from limited thermal conductivity, even with the massive loading of thermal fillers. This is mainly attributed to the weak transport ability of phonons (the energy quanta of atomic lattice vibrations) in the disordered polymer chains, the lack of continuous thermal transfer pathways, and the strong phonon scattering at the interfaces between fillers and polymer matrix.

The good news is that numerous advances have been made to make up these imperfections. For example, by reducing the entanglement and increasing the alignment of polymer chains, PE film with thermal conductivity of 62 $Wm^{-1}K^{-1}$ which outperforms that of many conventional metals (304 stainless steel ~15 $Wm^{-1}K^{-1}$) and ceramics (aluminum oxide ~30 $Wm^{-1}K^{-1}$) were achieved [45]. By constructing highly ordered graphene framework and reducing the thermal interface resistance simultaneously, polymer composites with extremely high thermal conductivity of 56.8–62.4 $Wm^{-1}K^{-1}$ at the graphene loading of ~13.3 vol% were obtained, achieving a thermal conductivity enhancement (TCE) over 2400% with per 1 vol% filling content [214]. It is worth noting that most of these exciting breakthroughs are related to the alignment engineering of materials which reinforces the orderliness of composites. Therefore, in this section, recent progress on thermal conduction reinforcement based on alignment techniques are discussed.

3.1. Alignment of polymers

Polymers are materials consisting of long molecular chains, in which each chain is composed of repeated structural units called monomers. The average chain length is usually characterized by the average weight of each macro-molecule, i.e., the molecular weight. Polymers can be as short as just a few monomers, or as long as thousands of monomers such as the ultra-high molecular weight polyethylene (UHMWPE) [215] Bulk polymers are generally regarded thermal insulators due to their low thermal conductivities at room temperature (on the order of 0.1–1.0 $Wm^{-1}K^{-1}$) [216,217]. The underlying origin is that in the amorphous phase, pervasive defects, and structural disorders in polymers, including chain entanglements, chain ends, crystal-amorphous interfaces and voids, act as phonon scattering sites that inhibit the efficient thermal transport [218].

In fact, most polymers such as PE, polyacetalene (PA), polyvinylchloride (PVC), etc, themselves contain backbone of carbon-carbon bonds, similar to those in diamond, one of the most thermally conductive materials (over 1000 $Wm^{-1}K^{-1}$) [219]. Therefore, these polymers have the potential to feature very high thermal conductivities since phonons can transport within individual chains at high speeds. Once the polymer chains are highly ordered, the phonons are able to propagate for a large distance in a straight unimpeded line. Therefore, the realization of intrinsically high thermal conductivity for polymers may exist in elongated single molecules or arrays of aligned chains. In as early as 1978, pioneer researchers have conducted molecular dynamics (MD) simulations [220,221] and measurements on the thermal conductivity

of aligned chains [222] and nanofibers, [108] all suggesting that these individual chains do have extremely high thermal conductivity.

With the encouragement of those exciting proof of concepts, researchers have devoted themselves into the realization of highly thermal-conductive polymers. Since most of polymers are semi-crystalline of which crystalline regions are embedded in amorphous matrix, increasing the alignment of chains, and reducing the amorphous component is the most mentioned idea to increase the mechanical and thermal properties of polymers. This purpose can be approached by processing bulk samples into thin films or fibers [223]. For example, some commercial PE fibers fabricated by spinning-induced alignment technique demonstrate a thermal conductivity of 30–40 $Wm^{-1}K^{-1}$ at room temperature. [224,225] By mechanically stretching the polymers chains, UHMWPE nanofibers with thermal conductivity of 104 $Wm^{-1}K^{-1}$[108] and PE films over 60 $Wm^{-1}K^{-1}$[45] were achieved, as shown in Figs. 7a and 7b, respectively. In the initial stage of the stretching process, small crystalline blocks are untied from the crystalline lamellae and turned into microfibrils along the stretch direction. Under this small drawing ratio, the crystalline blocks are still entangled and interconnected by the intra-microfibrillar tie molecules, originating from the partially unfolded polymer chains. Meanwhile, these microfibrils are connected by the inter-microfibrillar tie molecules, termed as the bridging molecules. With the increase of stretch ratio, the microfibrils are further disentangled and aligned by the shear force, resulting in a decrease of the microfibrillar volume fraction and an increase of fully unfolded interfibrillar tie molecules. Finally, these increasingly aligned chains result in a larger average crystal size along the stretch direction. This is the underlying origin of the enhanced mechanical and thermal properties. Therefore, increasing the stretch ratio will enhance the volume fraction of the chain-aligned crystalline region, thus reinforcing the thermal conductivity of polymer samples. [45,108,109] Subsequently, it is found that heating while stretching helps the further elongation of polymer chains, and thus a general trend of higher thermal conductivity with higher stretching temperature was observed by Zhu et al. [226] as shown in Fig. 7c. However, the thermal conductivity drops when the stretching temperature approaches the melting point of bulk polymers, since such a high temperature may cause the loss of shearing stress when crystallites melt. In Fig. 7d, Shrestha et al. obtained PE nanofibers with thermal conductivity of 90 $Wm^{-1}K^{-1}$ by a local-heating based stretching method [227]. With this approach, a high strain rate of 1400 s^{-1} can be achieved, and the nanofibers can be rapidly quenched to minimize the relaxation, resulting in a nearly defect-free aligned crystalline PE nanofiber.

Besides stretching method that creates more crystalline domains within polymers, Singh et al. reported on a template-assisted electropolymerization method to align the chains of polythiophene nanofibers in a purely amorphous form and achieved a thermal conductivity up to 4.4 $Wm^{-1}K^{-1}$, more than 20 times than that of bulk polymer. [44] According to their results, the enhanced thermal conductivity of amorphous nanofibers originates from the relatively high thermal conductivity of single aligned polymer chains, which reduce the phonon scattering from an overall disordered structure. This enhancement in thermal conductivity enables vertically aligned arrays of polythiophene to be used as TIMs with a low total thermal resistance of 12.8 ± 1.3 $mm^2 K W^{-1}$. After that, Xu et al. revealed that the amorphous regions of PE films also have a surprisingly high thermal conductivity over 16 $Wm^{-1}K^{-1}$ under a stretch ratio of 110, [45] which suggests that the amorphous regions may as well enable efficient phonon transport after chains alignment. Shanker et al. utilized electrostatic repulsive forces between ionized pendant groups on the backbone of polyelectrolytes to stretch the polymer chains, and achieved an amorphous polymer with randomly aligned yet layered-stacked polymer chains, featuring an enhanced thermal conductivity of 1.2 $Wm^{-1}K^{-1}$. [228] These findings provide an alternative means for achieving highly thermal-conductive polymers by aligning the non-crystalline chains of polymers, which is more likely to realize the scalable manufacturing of heat-conducting polymers.

Electrospinning is also an effective way to fabricate aligned polymer nanofibers. During the electrospinning process, the polymer solution drop is greatly drawn along the collector rotating direction under electrostatic force, and thus nanoscale polymer fibers with uniaxially aligned morphology are obtained. Zhong et al. reported on electrospun Nylon-11 nanofibers with different diameters ranging from 109 to 413 nm [229] It is revealed by the wide-angle X-ray scattering (WAXS) data that the longitudinal crystal size grows with the decreasing fiber diameter, which implies a longer phonon mean free path (MFP) along the aligned direction, as displayed in Fig. 7e. Besides, the fraction of extended chains paralleling to the fiber axis also increases as the fiber diameter decreases. These transformations facilitate efficient phonon propagation along the fiber axis. As a result, the thermal conductivity of 109 nm nanofiber is ~0.8 $Wm^{-1}K^{-1}$, about 3 times higher than that of 413 nm. The above-mentioned electrospun nanofibers were fabricated with a relatively low electric voltage of 6–7 kV. One more study by Canetta et al. reported the thermal conductivity of individual polystyrene nanofibers, which were fabricated under electrospinning voltage of 7–10 kV, ranges from 6.6 to 14.4 $Wm^{-1}K^{-1}$ [230]. These values are significantly higher than those of bulk polystyrene, which may be attributed to the higher degree of molecular chain alignment from higher strain rates within the electrospinning jets under higher voltage. Therefore, Ma et al. further explored the effects of electric field intensity on the molecular alignment as well as thermal properties of electrospun PE nanofibers [231]. As depicted in Fig. 7f, under increasing voltages varying from 9 to 52 kV, the measured thermal conductivity of nanofibers at each electrospinning voltage increases linearly with the voltage. High degree of molecular orientation and better crystallinity at high voltage is also validated by analyzing the structural change of PE nanofibers using Raman spectroscopy, from which it is observed that the C-C band intensity becomes significantly larger. Meanwhile, it is noticed that the highest thermal conductivity value of 9.3 $Wm^{-1}K^{-1}$ was obtained at voltage of 45 kV rather than 52 kV. This is mainly because of the trade-off between higher electric force and shorter flight time for fiber crystalline structure formation. The existence of optimal electrospinning voltage was also confirmed by Ero-Phillips et al. in their work of electrospun poly(L-lactic acid). [232].

3.2. Aligning fillers in composite materials

Compared with pure polymers, composite polymers with the incorporation of highly thermal-conductive fillers demonstrate higher thermal conductivity as well as ease of use. Typically, thermally conducting but electrically insulating fillers such as ceramic fillers (BN, AlN, SiC, Al_2O_3, etc.) are used for applications in which insulator composites are required [233,234]. Those thermally and electrically conducting fillers such as metal fillers (Al, Ag, Cu, Ni etc.), [235–237] and carbon derivatives (Graphene, carbon nanotube, carbon nanofiber, diamond, etc.), [238–240] can be adopted in those applications without an insulation requirement. The effective thermal conductivity of these composites is determined by the intrinsic properties of polymer and fillers, the distribution and alignment of fillers, the filling fraction of fillers, and the interface between polymer and fillers, etc. Given these variables, it is difficult to reveal and estimate the thermal conduction properties of composite polymers.

Till now, many theories have been proposed to predict the thermal conductivity of composite materials. The most widely used effective medium theory (EMT) was first proposed by Maxwell Garnett and then improved by Bruggeman. [241] EMT is suitable for describing composites with low volume fraction (< 25%) and neglectable interaction between fillers. Later on, Geometric model, [242] Agari and Uno model, [243] Hamilton and Crosser model, [244] Lewis and Nielsen model, [245] Cheng and Vachon model, [246,247] etc., were developed to describe the thermal transport behavior of composite materials with specific configurations. Here, we are not intending to discuss these

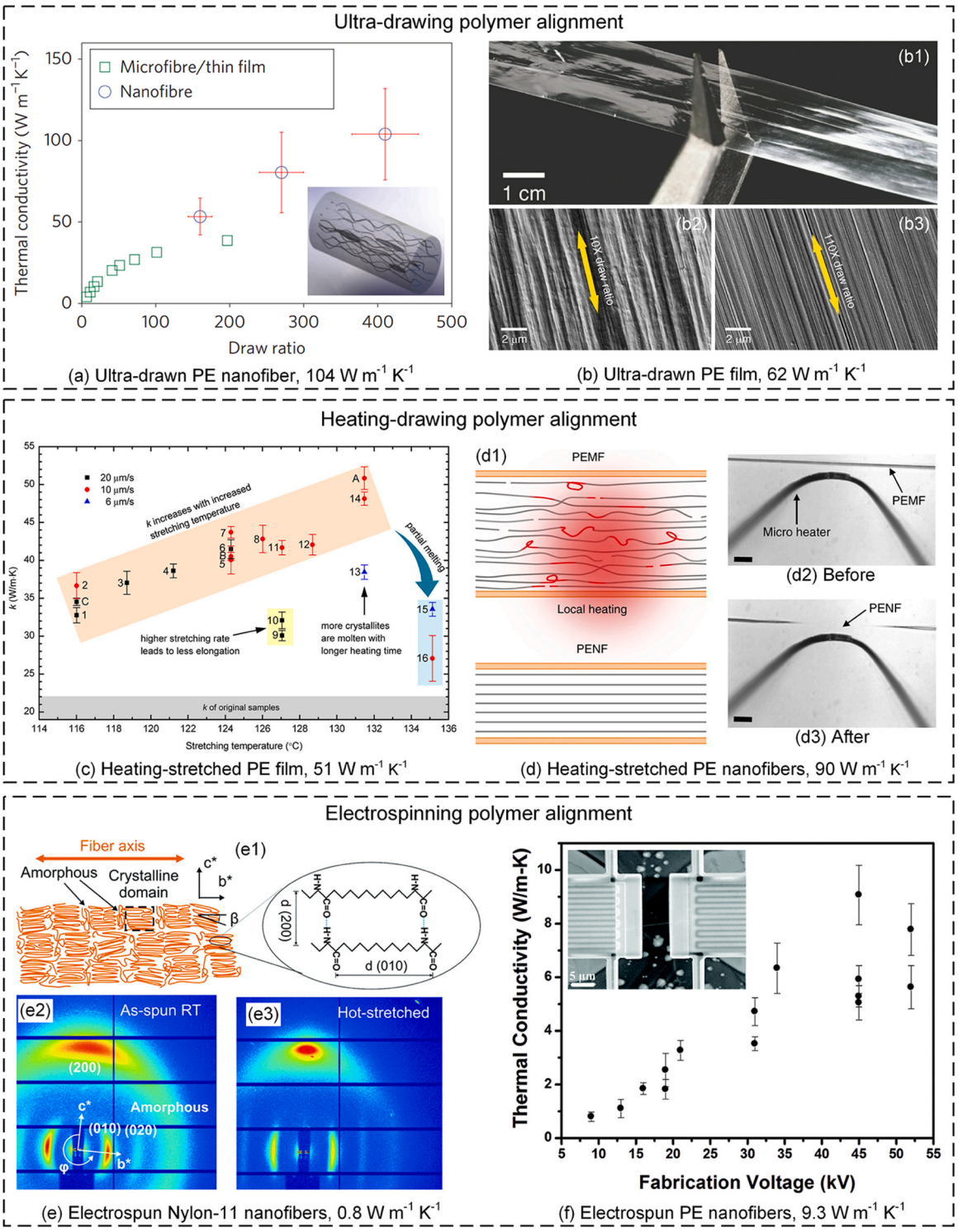

Fig. 7. Alignment engineering of polymers for heat conduction. a) Thermal conductivity of ultra-drawn PE nanofiber under different drawing ratio. b) Ultra-drawn PE film. b1) Photograph of a thin transparent drawn PE film. b2) and b3) show the SEM images of PE film with drawn ratio of 10 × and 110 × , respectively. c) Thermal conductivity of UHMWPE fibers after being stretched at different rates and different temperatures. d) Heating stretched PE nanofiber. d1) Schematic illustration of a localized drawing with a microheater to fabricate PE nanofiber from a PE microfiber. d2, d3) Optical micrographs before and after localized heating-drawing. Scale bars, 20 μm. e) Electrospun Nylon-11 nanofibers. e1) Schematic of the molecular arrangement in Nylon-11 nanofibers. Wide-angle X-ray scattering (WAXS) patterns from uniaxially aligned nanofibers with initial diameter of ~200 nm are shown for e2) as-spun at room temperature (RT) and e3) after hot-stretching to a 1.5 × draw ratio at 120 °C, respectively. f) Thermal conductivity of the electrospun PE nanofibers under increasing fabrication voltages. Inset show the SEM image of a single nanofiber suspended between two adjacent SiN_x membranes on a measurement device.
(a) Reproduced with permission [108,108]. Copyright 2010, Nature Publishing Group. Inset shows an ideal polyethylene nanofiber with perfectly aligned molecular chains. (b) Reproduced with permission [45]. Copyright 2019, Nature Publishing Group. (c) Reproduced with permission [226]. Copyright 2017, American Chemical Society. (d) Reproduced with permission [227]. Copyright 2018, Nature Publishing Group. (e) Reproduced with permission [229]. Copyright 2014, The Royal Society of Chemistry. (f) Reproduced with permission [231]. Copyright 2015, The Royal Society of Chemistry.

models in detail since this is out of the scope of this review. To gain an extensive understanding of these thermal models, detailed review literatures wrote by other peer researchers are recommended [248].

Besides these models, it is also recognized that the thermal percolation behavior is a critical criterion for evaluating the effectiveness of fillers incorporation. Under low filler loading fraction, the fillers are separately distributed or form short clusters within the polymer matrix. Once the filler loading fraction exceeds a critical value, known as the percolation threshold, the fillers will form interconnected pathways that enable rapid thermal transport. [249] Under this situation, heat can be transferred efficiently through the 'highspeed' fillers network rather than the polymer matrix. Thus, the thermal conductivity of composite materials can be significantly improved when thermal percolation is reached. In the beginning of this research field, the thermal percolation is achieved by simply increasing the dosage of randomly distributed fillers. However, the overload of fillers also results in an enlarged interfacial thermal resistance between filler-filler and filler-polymer, which diminishes the enhancement of thermal conductivity. Besides, it also increases the difficulties in processing the high viscosity composites, and results in a composite material with high elastic modulus that is undesired in flexible electronics applications.

In recent decades, great efforts have been devoted to construct ordered filler network within polymer matrix for efficient thermal conduction. By arranging the alignment of fillers in desired manner, the thermal percolation can be realized under a relatively low filler loading fraction. Thus, the obtained composite materials have both outstanding mechanical and thermal properties. According to the geometry of filler, the aligned thermal network within composite polymers can be classified into 1D filler network (micro/nano-wires, -tubes) and 2D filler network (micro/nano-platelets, graphene, etc.). It should be noticed that there are also many 0D fillers (mainly micro/nano-spheres) such as Ag microspheres, [250] Cu nanoparticles, [251] etc. However, these 0D fillers demonstrate limited tunability in the formation of thermally conductive network due to their poor ability of being interconnected with each other, unless mixed with other components.

3.2.1. 1D aligned architecture

Considering the special geometric feature of 1D fillers, it is feasible to align all the fillers into a single orientation which is coincident with the desired heat dissipation direction, namely the 1D aligned architecture. In this architecture, the fillers form numerous 'head-to-tail' chains within the polymer matrix that make the best use of their thermal properties and minimize the influence of thermal interfaces. Carbon-derivate nanomaterials including carbon fibers (CFs), [252] carbon nanotubes (CNTs), [253] and Silicon Carbide (SiC) nanowire, [254] etc., and metal nanowires such as Ag nanowires, [255] are considered as ideal 1D fillers for polymer composites, since they exhibit high thermal conductivity, deformability and flexibility simultaneously. To achieve rigidly aligned architecture, external forces such as electric field, [86] magnetic field, [256] mechanical force, [257] and shear force, [258] which can provide uniform and single-directional driving forces, are needed to provide torque for moving as well as rotating the fillers.

Most 1D fillers can be directly manipulated by the applied DC or AC field thanks to the existence of their free surface electrons. According to the research by Martin *et al.*, [78] the AC electric field is more effective in realizing uniform and aligned CNTs network than DC field. Since in the duration of DC field, the fillers tend to move and absorb onto the electrode under electrophoresis effect. Then, the tips of nanotubes become source of high field strength and location for absorption of other fillers, finally resulting in a ramified filler network connecting the anode and cathode. While, by slightly changing the experimental setup, a high-density and uniform array of fillers are also attainable based on DC field. Uetani *et al.* introduced an electrostatic flocking technique to make vertically aligned, high-density CFs arrays on a planar substrate (Fig. 8 a1). [252] Different with traditional electrophoresis system where the fillers are suspended in liquid, the CFs in the electrostatic flocking system are placed on one face of two parallel electrodes, and then a potential is applied between the two electrodes. During this process, the CFs will be charged and propelled toward the opposing electrode because of electrostatic attraction, forming a vertically aligned CFs scaffold (Fig. 8 a2, a3). By filling the CFs scaffold with elastomeric polymer, a composite showing high thermal conductivity of 23.3 $Wm^{-1}K^{-1}$ was achieved under filler loading of 13.2 wt%.

For magnetic field approach, a strong magnetic field is usually needed to manipulate the pristine 1D fillers. Kimura et al. has demonstrated earlier that a constant magnetic field of 10 T induced alignment of CNTs in the polyester matrix, while the alignment deteriorated with the increasing filler loading. [259] This is because that the magnetic force is insufficient to overcome the resistance against rotating in a viscous polymer matrix and the van der Waals forces between fillers. Subsequently, higher magnetic field up to 25 T were applied to realize more favorable alignment of MWCNTs and SWCNTs. [256,260] Although effective, such a high magnetic field severely hinders the wide application of this method. To improve the response of 1D fillers under a low magnetic field, efforts have been devoted to increase the magnetic susceptibility of fillers by attaching magnetic inorganic nanoparticles such as Fe_3O_4, NiO, CoO, etc., onto the filler surface. [261] With the decoration of these superparamagnetic nanoparticles, a relatively low magnetic field of 0.3 T is sufficient to form a high anisotropy of aligned CNTs. [262].

For the mechanical stretching or shearing flow method, the generated shear force is the only driving force for aligning 1D fillers along the shearing direction. A high temperature process of either hot-stretching or melt-extruding is usually needed to create a flowing polymer matrix in which the fillers can be oriented. [263,264] It is agreed that there is a positive relationship between the shear rate and the degree of fillers' alignment. As an example, Abbasi *et al.* investigated the alignment of MWCNTs at different levels of shear rate using Raman spectroscopy, and revealed that the nanotubes are preferentially aligned in the flow direction at large injection or compression rates [265]. This is mainly because that the high shear rate breaks down the nanotube agglomerations and facilitates the orientation of the nanotubes in the flow direction. Besides, there is an inversely proportion between the aspect ratio of fillers and degree of alignment, since the agglomerations and entanglement are more dominate under higher aspect ratio condition [266].

Owing to the extremely high thermal conductivity of individual CNTs (~3000 $Wm^{-1}K^{-1}$), the vertically aligned CNTs array can have promising thermal conductivity as high as those of metals (~265 $Wm^{-1}K^{-1}$) [267]. Goodson et al. presented the first benchmark work towards thermal conductivity of aligned-CNTs composites with controlled CNTs density [268]. They found that a 1 vol% CNTs can double the thermal conductivity of the base polymer, and a dense packed CNTs with filling load of 16.7 vol% can increase the thermal conductivity up to 4.87 $Wm^{-1}K^{-1}$ (18-fold, Fig. 8b). By growing vertically aligned CNTs arrays on silicon substrates with optimized density and reduced defects, Ivanov et al. reported an out-of-plane thermal conductivity of 5.5 $Wm^{-1}K^{-1}$ for epoxy-infiltrated CNTs array (8 vol%) [269]. However, the thermal conductivities reported above are lower than expected for CNTs-based materials, and also lower than those reported for unfilled CNT arrays.

This discrepancy can be attributed to the following reasons. First, the contact area between nanotubes exists even in the perfectly aligned CNTs array, and consequently introduce contact resistance due to the phonon scattering on the contact points. The thermal contact resistance may strongly influence the effective thermal conductivity of the composite materials. To reduce the effect of point-contact between CNTs, Hu et al. proposed to increase the contact area between neighboring CNTs with the assistance of graphene nanosheets. [270] Instead of transporting heat from single nanotube to its adjacent nanotubes through the limited inter-tube contact, the heat can be transferred through the larger contact area between CNTs and graphene, thus reducing the boundary scattering effect and facilitating the phonon transport. As a result, the

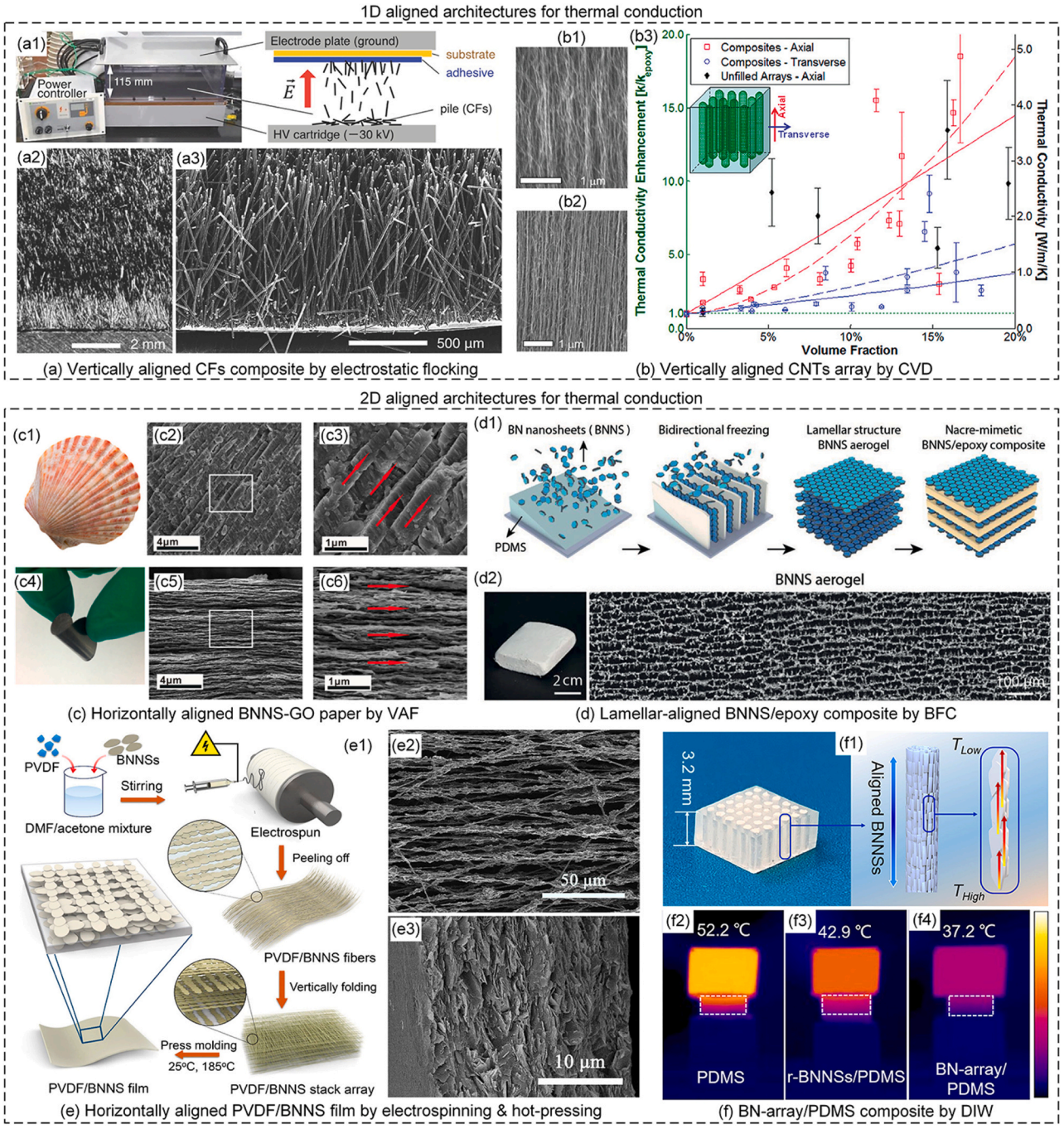

Fig. 8. 1D and 2D aligned architectures in composite materials for heat conduction. a) Vertically aligned CFs composite by electric field. a1) Set-up of the electric field-directed alignment system. a2) Optical image and a3) SEM image of the vertically aligned CFs scaffold taken at a 45° viewing angle. b) Vertically aligned CNTs array by CVD. b1) and b2) show the SEM images of the aligned CNT films with 1 vol% CNTs (A-CNT 1% v_{CNT}) and the aligned CNT films with 20 vol% CNTs (A-CNT 20% v_{CNT}) after biaxial mechanical compression, respectively. b3) The axial and transverse thermal conductivity of CNT nanocomposites and unfiller CNT array, as a function of volume fraction. The schematic below the legend shows the axial and transverse measurement directions for the aligned CNT composites. c) Horizontally aligned BNNS-GO paper by VAF. c1) Photograph of natural nacre. c2) Cross-sectional micrograph of natural nacre. c3) Enlarged view of the white rectangle area in c2), where the red arrows highlight the aligned area. c4) Photograph of the BNNS-GO paper. c5) Cross-sectional micrograph of the BNNS-GO paper. c6) Enlarged view of the white rectangle area in c5), where the similar layered structure is marked with red arrows. d) Lamellar-aligned BNNS/epoxy composite by BFC. d1) Schematic illustration of the fabrication process of aligned BNNS/epoxy composite. d2) Optical and SEM images of a BNNS aerogel, from which the long-range aligned lamellar structure is observed. e) Horizontally aligned PVDF/BNNS film by electrospinning and hot-pressing. e1) Scheme of the preparation process of PVDF/BNNS nanocomposite film. e2) SEM image of nanocomposite fibers with 33 wt% BNNS. e3) SEM image of the nanocomposite film with 33 wt% BNNS. f) BN-array/PDMS composite by DIW. f1) Optical photograph of a representative BN array/PDMS sample made with 6 × 6 BN rods. Inset shows the schematic diagram of thermal transport through the aligned BN nanosheets in the vertical direction. f2)-f4) show the temperature distributions of the PDMS, randomly distributed BN/PDMS, and BN array/PDMS samples sandwiched between Al blocks, respectively. A laser beam is applied to the top Al blocks as the heat source for all the samples. White dashed boxes indicate the location of these samples.

(a) Reproduced with permission [252]. Copyright 2014, Wiley-VCH. (b) Reproduced with permission [268]. Copyright 2011, American Chemical Society. (c) Reproduced with permission [278]. Copyright 2016, American Chemical Society. (d) Reproduced with permission [47]. Copyright 2019, Wiley-VCH. (e) Reproduced with permission [291]. Copyright 2019, American Chemical Society. (f) Reproduced with permission [210]. Copyright 2019, American Chemical Society.

CNTs/graphene film achieved horizontal and vertical thermal conductivity over 1000 $Wm^{-1}K^{-1}$ and 335 $Wm^{-1}K^{-1}$, respectively. Second, the defects within individual nanotubes such as lattice defects, impurities, and amorphous carbon also result in reduced thermal conductivities of CNTs as well as their composites. Various post-treatments including thermal annealing, nitric acid treatments, and solution centrifugation, [269,271,272] are effective strategies for improving the thermal conductivity of CNTs component. Third, the phonon modes of CNTs may be scattered or damped when contact with polymer matrix. For example, Gojny et al. found that the MWCNTs are more effective than single-walled CNTs (SWCNTs) in enhancing the thermal conductivity [273]. This is mainly because that the inner shells of MWCNTs enable efficient phonons conduction, although their outer shell is contacted with polymer matrix.

3.2.2. 2D aligned architectures

When spreading the heat from a chip on a circuit board, the heat spreader installed between the heat source and heat sink typically requires high thermal conductivity in their in-plane direction, so that the local heat accumulation condition can be released. Assembling the 1D and 2D fillers into a horizontally connected network can make full use of their high in-plane thermal conductivity, thus realizing superior thermal spreading ability. Compared with rigidly 1D aligned architecture, laminate-aligned structure is a more commonly used strategy for improving the thermal conductivity of polymers, since the contact area and overlapping of thermal fillers in the laminated structure are larger than those in the rigidly aligned structure. Either single fillers or hybrid fillers is commonly utilized to realize desired laminated heat conduction pathways. Compared with 1D fillers, 2D fillers are easier to be aligned into laminated structure due to their flake-like morphology. For instance, the layered and planar stacked 2D BNNS can be fabricated by a simple vacuum filtration process, [274,275] and their composite films which demonstrate highly anisotropic thermal performance are widely adopted in electronic packaging applications as heat spreaders. By virtue of this advantage, the overall loading fraction of these fillers can be reduced when the percolation of filler network within polymer matrix is accomplished. This can make up for the deterioration of mechanical properties and processability of composite materials caused by the incorporation of fillers.

The VAF approach, as discussed in Section 2.1, is a simple yet effective method to align the fillers into highly packed laminate structure. Through the shear force provided by the flowing suspension under the assistance of vacuum, the fillers tend to lie flatly above the filtration membrane, thus forming a highly planar-aligned thin skeleton. The most attractive point of this technique is, both rough implement and subtle control of filtration are feasible to realize well-aligned laminate structure, as long as the appropriate fillers are chosen. With the rough yet robust VAF process, 2D fillers such as graphene- and BN-based laminated composites can be fabricated without extra setup [276]. For example, Liang et al. reported an aligned functionalized multilayer graphene sheet (A-fMGs) in the in-plane direction. In their alignment method, the fMGs are dispersed in deionized water and vacuum-filtrated with an anodic aluminum oxide (AAO) filtration membrane. After washed by DI water, removed from membrane, and dried at 105 °C for 3 h, the obtained filtrated film demonstrated a high thermal conductivity of 112 $Wm^{-1}K^{-1}$ at RT [277]. Inspired by the natural nacre which demonstrates orderly layered structure and precise interfaces between inorganic platelets and organic matrix, Yao et al. reported on thermally conductive papers consisting of BNNS and GO fabricated by a simple VAF process (Fig. 8c). [278] The constituent fillers form a horizontally stacked laminate structure, in which the adjacent BNNS platelets are bridged by flexible GO (Fig. 8 c5, c6). Owing to the highly aligned layered structure and the strong lattice vibrational couplings between BNNS and GO, the composite film exhibited a high thermal conductivity of 29.8 $Wm^{-1}K^{-1}$ and high electrical insulation with a volume resistance of 7.95×10^{13} Ω·cm, which provides a creative opportunity for designing electrically insulating TIMs.

As an example of precisely controlled filtration, Kono et al. demonstrated a nearly perfectly aligned CNT film with in-plane thermal conductivity of 43 ± 2.2 $Wm^{-1}K^{-1}$ and a record-high thermal anisotropy of 500 for the time, [279] which is fabricated by their controlled vacuum filtration (CVF) approach. [127] Although the filtration setup in their technique was similar with traditional ones, some experimental details were carefully controlled, including that the surfactant concentration should be lower than the critical micelle concentration, the filler concentration should be below a threshold point, and the filtration speed must be below a low speed. By changing the surfactant and adjusting the filtration speed, the morphology of as-fabricated film can be altered from highly-aligned to poorly aligned (with thermal conductivity of 28 ± 1.2 $Wm^{-1}K^{-1}$), or even randomly aligned (14 ± 2.8 $Wm^{-1}K^{-1}$). It should be noted that in such a well-aligned structure, the inter-tube thermal resistance between adjacent CNTs has negligible effect on the heat conduction due to the large contact area between CNTs, since they are densely aligned in the same direction.

Ice-templating method is also applicable for creating laminate structure, since the growth kinetics of hexagonal ice that the crystallographic *a*-axis (parallel to the vertically induced temperature gradient) is 43–200% faster than that of *c*-axis, [280,281] and the ice dendrites grow rapidly in the direction of temperature gradient, simultaneously pushing fillers away from the moving front. After removal of ice crystals via sublimation, an elongated porous structure which contains aligned fillers paralleling to the direction of temperature gradient is obtained. Therefore, it seems that a cold finger is enough to provide the necessary driving force of achieving aligned lamellar structure in this method. However, the obtained porous structure varies a lot with different suspension characteristics, including fillers volume fraction, binders, and solidification velocity. In most cases when anisotropic freeze-casting technique is employed, lamellar is the predominant pore structure. Meanwhile, 'secondary arms' may emerge from the surface of ice crystals in the direction perpendicular to the temperature gradient. With the increase in both length and density of these dendritic side branches, the final morphology of ice will transfer from lamellar to dendritic, in which highly interconnected ice network has formed [282]. Typically, increased interconnectivity between adjacent filler walls can be realized by increasing filler loading, increasing solidification velocity, and addition of binders or cryoprotectants. Consequently, these different microstructures result in diverse thermal properties of the final composite materials.

Sun and Wong's group have conducted detailed research works regarding the attainable microstructures and their thermal characteristics by the ice-templated approach. In their reported work of vertically aligned and interconnected SiC nanowire (SiCNW) networks as fillers for polymer composites, [154] they found that the final architecture of the SiCNW network can be controlled by varying the solid concentration and the content of SCMC (as the binder). With the increase of SiCNW volume fraction from 0.76% to 2.17%, the viscosity of the suspension increases, thus the movement of SiCNW is restricted while the ice crystals still grow fast [283]. In such a situation, more fillers are trapped by the moving ice front, and laid perpendicular to the temperature gradient, bridging the neighboring lamellar filler slice. Finally, the obtained microstructure is close to a honeycomb-like morphology. As a result, the through-plane thermal conductivity of SiCNW/epoxy composites increases from 0.36 to 1.67 $Wm^{-1}K^{-1}$ with the increasing filler loading, while the anisotropy of thermal conductivity diminishes with the increase of SiCNW loading, which is mainly due to the change of microstructure morphology from well-aligned lamellar to honeycomb-like at a higher filler loading. Similarly, increasing the concentration of binder (SCMC) also results in an increase of suspension viscosity and perpendicularly interconnected bridges.

Above-mentioned UFC technique usually results in multiple submillimeter lamellar structures with different orientations within the system, which is adverse for the efficient thermal conduction. To

improve this issue, Bai et al. have developed the BFC technique that generates dual temperature gradients in both vertical and horizontal directions, by tactfully introducing a PDMS wedge between the cold finger and the suspension (Fig. 8 d1) [47,284]. Under this condition, the ice crystals grow in two directions, i.e., vertically from bottom to top, and horizontally from bottom end of the wedge to top end of the wedge. Consequently, a large-scale monodomain lamellar structure is obtained (Fig. 8 d2). It is validated that under the same BNNS filling load of 15 vol %, the uniaxially aligned BNNS/epoxy composite demonstrates a thermal conductivity of 1.9 $Wm^{-1}K^{-1}$, while that of biaxially aligned composite is as high as 6.07 $Wm^{-1}K^{-1}$. [47] With this method, they also obtained a BNNS/epoxy composite with thermal conductivity of 6.54 and 0.7 $Wm^{-1}K^{-1}$ in the direction parallel and perpendicular to the lamellar structure, respectively, with a BNNS loading of 20 vol%. Even with less filler loading, these thermal conductivity values are higher than those with traditional method and possess a thermal conduction anisotropy of 12, demonstrating the superiority of long-range lamellar structure in efficient thermal dissipation.

Electrospinning technique not merely can be utilized for aligning polymer molecules (as discussed in Section 3.1), but also can be adopted to fabricate polymer composites containing laminated aligned 1D and/or 2D fillers [285,286]. During the electrospinning process, the stretching of polymer fibers and orientation of fillers occur simultaneously, which benefits the construction of directional thermal conductive pathways within the in-plane direction. There are two strategies for fabricating polymer/filler composites by electrospinning. One is to directly spin the polymer/filler-mixed suspension, such as the PVA/BNNS fibers, [286] polyvinylidene fluoride (PVDF)/BNNS fibers, [287] and MWCNTs/epoxy nanofibers, [288] etc. In this manner, the fillers are randomly dispersed and embedded by intertangled molecular chain of polymer in the electrospinning suspension. The other is to spin the polymer fibers and electrostatic-spray the thermal conductive fillers separately, such as the PVA/BNNS membranes, [116] and the PVA/BNNS@Ag nanowire composites. [290] In this case, the sprayed fillers are attached onto the fibers surface via electrostatic interaction, which means that the fibers act as templates for fillers to form multiple linear-aligned thermally conductive pathways along the in-plane direction without the incorporation of low thermally conductive polymer. This may facilitate the efficient heat dissipation under appropriate fabrication conditions. It should be noted that, the thickness and density of the polymer nonwoven fabric, depending on the electrospinning duration, are the critical factors in deciding if all polymer fibers can receive the filler spray. If the fibers fabric is too dense or thick, the filler spray cannot reach the internal fibers. If the fabric is too sparse or thin, then the obtained fibers fabric cannot be peeled off from the cylindrical collector due to its poor mechanical strength [116].

In addition to fillers' alignment, the filler-filler and filler-polymer interfacial thermal resistances also play crucial roles in the final thermal conductivity of composites. Post-treatment procedure after electrospinning such as hot-pressing or annealing is necessary to enhance these interfacial contacts. [291,292] For instance, by hot-pressing the electrospun PVDF/BNNS film at 185 °C, Chen *et al.* achieved an oriented PVDF/BNNS composites with in-plane thermal conductivity of 10.4 $Wm^{-1}K^{-1}$ under 33 wt% BNNS loading (Fig. 8e). The calculated interfacial thermal resistance in the composites is about 1.26×10^{-6} m^2KW^{-1}, which is an order of magnitude small than that (1.81×10^{-6} m^2KW^{-1}) of composite with randomly dispersed BNNS. [291] Similarly, they further realized an electrospun PVA/BNNS nanocomposites with ultrahigh in-plane thermal conductivity of 21.4 $Wm^{-1}K^{-1}$ under 22 vol% BNNS addition [289].

By coating superparamagnetic or soft magnetism nanoparticles onto the surface of 2D fillers, it is also feasible to realize aligned lamellar structure by using external magnetic field to control the orientation and position of platelet fillers in polymer matrix. However, the reported thermal performances with this method are barely satisfactory. For instance, Yuan *et al.* reported on the magnetic aligned hBN platelets in silicone matrix and the obtained thermal conductivity of the composites with 9.14 vol% filler loading is 0.58 $Wm^{-1}K^{-1}$ [91]. Other researches which used this method also obtained poor thermal conductivity less than 1 $Wm^{-1}K^{-1}$ [28]. This phenomenon is mainly attributed to the inferior aligned structure which is confirmed by the reported micro-characterizations. Several factors contribute to the imperfect alignment of fillers. First, the overweight of filler makes it difficult to be tilted or oriented with magnetic nanoparticles under constant magnetic field. Second, the steric interactions between the fillers dominate when filling load increases, thus hindering the filler alignment. Therefore, modifications have been made to promote the filler alignment regarding these factors.

For examples, Yuan et al. proposed to use combined mechanical stimuli and rotating magnetic field to prepare well-aligned hBN-filled composites under filling load from 10 to 20 vol%. [293] In their experimental setup, the suspension was fastened on a vibrating table which could provide continuous mechanical vibration to the sample, and a magnet that is rotated with a fixed frequency of 5 Hz is applied to the sample for the formation of ordered filler structure. As a result, the thermal conductivity of composites was further improved to about 1.4 $Wm^{-1}K^{-1}$ at 20 vol% hBN filling fractions. Liu *et al.* proposed to use modified positively charged FeCo nanocubes as an assistant to help BNNS vertically aligned for forming thermal conduction channels. [294] Owing to the cubic morphology of nanoparticles and the lightweight of few-layer BNNS, the FeCo-BNNS complex materials are easier to be tilted by magnetic force. Consequently, the thermal conductivity of the composite films with 30 wt% and 50 wt% BNNS fillers reached 2.25 $Wm^{-1}K^{-1}$, which is 7 times higher than the unaligned composite sample with 50 wt% BNNS. In addition to BN, graphene derivates were also combined with magnetic nanoparticles to realize filler orientation, such as rGO@Fe_3O_4 nanocomposite, [295] graphene-Fe_3O_4/SiC composites, [296] etc. However, their large laminar size comparing to other 2D fillers hampers the efficient alignment under magnetic field, resulting in a relatively low enhancement of thermal conductivity. Using high magnetic field may be one of few strategies for improving the alignment of these composites. Chung *et al.* reported a large enhancement up to 330% of the through-plane thermal conductivity towards graphite fillers, with a 10 T superconducting magnet, and the thermal conductivity is as high as 4.5 $Wm^{-1}K^{-1}$ under 60 wt% filling loads [297].

3D printing is a versatile approach to enhance the thermal properties of polymer composites by orienting fillers with the assistance of shear force. Both light- and ink-based 3D printing techniques are effective to sculpt composites with laminated aligned fillers. For light-based 3D printing technique, the orientation of fillers is realized by the synthetic effect of gravity and shear force. As depicted in the work of DLP-based filler alignment by Wang et al. [298] the in-plane alignment of Al_2O_3 platelets in the slurry is achieved by the mechanically press of the printing platform. The orientation of fillers is more apparent when the printing layer thickness is thinner compared to the lateral size of filler. For instance, the thermal conductivity of composites with 30 wt% Al_2O_3 and printing layer thickness of 15 μm achieved 2.622 $Wm^{-1}K^{-1}$, which is about 14 times higher than the pure UV resin, while that with printing layer thickness of 50 μm is less than 1.5 $Wm^{-1}K^{-1}$. This is mainly because that the freedom for the orientation of the fillers increases with the increasing printing layer thickness, making the fillers to distribute more and more randomly.

Although light-based 3D printing methods enable high feature resolution, they are limited to printing with either photocurable resins or thermoplastic polymer powders. Instead, the ink-based 3D printing techniques such as DIW and FDM, provide a wider choice of raw materials in the form of printable inks. In these methods, the alignment of fillers is mainly realized by the shear force generated during the printing process. Thus, the alignment direction can be controlled by the printing direction of ink-filaments. For example, horizontally aligned BN/Al_2O_3-PDMS composites with high filler orientation degree above 90% and thermal conductivity of 3.64 $Wm^{-1}K^{-1}$ were obtained by the DIW

method. [299] Similarly, Liu et al. prepared the horizontally orientated hBN-filled TPU composites by the FDM approach. [300] Liang et al. reported on macroscale rods consisting of vertically aligned BNNS at the nanoscale by the DIW method in which the ink was printed along the vertical direction, and achieved a BNNS/PDMS composite with through-plane thermal conductivity up to 5.65 $Wm^{-1}K^{-1}$ (Fig. 8f), which demonstrated superior heat dissipation ability over pure PDMS and PDMS composite with randomly distributed BNNS. In these ink-based techniques, the formation of ink-filament is decided by both the properties of the raw materials including the density, surface tension, viscosity, and characteristic length of the ink, as well as the printing parameters including the velocity of the extruded ink and the nozzle diameter. [188] Generally, the requirement of rheological properties for the printable ink in vertically aligned case is stricter than that in horizontal aligned case, since the vertically extruded ink-filament must be stiff enough to retain their vertical shape without collapsing or bending, yet they should be smoothly extruded from the nozzle without clogging.

3.2.3. 3D network architecture

Since the total interface area of filler-matrix decreases with the increase of filler size, the improvement of heat transport efficiency follows the general rule of 3D > 2D > 1D > 0D. [301] Undoubtedly, the 3D interconnected filler network structure is more ideal for favoring the thermal conductivity of composites owing to their intrinsic continuous nanostructures. Although these 3D network structure cannot be rigidly termed as 'alignment', their regularly repeating characteristics are quite similar with those of above-mentioned aligned structures. Thus, we still briefly summarize these 3D network architectures for efficient thermal conduction.

A 3D porous template is always the cornerstone of 3D interconnected thermal conduction network, and two strategies are commonly utilized to prepare the 3D percolation framework. The first one is to grow thermal materials onto the template, which is typically realized by the CVD technique [302,303]. The CVD method is considered more effective in achieving high thermal conductivity of polymer composites, since the obtained 3D thermal network has an almost unspoiled crystalline structure with fewer structural defects. For example, Shen et al. reported a high-density 3D multilayer graphene web (MGW) by the Ni foam-templated CVD, and the MGW/epoxy composites achieved a high thermal conductivity of 8.8 $Wm^{-1}K^{-1}$ at a graphene loading of 8.3 wt%. [304] Zhang et al. also prepared a 3D diamond foam-based paraffin composites by the Cu foam-templated CVD. Even at a low diamond loading of 1.3 vol%, the thermal conductivity of the composites reached 6.7 $Wm^{-1}K^{-1}$ [305]. These remarkable thermal properties are rarely reported previously under identical loading of fillers. However, the high-cost and time-consuming features make this method unsuitable for mass production currently.

On the contrary, the second strategy that is more convenient to conduct, is to directly assemble fillers onto the 3D template. Porous polymer skeletons such as PU and melamine foams are the most widely adopted 3D templates, and the assembly of fillers onto their surface can be realized by immersing the templates into the dispersion liquid of targeting fillers. After dried and encapsulated with polymer matrix, polymer composite with excellent heat conducting properties is obtained. Simple yet effective, as demonstrated by Liu et al., a 3D graphene/epoxy composite based on PU sponge templates with ultrahigh thermal conductivity of 8.04 $Wm^{-1}K^{-1}$ was obtained under a low graphene loading of 6.8 wt%, which is comparable with the performance obtained by the CVD technique [306]. Similarly, GO coated melamine foam, [214] BNNS coated melamine foam, [172] and rGO coated PU foam, [307] etc., were also developed by using this 'dipping and drying' method. It should be noted that the coating of fillers onto the template surface is a spontaneous assembly process, driven by the electrostatic attraction or van der Waals forces, which means that the contact between adjacent fillers may be incompact and thus resulting in high interfacial thermal resistance. Take a step forward, Dai et al. proposed a dual-assembly method for preparing graphene-based thermally conductive composites [48,214]. As shown in Fig. 9a, b, this method adopts a porous PU thin film, instead of traditional thick PU sponge, as the 3D template for assembling graphene sheets on PU skeletons by typical solution-immersion process. Then, the graphene/PU film was post-assembled into large monolith by a continuous roll-to-roll equipment. Unlike traditional PU sponge which leads to a nonuniform assembly of graphene sheets on the skeleton, the porous PU film with thickness of ~500 μm (Fig. 9c, d) enable the uniform attachment of graphene sheets on entire surface of the PU skeleton (Fig. 9e, f). Therefore, highly ordered graphene network structure as well as reduced junction thermal resistance can be obtained by this dual-assembly strategy. Consequently, the as-prepared graphene composite exhibited superior thermal conductivity of 62.4 $Wm^{-1}K^{-1}$ at the graphene loading of about 13.3 vol%, giving an ultrahigh TCE over 2400% (per 1 vol% filler). Further, when a hot-pressing process was applied to the stacked graphene/PU film, the density and structural orientation of the graphene framework can be controlled, and highly ordered graphene sheets were obtained (Fig. 9g-i). [48] As a result, the graphene/epoxy composite achieved 117 $Wm^{-1}K^{-1}$and 13.4 $Wm^{-1}K^{-1}$ in the in-plane and out-of-plane direction, respectively, at the graphene loading of 24.7 vol%. This is the highest value reported for the graphene framework/polymer composite at the time.

In addition to the foam templates, microparticles were also utilized as templates to construct 3D heat conducting network. Compared with those random filler-filled thermal composites, the existence of these microparticles increase the interconnection probability of fillers, and thus the 3D filler network is easier to be built. There are two strategies of using the microparticles, one is to treat the microparticles as sacrificing templates, i.e., the microparticles are removed after the formation of 3D network. For example, sacrificial material NH_4HCO_3 were mixed with BN platelets to fabricate the 3D BN skeletons by hot-pressing. [308] NH_4HCO_3 acted as a constituent material that was decomposed into gas after the 3D interconnected BN foam was formed. By this strategy, 3D-BN/epoxy with thermal conductivity of 6.1 $Wm^{-1}K^{-1}$ at BN loading of 59.43 vol% was obtained. Other sacrificial materials such as salt and bubbles were also adopted to assist the construction of 3D network [309, 310]. The other strategy is to treat the microparticle templates as building blocks of the 3D network-based composite. Typically, the microplates used in this approach are thermoplastic polymer powders such as PS, PP, PVA, PE, etc. The fillers are self-assembled onto the polymer templates via electrostatic interactions or chemical adsorption, and the mixture is shaped into a monolith by hot-pressing. With this versatile method, numerous composites were fabricated, such as the graphene nanoplatelets (GNPs)-coated PP composites, [311] BNNS-coated PS composites, [312] and BNNS-coated PI composites, [313] etc. To realize successful self-assembly of fillers and templates, some surface treatments toward them are necessary to adjust their surface charges. For example, both the pristine PS microspheres and BNNS demonstrated negative zeta potentials, which is inaccessible for them to be self-assembled. By modifying the PS microspheres with poly(dislyldimethylammonium chloride) (PDDA), the PS@PDDA microsphere features a positive zeta potential, thus enabling the decoration of BNNS on their surface.

Table 1 concludes the thermal conduction properties of polymers and composites with aligned architectures in some representative works. Up to now (May 2023), the highest thermal conductivity of pure polymer nanofiber (PE nanofiber) and polymer film (PE film, without filler) are 104 $Wm^{-1}K^{-1}$ and 65 $Wm^{-1}K^{-1}$, respectively, both of which are achieved by drawing [108,109]. For the composite materials, the highest thermal conductivity is 397.9 $Wm^{-1}K^{-1}$ (in-plane), by using the vertically aligned CNTs interconnected with graphene films via SiC as building blocks and mesophase pitch as base material [314]. The highest thermal conductivity reinforcement with per 1 vol% filler is 2494%, which is achieved by highly ordered graphene/PU framework-epoxy [48].

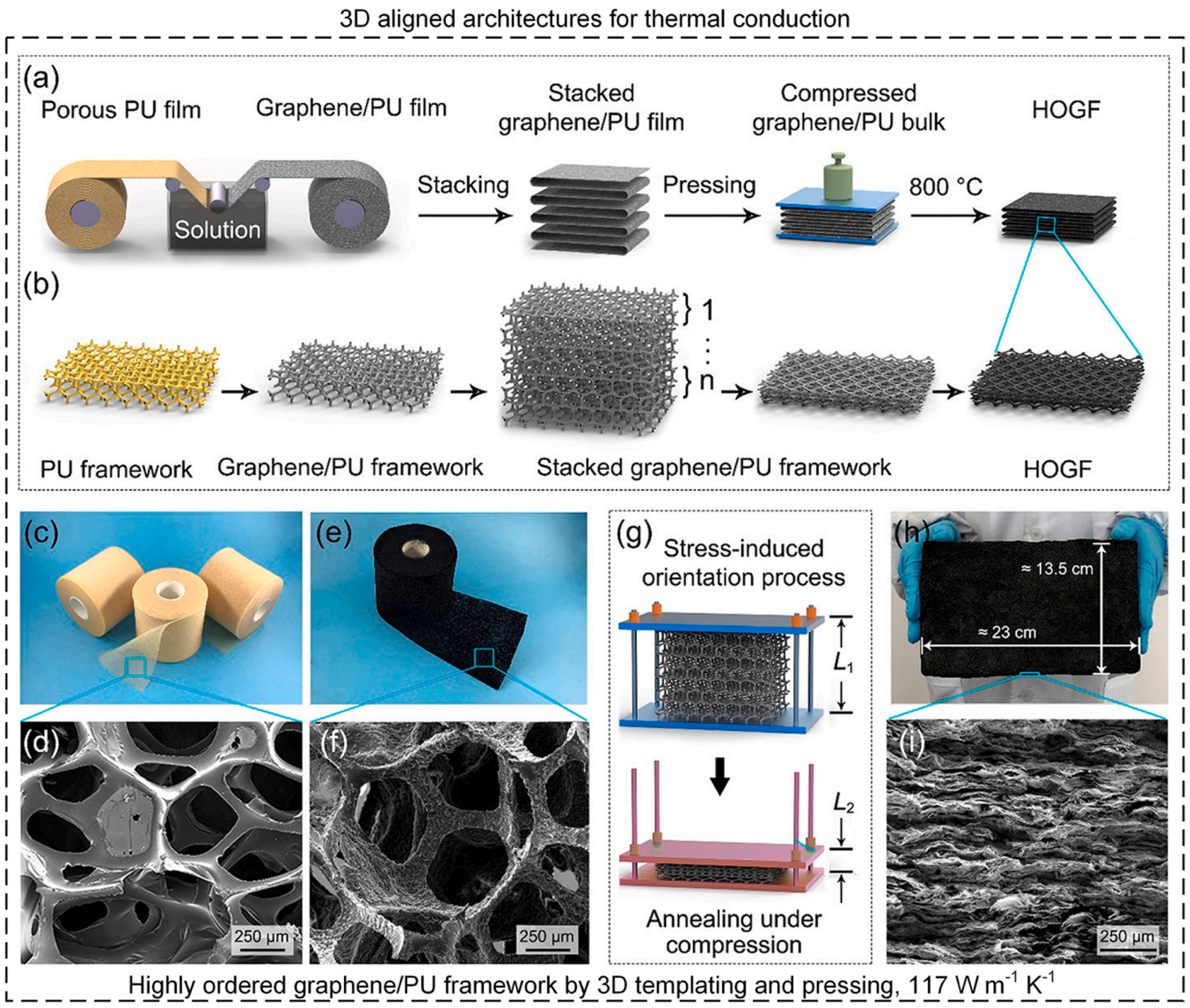

Fig. 9. 3D aligned graphene/PU framework by polymer templating and pressing. a) Schematic showing the fabrication process of the highly ordered graphene/PU framework. (b) The corresponding structural change of each step in a). c), d) Photograph and SEM image of porous PU film. e), f) Photograph and SEM image of graphene/PU composite film. g) Schematic showing the stress-induced orientation process. h), i) Photograph and SEM image of the as-prepared highly ordered graphene/PU framework.
Reproduced with permission [48]. Copyright 2021, American Chemical Society.

4. Alignment engineering for thermal insulation

Thermal insulation, contrary to the purpose of thermal conduction, is to retard the heat transport between two spaces to maintain a temperature difference. Thermal insulation materials are necessary to avoid undesired temperature changes of electronic devices, including not only temperature-sensitive microelectronics such as microelectromechanical systems (MEMS), [316] infrared detecting sensors, [317] and thermoelectric devices, [318] but also elaborate systems including gas turbine engines and aircrafts. [319] Besides, they are essential for controlling the interior environment of buildings which consumes over 10% of the global energy consumption, [320] as well as for maintaining human body temperature in the form of smart textiles and clothing systems [51].

Low-density, porous materials such as foams and aerogels are commonly identified as thermal insulation materials. As displayed in Fig. 10a, the heat transfer characteristics in these materials depend on the sum of solid conduction ($\lambda_{s,cond}$), gas conduction ($\lambda_{g,cond}$), gas convection ($\lambda_{g,conv}$), and radiation (λ_{rad}). Their effective thermal conductivity (λ_{eff}) can be expressed as [321].

$$\lambda_{eff} = \lambda_{s,cond} + \lambda_{g,cond} + \lambda_{g,conv} + \lambda_{rad} \quad (1)$$

where the contribution of gas convection is negligible when the air channels are severed into small-size micropores (< 1 mm) by the solid walls, since in such situation, the gas is unable to travel across a long distance to deliver heat (Fig. 10b). [322] The radiation contribution, which is proportional to the third power of object's temperature, is also negligible under ambient temperature and pressure conditions (Fig. 10c). Thus, the gas conduction and solid conduction dominate the effective thermal conductivity of porous materials.

As depicted in Fig. 10d, the gas conduction is strongly related to the pore size and the mean free path of air in the pores. Under ambient environments, the air molecules vibrate with a mean free path of 70 nm to deliver the heat, resulting in a thermal conductivity of 26 $mWm^{-1}K^{-1}$ for stationary air. When the pore size is below the mean free path of air molecular, the air molecule collisions are dramatically suppressed and

Table 1
Representative thermal conduction properties of polymers and polymer composites with aligned architectures achieved by various alignment techniques.

Alignment techniques	Matrix	Filler	Filler fraction	Aligned architecture	κ ($Wm^{-1}K^{-1}$)	κ Reinforcementby fillers	Year
magnetic field	epoxy	hBN	20 wt%	1D	$\kappa_{\perp} = 0.85$	23% per 1 wt%	2013[28]
	silicone	hBN	9.14 vol%	1D	$\kappa_{\perp} = 0.58$	24% per 1 vol%	2015[91]
	epoxy	hBN	20 vol%	1D	$\kappa_{\perp} = 1.4$	30% per 1 vol%	2016[293]
	PDMS	BNNS	50 wt%	1D	$\kappa_{\perp} = 2.25$	23% per 1 wt%	2019[294]
	epoxy	rGO@Fe_3O_4	30 wt%	1D	$\kappa_{\perp} = 0.61$	6% per 1 wt%	2021[295]
	epoxy	graphene	3.36 wt%	1D	$\kappa_{\perp} = 0.71$	93% per 1 wt%	2020[296]
	PVP	graphite	60 wt%	1D	$\kappa_{\perp} = 8.9$	53% per 1 wt%	2018[297]
	epoxy	CNT	3 wt%	1D	$\kappa_{\perp} = 6.5$	103% per 1 wt%	2003[256]
drawing	PE	none	none	1D	$\kappa_{//} = 62$	163 times	2019[45]
	PE nanofibers	none	none	1D	$\kappa_{//} = 104$	297 times	2010[108]
	PE	none	none	1D	$\kappa_{//} = 65$	217 times	2017[109]
	PE	BNNS	15 wt%	1D	$\kappa_{//} = 106$	2202% per 1 wt%	2020[110]
	PE	none	none	1D	$\kappa_{//} = 14$	25 times	1978[224]
	PE microfibers	none	none	1D	$\kappa_{//} = 51.8$	/	2017[226]
	PE nanofibers	none	none	1D	$\kappa_{//} = 90$	/	2018[227]
pressing	PVDF	diamond@SiC	70 wt%	2D	$\kappa_{iso} = 2.39$	16% per 1 wt%	2020[234]
	PE	hBN	35 wt%	2D	$\kappa_{\perp} = 3.11$	30% per 1 wt%	2020[257]
	PE	graphene	10 wt%	2D	$\kappa_{\perp} = 1.84$	46% per 1 wt%	2017[311]
	PS	BNNS	13.4 vol%	2D	$\kappa_{//} = 8$	71% per 1 vol%	2017[312]
	PI	BNNS	12.4 vol%	2D	$\kappa_{//} = 4.25$	32% per 1 vol%	2020[313]
VAF	PMMA	BNNS/graphene	29.3 vol%	2D	$\kappa_{//} = 4.03$	65% per 1 vol%	2019[122]
	PVA	graphene	93 wt%	2D	$\kappa_{//} = 61.3$	/	2019[123]
	cellulose	BNNS	70 wt%	2D	$\kappa_{//} = 30.25$	26% per 1 wt%	2017[274]
	graphene	none	none	2D	$\kappa_{//} = 112$	58 times	2011[277]
	BNNS	GO	/	2D	$\kappa_{//} = 29.8$	/	2016[278]
	CNT	none	none	2D	$\kappa_{//} = 43$	/	2019[279]
spinning	nylon-11	none	none	1D	$\kappa_{//} = 1.6$	6 times	2014[229]
	PS	none	none	1D	$\kappa_{//} = 14.4$	96 times	2014[230]
	PE	none	none	1D	$\kappa_{//} = 9.3$	20 times	2015[231]
	PBI	CNT	1.94 wt%	1D	$\kappa_{//} = 18$	1856% per 1 wt%	2013[239]
	PDMS	BNNS	15.6 vol%	1D	$\kappa_{//} = 1.94$	63% per 1 vol%	2017[286]
	PLA	AgNW	0.58 vol%	2D	$\kappa_{//} = 5.95$	258% per 1 vol%	2020[287]
	PVA	BNNS@AgNW	33 wt%	2D	$\kappa_{//} = 10.9$	119% per 1 wt%	2021[290]
	PVDF	BNNS	33 wt%	2D	$\kappa_{//} = 16.3$	57% per 1 wt%	2019[291]
	PVP	BNNS	5.52 vol%	2D	$\kappa_{//} = 3.24$	220% per 1 vol%	2021[292]
spinning & pressing	PVA	BNNS	33.1 wt%	2D	$\kappa_{//} = 21.4$	320% per 1 wt%	2019[289]
ice-templating	epoxy	BNNS	15 vol%	2D	$\kappa_{//} = 6.07$	211% per 1 vol%	2019[47]
	epoxy	SiC nanowires	2.17 vol%	2D	$\kappa_{\perp} = 1.67$	407% per 1 vol%	2018[154]
	epoxy	BN-rGO	13.16 vol%	2D	$\kappa_{\perp} = 5.05$	205% per 1 vol%	2018[166]
	PDMS	BN-SiC	8.35 vol%	3D	$\kappa_{\perp} = 3.87$	220% per 1 vol%	2020[233]
polymer-templating	epoxy	BNNS	1.1 vol%	3D	$\kappa_{\perp} = 0.6$	211% per 1 vol%	2018[172]
	epoxy	graphene	13.3 vol%	3D	$\kappa_{\perp} = 62.4$	2400% per 1 vol%	2021[214]
	epoxy	graphene	24.7 vol%	3D	$\kappa_{//} = 117$	2494% per 1 vol%	2021[48]
	epoxy	biomass-derived SiC	21 vol%	3D	$\kappa_{\perp} = 10.27$	259% per 1 vol%	2022[315]
templated-CVD	epoxy	SiC	3.74 vol%	3D	$\kappa_{\perp} = 14.32$	1613% per 1 vol%	2020[182]
	Al	diamond	4.6 vol%	3D	$\kappa_{iso} = 315.7$	12% per 1 vol%	2020[303]
	paraffin	diamond	1.3 vol%	3D	$\kappa_{iso} = 14.32$	1984% per 1 vol%	2019[305]
	Mesophase pitch	CNTs@SiC-graphene	/	3D	$\kappa_{\perp} = 41.7$, $\kappa_{//} = 397.9$	/	2023[314]
bubbles-templating	PDMS	BNNS	25.4 wt%	3D	$\kappa_{iso} = 1.58$	30% per 1 wt%	2020[186]
	PDMS	graphene	18.1 wt%	3D	$\kappa_{\perp} = 3$	84% per 1 wt%	2021[310]
light-based 3DP	UV resin	Al_2O_3	30 wt%	2D	$\kappa_{//} = 2.62$	43% per 1 wt%	2021[298]
ink-based 3DP	PDMS	BNNS	10.5 wt%	1D	$\kappa_{\perp} = 5.65$	70% per 1 wt%	2019[210]
	TPU	graphene	45 wt%	2D	$\kappa_{\perp} = 12$	104% per 1 wt%	2021[212]
	PDMS	BN/Al_2O_3	35/30 wt%	1D	$\kappa_{//} = 3.64$	36% per 1 wt% BN	2020[299]
	PU	hBN	25.9 vol%	1D	$\kappa_{//} = 2.56$	37% per 1 vol%	2019[300]

Note: '/' indicates data unavailable. $\kappa_{//}$ and $\kappa_{\perp}$ indicate the thermal conductivity of in-plane and through-plane direction, respectively, and κ_{iso} represents the isotropic thermal conductivity.

consequently the heat transfer is minimized due to the Knudsen effect [323]. Under this condition, the thermal conductivity of air $\lambda_{g,cond}$ can be expressed as:

$$\lambda_{g,cond} = \lambda_{g0,cond} \frac{\phi_g}{1 + \beta \frac{T}{P_g D_{cell}}} \quad (2)$$

Where $\lambda_{g0,cond}$ is the thermal conductivity of free air, ϕ_g is the volume fraction of air, β is the Knudsen coefficient, T is the ambient temperature, P_g is the air pressure inside the pores and D_{cell} is the diameter of the pores. From this equation, the gas conduction is in inverse proportion to the pore size, indicating that superior thermal insulation can be realized by reducing the pore size of porous materials. As validated by Notario et al., the thermal conductivity of polymeric foams can be significantly reduced from 17 to 7 $mWm^{-1}K^{-1}$ when the pore size decreased from 100 to 10 nm. [324].

The solid conduction in thermal insulation materials is dominated by phonon transport, since most of these materials are poor electrical conductors with few free electrons, such as silica aerogel, wood, and cellulose. According to the kinetic transport theory, [325] the solid conduction in these materials can be expressed as $\lambda_{s,cond} = c_{ph} \cdot l_{ph} \cdot v_{ph}/3$, where c_{ph} is the specific heat capacity, l_{ph} is the mean free path and v_{ph} is the velocity. From above equation, the solid conduction can be suppressed by increasing phonon scattering interfaces (Fig. 10e), including the solid-solid and solid-air interfaces. Thus, the mean free path of phonons can be shortened and total interfacial thermal resistance is elevated [326].

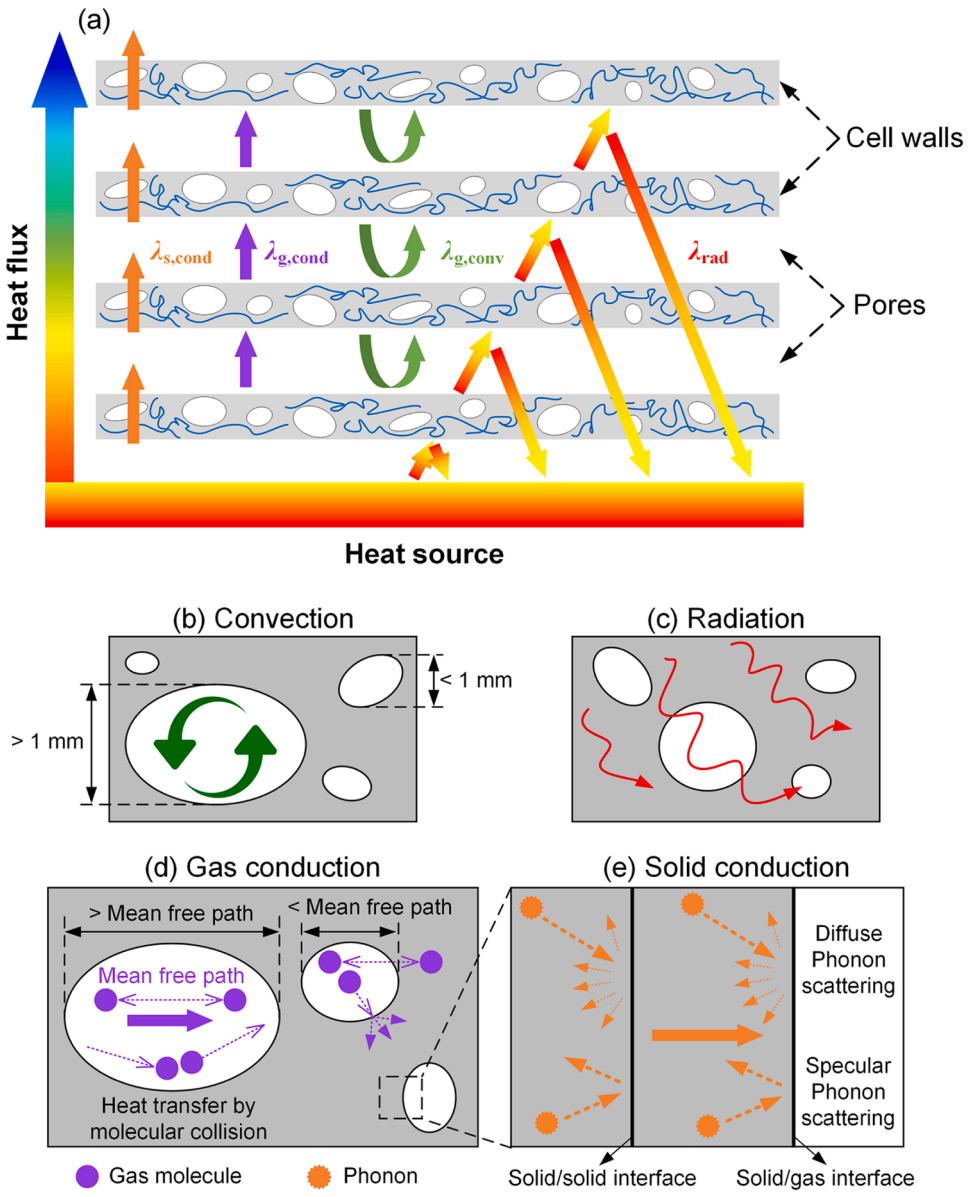

Fig. 10. Theory schematic of thermal insulation. a) Overall heat transfer process in thermal insulation materials. b)-e) indicates the detailed heat transfer situation of gas convection, radiation, gas conduction and solid conduction, respectively.
(a) Repainted with permission [51]. Copyright 2018, Wiley-VCH. (b-e) Repainted with permission [322]. Copyright 2020, Wiley-VCH.

Usually, there is a trade-off between the thermal conductivity of solid, gas and radiation. For examples, an increase of porosity will reduce the $\lambda_{s,cond}$, but will increase the $\lambda_{g,cond}$ and λ_{rad}, and thus may increase the λ_{eff}. A reduction in pore size can reduce the $\lambda_{g,cond}$, but it often decreases the porosity, which will increase the $\lambda_{s,cond}$. Therefore, it is quite challenging to lower the effective thermal conductivity of thermal insulation materials without the guidance of theoretical models. Recently, Shrestha et al. developed a unified model that can describe a wide variety of thermal transport behaviors within insulation materials, which may provide a broad guideline for the design and fabrication of high-performance thermal insulation materials. [327] According to the theoretical analysis, foams and aerogels with abundant tiny-pores and complex interfaces are the potential materials with thermal super-insulation properties. Following this guidance, researchers have developed various thermal insulation materials by engineering their porosity, pore structure and solid configuration. These materials can be divided into three categories, i.e., 1D fiber-like materials (synthetic hollow fibers, aerogel fibers, etc.), 2D hierarchical materials (carbonaceous aerogels, ceramic aerogels, etc.), and isotropic materials (silica aerogels, polymeric foams, etc.). Numerous alignment strategies toward the pore and solid structures in these materials have led to superior thermal insulation performance. Therefore, in this section, different aligned structures and their thermal insulating properties are discussed.

4.1. 1D nanofibrous aligned structures

People have made great effort to imitate the amazing features exhibited by other species on Earth. Striking thermal insulating feature has been shown by some animals living in the extremely cold zone such as the polar bear, whose skin is covered by thermally super-insulating hollow hairs (Fig. 11 a1-a3). Therefore, approaches to fabricate synthetic hollow fibers mimicking these animal hairs have attracted much attention because the wearable feature of fibers is superior to conventional aerogels. Bai et al. developed a freeze-spinning method (Fig. 11 a4), which subtly combines the freeze-casting and spinning techniques, to prepare the continuous silk fibroin fibers with aligned porous

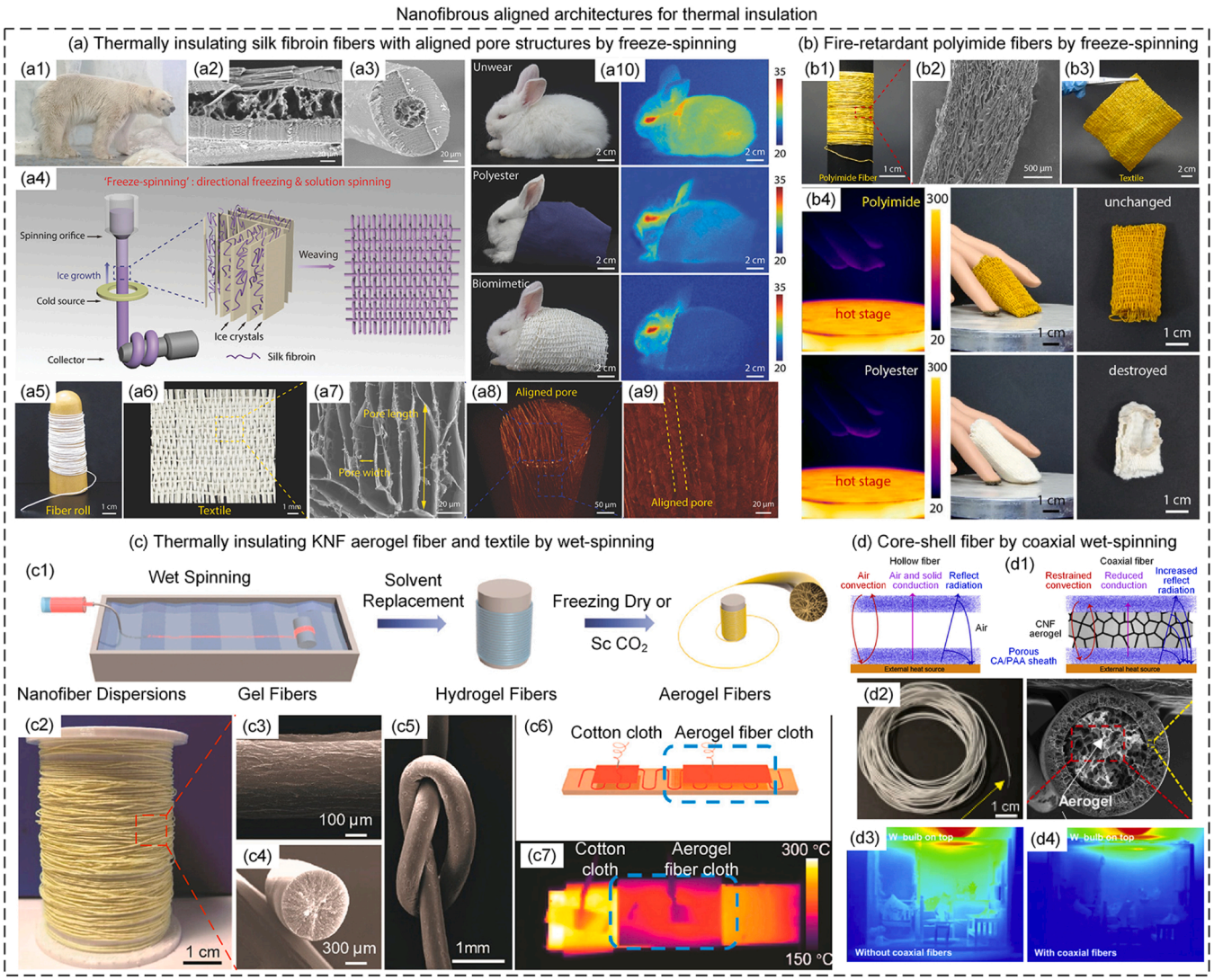

Fig. 11. Aligned fibrous architectures for thermal insulation. a) Thermally insulating silk fibroin fibers with aligned pore structures by freeze-spinning. a1) Photograph of a polar bear. a2, a3) SEM images of a polar bear hair showing the hollow core and aligned shell, respectively. (a4) Schematic of the freeze-spinning process. a5), a6) Optical image of porous fibers collected in a roll and woven in a textile, respectively. a7) Radial cross-sectional SEM image of a biomimetic porous fiber showing the typical structure. a8), a9) shows the X-ray computed microtomography images showing the axial aligned lamellar pores within the biomimetic fiber. b) Fire-retardant and thermally insulating polyimide fibers by freeze-spinning. b1), b2) shows the optical and SEM images of a polyimide fiber. b3) Optical image of a 10 × 10 cm^2 textile woven with the polyimide fiber. b4) Infrared and optical images showing a plastic finger touching a hot stage at 300 °C with polyimide and polyester finger-cots respectively. c) Thermally insulating KNF aerogel fiber and textile by wet-spinning. c1) Schematic showing the fabrication of KNF aerogel fibers. c2) Photograph of the aerogel fiber in a roll. c3)-c5) SEM images of the aerogel fiber and a fiber knot. c6) Schematic of the experimental setup for testing thermal insulation property of the aerogel textile and c7) the corresponding infrared thermal image. d) Core-shell fiber with CNF aerogel core and cellulose acetate shell by coaxial wet-spinning. d1) Schematic showing the thermal insulation mechanisms of the hollow and coaxial fibers. d2) Optical and cross-sectional SEM images of the coaxial fibers. d3), d4) Thermal images of the toy house in a simulated hot weather without and with the coaxial fiber mat on the roof, respectively.
(a) Reproduced with permission [51]. Copyright 2018, Wiley-VCH. (b) Reproduced with permission [151]. Copyright 2020, Elsevier. (c) Reproduced with permission [149]. Copyright 2019, American Chemical Society. (d) Reproduced with permission [329]. Copyright 2020, Elsevier.

structure. [51] In this method, the as-spun fiber passes through a freezing copper ring so that the ice crystals can grow directionally within the fiber, yielding a preferential ice pattern inside the fiber. After freeze-dried, porous structures that negatively duplicate the ice crystal patterns are generated in the fiber (Fig. 11 a5-a9). Similar with the typical freeze-casting process, the aligned pore structures in the fiber can be controlled by the solution viscosity, spinning speed, freezing temperature, etc. For instance, when the freezing temperature is increased from − 196 to − 40 °C, the average pore size increases from 20 to 85 μm. According to the measurement, the equivalent thermal conductivity of the fiber is 21.86 $mWm^{-1}K^{-1}$. When a textile (~0.4 mm) woven by the as-spun porous fibers was placed onto a hot plate, the temperature difference between the plate and the textile surface achieved about 8 °C, indicating its excellent thermal insulation property and making it a promising material for personal thermal management. As a proof of concept, the optical and infrared images of a rabbit wearing this biomimetic textile and a commercial polyester textile are shown in Fig. 11 a10. It is evident that the rabbit body covered with the biomimetic textile is almost invisible under infrared camera, indicating that the biomimetic textile is more efficient than commercial polyester in thermal insulation. Besides, these porous fibers demonstrate active electro-heating capacity when doped with CNTs, as well as outstanding underwater thermal insulation ability when coated with a hydrophobic SiO_2 layer. [328] The developed freeze-spinning technique can also be utilized to fabricate other porous fibers, such as the highly stretchable, fire-retardant, and thermally insulating polyimide (PI) fibers obtained

by implementing a thermal imidization process towards freeze-spun poly(amic acid) (PAA) fibers. [151] Fig. 11 b1-b3 show that the well-aligned pores obtained during freeze-spinning are reserved in the PI fibers after thermal imidization, and the fibers can be easily woven into a large piece of textile (100 cm^2), reflecting the stability and scalability of the fabrication process. As shown in Fig. 11 b4, when plastic fingers wearing the PI textile and polyester finger-cot respectively touch a hot stage at 300 ℃, the finger temperature in the polyester finger-cot increases rapidly and reaches around 262 ℃ within 60 s, resulting in the melting of polyester. Whereas, the finger temperature in the PI finger-cot increases much slower to 132 ℃ after thermal equilibrium, with the PI textile barely changes. This test has demonstrated the potential of aligned porous fibers in the thermal protective clothing area.

Wet-spinning is also a feasible method to prepare aerogel fibers with various aligned porous structures, which is conducted by extruding the well-dispersed nanofiber solution into a coagulation bath from the needle, and then followed by a drying process. Liu et al. reported a nanofibrous Kevlar (KNF) aerogel fiber fabricated by the wet-spinning process (Fig. 11 c1) [149]. The obtained fibers demonstrate robust mechanical performance with a tensile strength of 3.3 MPa and a strain of 35.2% under 2 wt% KNF dispersion, such that they can be tied into a knot or woven into a textile (Fig. 11 c2-c5). Besides, this aerogel fiber remains stable after heated to 300 ℃, and temperature difference between the fiber surface and hot surface reaches 90 ℃, indicting the aerogel's outstanding thermal insulation ability under high-temperature environment (Fig. 11 c6, c7). By subtly modifying the spinning nozzle into a core-shell structure, Zhou et al. reported a core-shell coaxial fiber with CNF aerogel core and stiff cellulose acetate porous shell. [329] As shown in Fig. 11 d1, d2, benefiting from the CNF aerogel inside the core that reduce the convection and conduction as well as increase reflect radiation, the coaxial fiber demonstrated better insulation performance than the typical hollow fiber. As a result, when heated to 150 ℃, the temperature difference of the fiber surface and the hotplate reach 54 ℃ and 41 ℃ for coaxial and hollow fiber textile, respectively. After 20 min of irradiation from a simulated summer heat of 100 W, the toy house with coaxial fiber mat on the roof displays lower temperature distribution than that without the mat (Fig. 11 d3, d4), suggesting that these porous coaxial fibers may open up new possibilities in biobased thermal insulation materials. One should be noticed that, although above-mentioned aerogel fibers were all treated by freeze-drying, the pore structures among different raw materials vary a lot, which has not been studied intensively by peer researchers.

4.2. 2D hierarchically aligned structures

Except for those thermally insulating textiles with the purpose of personal thermal management, most of thermal insulators are in the form of aerogel film or block. Thus, recent efforts have been made in the fabrication of highly porous aerogels assembled by 2D hierarchically aligned nanostructures, including ceramic aerogels, [52] polymer-based aerogels, [330] and cellulose-derivate aerogels. [322] These aerogels are anisotropic materials where the thermal conductivity in the through-plane direction is significantly lower than that in the in-plane direction. The anisotropic thermal conductivity is highly related to the intrinsic heat conduction anisotropy of the solid part, and the morphological anisotropy of both the walls and pores. Compared with conventional isotropic thermal insulators, the anisotropic thermal-insulating aerogels can prevent heat accumulation within the surface through their elevated in-plane thermal conductivity and reduce heat transfer in through-plane direction due to the lower thermal conductivity.

Ceramic aerogels. Ceramic aerogels, consisting of metal oxides (such as Al_2O_3, ZrO_2), nonmetallic compounds (such as silica, SiC, BN) or composite ceramics (such as Al_2SiO_5, $ZrSiO_4$), are effective thermal-insulators owing to their lightweight, low thermal conductivity (e.g. 12–20 $mWm^{-1}K^{-1}$ for silica aerogels), and superior fire-retardant characteristics [52,331]. Therefore, they have found their places in various thermal insulation fields, such as heat preservation of buildings and batteries, heat insulation of spacecrafts and furnaces, etc. However, traditional ceramic aerogels suffer from inherently brittle/fragile mechanical properties and crystallization-induced pulverization nature, [332] which have narrowed their field of application. To overcome this weakness, structural engineering strategies toward traditionally hard and stiff ceramics have been proposed, and elastic ceramic aerogels with robust mechanical and thermal stabilities were obtained. Currently, elastic ceramic aerogels can be realized by assembling flexible yet robust ceramic nanostructures such as BN aerogels, [333] and SiC nanowire aerogel, [334] which alter the aerogel structure from traditional necklace structure to fibrous-twining or layered-stacking configurations, respectively. For example, after interpenetrated with a silylated nanofibrillated cellulose (NFC), the inherently brittle silica aerogels were transformed into silica-NFC hybrid aerogels, showing improved compressive properties of 55% and 126% increase in Young's modulus and tensile strength, respectively, while maintaining low thermal conductivity less than 20 $mWm^{-1}K^{-1}$ [331]. However, these elastic ceramic aerogels fabricated by the in-situ crosslinking method or CVD method usually display a nanofibers/nanoplatelets-incorporated randomly distributed macroscale pore structure, which is inefficient in reducing the heat conduction comparing with those aerogels featuring ordered porous nanostructures. Meanwhile, their relatively low stiffness (specific modulus lower than 5 $kN{\cdot}m{\cdot}kg^{-1}$) also hinders their practical applications.

To further improve the insulation and mechanical properties of ceramic aerogels, Su et al. reported a SiC-SiO_2 core-shell (SiC@SiO_2) nanowire aerogel which exhibits an anisotropic and hierarchically aligned tubular pore microstructure [335]. UFC is adopted for preparing the SiC scaffold due to its advantage in forming well-interconnected hierarchical architecture by the anisotropic growing kinetic of ice crystals under temperature gradient. Then, to enhance its robustness, the scaffold is subjected to an air annealing process at 1000 °C for 20 min to enable the partial oxidation of SiC nanowires, thus forming a thin and amorphous SiO_2 shell on the nanowire surface. The tubular pores aligned along the axial direction provide multiscale thermal conducting barriers inside the aerogel, and the use of nanowire building blocks bring a large amount of extra tortuous solid conduction paths in the radial direction. In addition, the total interfacial thermal resistance is increased by the large amount of interface between amorphous silica and adjacent nanowires, and the stacking faults of the SiC whiskers. As a result, the thermal conductivities were measured as low as 14 and 35 $mWm^{-1}K^{-1}$ in the radial and axial direction, respectively. Besides, the dense cell walls of the aligned tubular pores enable robust connections between the building blocks, resulting in a specific modulus of ~24.7 $kN{\cdot}m{\cdot}kg^{-1}$, which is significantly higher than those aerogels with randomly distributed microstructure. On the basis of lamellar aligned and interconnected fibrous networks, enhancing the contact strength between ceramic fibers can leads to superelastic and high strength ceramic aerogels. Zhang et al. reported a ZrO_2-Al_2O_3 nanofibrous aerogels (ZrAlNFAs) in which the nanofibers are bonded by $Al(H_2PO_4)_3$, a widely used high-temperature adhesive in ceramic industry and refractory material fabrication. [336] The ZrO_2-Al_2O_3 nanofibers were firstly prepared by electro-spinning the mixture of ZrO_2-Al_2O_3 sol/PEO solution, and then the as-spun nanofibrous membranes were stacked layer-by-layer and immersed into the $Al(H_2PO_4)_3$ aqueous solution for crosslinking. Subsequently, the lamellar assembly was freeze-dried to form a nanofibrous porous structure with unbonded ZrO_2-Al_2O_3 fibers. Finally, the assembly was calcined in a muffle furnace at 800 ℃ for 1 h to endow the bonding of ZrO_2-Al_2O_3 fibers by the formation of orthorhombic $AlPO_4$. It is clearly observed from Fig. 12 b1, b2 that, in addition to the lamellar alignment of nanofibrous structure, the resulting ZrAlNFAs also demonstrated a bonding structure of nanofibers, enabling ability against mechanical deformation and thermal shock. Therefore, the as-formed lamellar multiarch ZrAlNFAs exhibited a recoverable

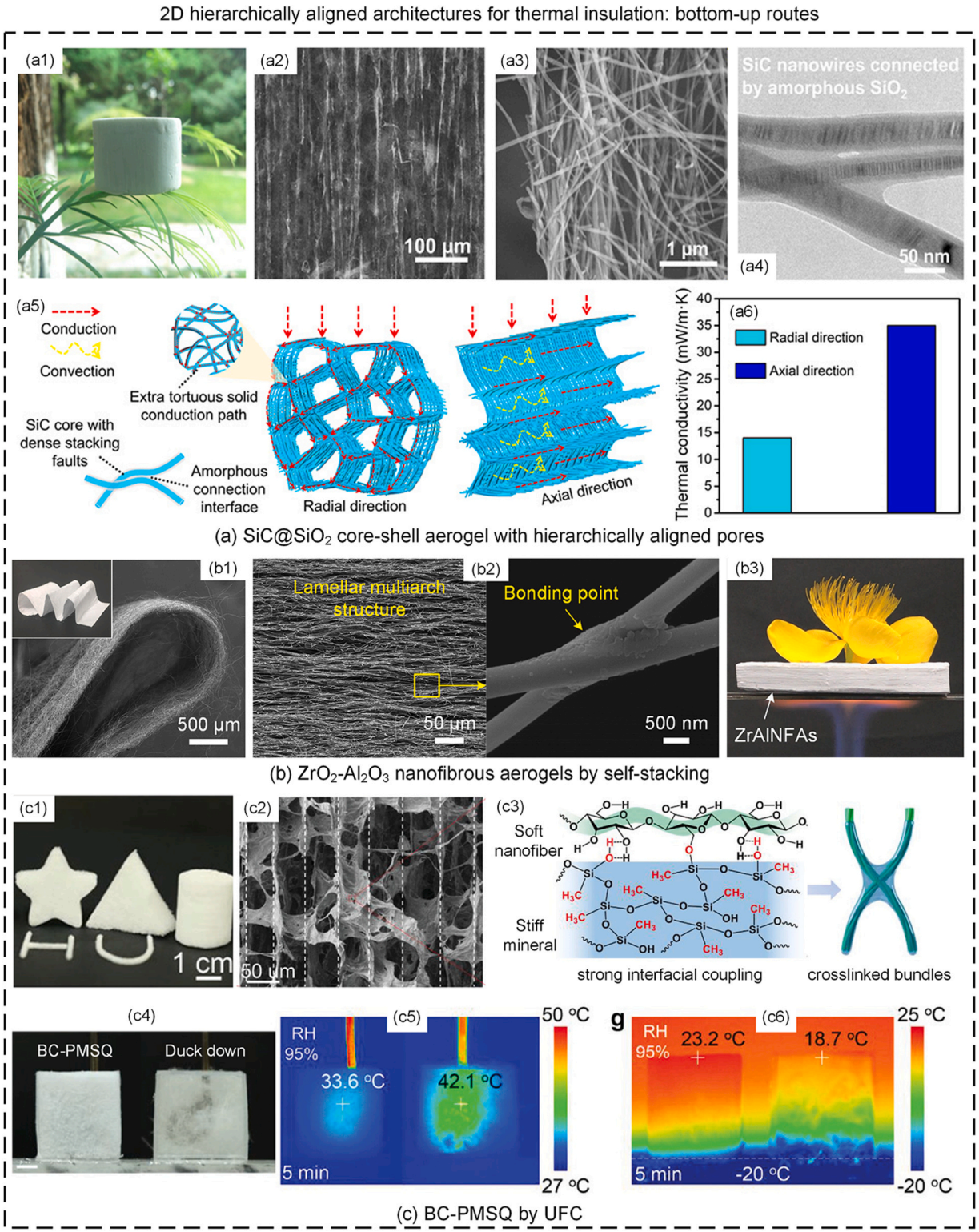

Fig. 12. Hierarchically aligned architectures for thermal insulation via bottom-up routes. a) SiC-SiO_2 core-shell nanowire aerogel. a1) Photograph of a piece of the aerogel standing on a leaf. a2), a3) SEM images of the aerogel with different magnifications. a4) High resolution TEM image showing the SiO_2 conjuction between nanowires. a5) Schematic diagram showing the thermal superinsulation mechanism of the aerogel. a6) The thermal conductivities of the aerogel in axial and radial directions. b) ZrAlNFAs by self-stacking. b1) SEM image and optical photograph (the inset) of ZrAlNFAs. b2) SEM images of the aerogel at different magnifications showing the lamellar architecture and the cross-linked networks between the nanofibers. b3) Illustration of superior thermal insulation performance of ZrAlNFAs. c) BC-PMSQ hybrid aerogels. c1) Photographs of BC-PMSQ aerogels with diverse geometrics and shapes. c2) SEM image of BC-PMSQ aerogel showing the anisotropic cellular architecture. c3) Schematic illustration of the hierarchical hybrid interfaces between BC nanofibers and PMSQ coatings. c4) optical image and c5) infrared image of BC-PMSQ and down feathers by inserting a 50 ℃ heating copper wire for 5 min at an RH of 95%. c6) Infrared image of BC-PMSQ and down feathers on a − 20 ℃ cooling plate for 5 min at RH of 95%.

(a) Reproduced with permission [335]. Copyright 2020, American Association for the Advancement of Science. (b) Reproduced with permission [336]. Copyright 2020, American Chemical Society. (c) Reproduced with permission [344]. Copyright 2021, Wiley-VCH.

strain up to 90% and a maximum stress of 1100 kPa, which is 1–2 orders of magnitude higher than other reported ceramic nanofibrous aerogels (10–100 kPa). [52,333,337,338] This aerogel has a thermal conductivity as low as 32.2 $mWm^{-1}K^{-1}$ along with maintained elastically resilient properties when heated to 1300 ºC (Fig. 12 b3), demonstrating its high thermal insulation ability and temperature-invariant compressibility over a wide usage scenario. Simple yet effective, Yang et al. proposed to add acetone into the UFC process of BNNS/PVA suspension to preparing BNNS/PVA aerogel with better thermal insulation and higher mechanical stability [339]. The acetone act as the antifreeze that reduce the freezing rate during UFC, leading to a thicker wall, lower density and higher porosity. As a result, the compressive moduli of the aerogel were reinforced by 210% and 280% in the axial and transverse directions, respectively, along with an ultralow thermal conductivity of 23.5 $mWm^{-1}K^{-1}$.

Nanocellulose aerogels. Renewable biomass materials such as wood chips and cork have been extensively adopted as thermal insulator for a long time. [340] However, their insulating ability is barely satisfactory with thermal conductivities of 40–50 $mWm^{-1}K^{-1}$. Fortunately, this condition has changed since the emergence of nanocellulose, an abundant biomass resource that can be extracted from the cell walls of plants and bacteria. Nanocellulose are nanofibers with diameter of 3–50 nm and length from 100 nm to several microns that demonstrate low density, high elastic modulus and flexible surface chemistry, making them possible to function as building blocks for generating high performance aerogels. Although nanocellulose aerogels suffer from high adsorption towards moisture which deteriorates their thermal insulation properties, different strategies have been proposed to tackle the moisture uptake issue, such as the crosslinking, hydrophobization and polyelectrolyte multilayers. [341,342] The anisotropic nanocellulose aerogels feature similar microstructures with natural wood, thus demonstrating both mechanically stiff and thermally insulating characteristics. There are two synthesis routes for preparing those nanocellulose aerogels. One is the bottom-up approach which includes extracting nanocellulose from plants, dispersing into solutions, and finally making into aerogels. The other is the top-down approach which starts from the chemical treatment of natural wood, followed by removal of other components within wood such as lignin and hemicellulose to obtain the nanocellulose aerogels. The bottom-up method is easier to realize wide design freedom in the pore/wall structure, while its fabrication cost and time consumption are relatively high, which may restrict the scalable applications of this approach. Inversely, the top-down method is more facile in its synthesis routes, but the microstructures of the obtained aerogels mainly depend on the original configurations of wood materials.

Regarding the bottom-up route, freeze-casting is the most commonly used technique to prepare anisotropic nanocellulose aerogels by aligning the nanocellulose fibers with the growth of anisotropic ice crystals. Adjustment of the freezing parameters enables facile control over pore size, pore density and pore alignment. Wicklein et al. reported on the fabrication of nanocomposite aerogels by freeze-casting the colloidal suspensions of CNF, GO and sepiolite nanorods (SEP) [156]. By applying a high cooling rate of 15 K/min, they obtained small aligned tubular pores with diameter of ~20 μm and wall thickness of 0.2–0.4 μm within the aerogels. Judging from the nitrogen adsorption isotherms tests, the cell walls are mesoporous with an average pore size of 3 nm. Benefiting from this nanosized components and their microstructure, the radial thermal conductivity of the nanocomposite aerogels is as low as 15 $mWm^{-1}K^{-1}$, which is significantly below the value of air. Further, during the variation of tubular pore size from 20 to 150 μm, the radial thermal conductivities barely change, indicating that the radial heat transport properties of the nanocomposite aerogels is dominated by the composition and microstructure of the cell walls, while the gas conduction is nearly identical. This result is also consistent with the Knudsen effect that the gas conduction can be significantly suppressed only when the pore size is reduced to below the mean free path of air (~70 nm). [323] Similar with that of ceramic fibers-based aerogels, the mechanical robustness of nanocellulose aerogels is unsatisfied due to the comparatively weak intermolecular interactions between nanocellulose, which has hampered their scope of applications. Organic alkoxysilanes, such as methyltrimethoxysilane (MTMS) are one of the auxiliaries for hybridizing nanocellulose to improve their mechanical strength [343]. Inspired by the tough bones where mesoscale fibrous network and microscale lamellar structure coexist through the combination of stiff calcium phosphate platelets and soft collagen fibrils, Zhang et al. developed hybrid aerogels consisting of bacterial cellulose (BC) and MTMS by the freeze-casting approach (Fig. 12 c1) [344]. The BC hierarchical network is first generated through freezing-induced assembly, and then stiff polymethylsilsesquioxane (PMSQ) is grown onto the soft BC network through the hydrolysis and condensation of MTMS. During this bottom-up fabrication process, the interconnected nanofibers cell walls are bridged and strengthened by the nanocoating of PMSQ, resulting in directional aligned porous aerogels with robust yet flexible interfacial interactions (Fig. 12 c2, c3). Owing to this full-scale "stiff--soft" synergistic structure, a maximum stress of 400.5 kPa at 99% strain along the pore alignment direction was achieved, and almost 80% maximum stress was reserved after 10000 compress-release cycles with a strain of 60%. Interesting, this BC-PMSQ hybrid aerogels was able to sustain a load of more than 10^7 times its own weight and recovered to its original shape completely. Such a superior compressible ability was rarely reported in other aerogels. Meanwhile, the hybrid aerogels demonstrate high porosity of $>$ 99% and low thermal conductivity of 28.9 $mWm^{-1}K^{-1}$ at room temperature, as well as superior thermal insulation property than down feathers even under high relative humidity (RH) of 95% (Fig. 12 c4-c6), indicating the effectiveness of PMSQ coating on the reinforcement of structural robustness and maintenance of thermal-insulating ability of nanocellulose aerogels. As another alternative for.

Recently, the top-down approach has found its place in preparing anisotropic, thermally insulating nanocellulose aerogels by virtue of its simple and direct chemical treatment routes toward natural wood. Typically, natural wood cell wall consists of three components, i.e., the paracrystalline cellulose fibers, amorphous heteropolysaccharide hemicellulose, and polyphenolpropane-based branched lignin. These components interconnect with each other, forming a robust and multifunctional cellular structure to transport nutrients and water from the roots to the leaves [345]. To reserve the porous and hierarchal aligned microstructures of wood, lignin and hemicellulose need to be removed. As reported by Hu's group, this can be realized by a two-step chemical treatment, i.e., first immersing the natural wood into a boiling mixed solution of $NaOH/Na_2SO_3$ to remove partial lignin and hemicellulose, followed by a treatment of H_2O_2 to remove the residual lignin (Fiugre 13a1) [346]. As a proof of concept, they treated American basswood by this method and obtained a thermal insulator made of aligned cellulose nanofibrils, which is referred as "nanowood" (Fig. 13 b1). [347] The nanowood inherits the original arrangement in natural wood yet exhibits a higher porosity (91%) in comparison with the natural wood. This is mainly attributed to the removal of intermixed lignin and hemicellulose which leads to much weaker solid conduction (Fig. 13 b2). The anisotropic thermal insulation property of the nanowood is originated from its anisotropic alignment structure, which is slightly divergent among different wood species. For example, with the same chemical treatment process, the aerogel obtained from balsa wood displays stacking-curved layers consisting of aligned nanocellulose fibers (Fig. 13 a2), [346] while that obtained from American basswood shows lamellar-aligned void channels separated by massive aligned nanocellulose fibers (Fig. 13 b3). [347] As a result of these aligned microstructures, the balsa wood aerogel achieves a low thermal conductivity of 28 $mWm^{-1}K^{-1}$ in the layer-stacking direction and 120 $mWm^{-1}K^{-1}$ in the cellulose-alignment direction. While, the nanowood exhibits 32 and 56 $mWm^{-1}K^{-1}$ in the radial and axial direction, respectively. Therefore, the top-down method demonstrates advantages such as simple, effective, and scalable, paving a new way for preparing nanocellulose aerogels

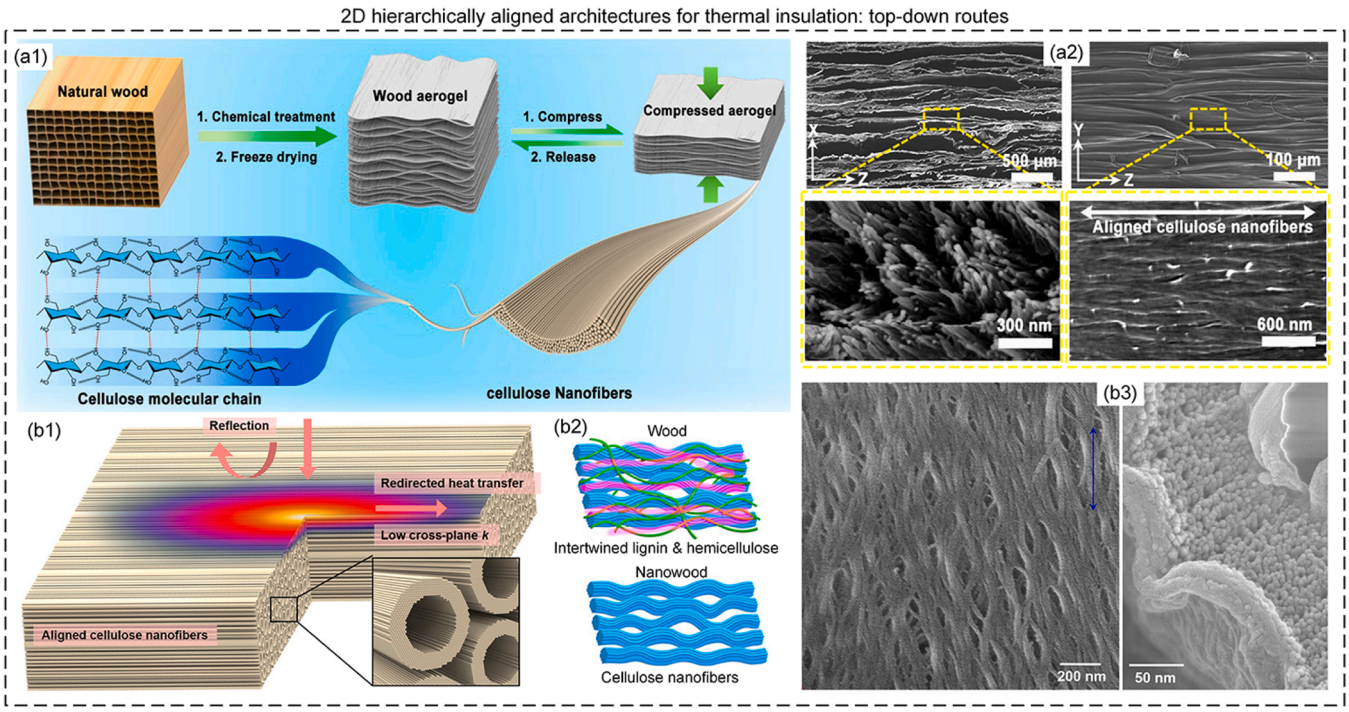

Fig. 13. Hierarchically aligned architectures for thermal insulation: top-down routes. a) Balsa wood aerogel by wood-templating. a1) Schematic illustration of the wood aerogel fabricated by a simple chemical treatment. a2) SEM images of the wood aerogel. b) Nanowood by wood-templating. b1) Schematics of the anisotropically thermal insulating properties of the nanowood. b2) Schematics of the aligned cellulose nanofibers in the nanowood before and after which the intermixed amorphous lignin and hemicellulose have been removed. b3) SEM images showing the side view (left) and top view (right) of aligned cellulose nanofibers. (a) Reproduced with permission [346]. Copyright 2018, American Chemical Society. (b) Reproduced with permission [347]. Copyright 2018, American Association for the Advancement of Science.

with anisotropic thermal insulating properties. Moreover, more researches are expected to conduct toward different wood species to find if there are any other unique nanostructures featuring better thermal and mechanical performances.

Polymer aerogels. Fossil-fuel-based polymer foams such as expanded polystyrene (EPS), PI and PU foams are currently used industrial thermal insulators. However, their thermal conductivities are slightly higher than air due to their macroscale, open pore structure which enable gas convection and conduction [348]. Compared with polymer foams, polymer aerogels have the potential to further reduce the thermal conductivity since their pore structure can be easily adjusted. Among these polymer aerogels, PI aerogels have drawn much attention with their excellent mechanical properties and high temperature stability. However, most of their thermal conductivities are in the range of 30–60 $mWm^{-1}K^{-1}$, which is still inferior to other aerogels. One of the main reasons is the shrinkage of PI aerogels during their formation, which results in apparent reduction of porosity and increase of density. [349] Since the thermal insulation performance is strongly related to the porosity and pore structure, effective strategies to reserve the pore structure of PI aerogels is urgently needed. Zhang et al. proposed to restrain the shrinkage and retain the structural integrity of PI aerogels by incorporating bacterial cellulose (BC) as a reinforcer, owing to its superfine nanofibrous structure [350]. The PI/BC aerogel prepared by the BFC technique exhibits well-aligned lamellar porous structure with pore size of ~10 μm and wall thickness of 1–2 μm, which results in distinct thermal conductivity in radial direction (44 $mWm^{-1}K^{-1}$) and axial direction (23 $mWm^{-1}K^{-1}$). This reduced thermal conductivity over conventional PI aerogels is the result of high porosity (up to 97%) and structural integrity. Actually, the addition of BC into the PI matrix successfully restrained the shrinkage rate of the aerogel from 36% to 17%, indicating that the BC can function as reinforcement to retain the pore structure left by ice crystal removal. It is worth noting that the pore structures of PI/BC aerogels prepared by bidirectional, random, and unidirectional freezing are quite different, so as their thermal conductivities. The aerogel prepared by random freezing show similar pore structures with pore size of 10–20 μm in both axial and radial directions, and their thermal conductivities in both directions are close to 42 $mWm^{-1}K^{-1}$. The aerogel prepared by unidirectional freezing show aligned tubular pore structures along the radial direction and honeycomb-like pore structures with pore size of 10–20 μm in the axial direction, featuring thermal conductivity of 37 $mWm^{-1}K^{-1}$ in radial direction and 66 $mWm^{-1}K^{-1}$ in axial direction, respectively. Among these aerogels, the aerogel prepared by bidirectional freezing shows the lowest radial thermal conductivity due to its absence of interlamellar heat conduction. The results support the idea that the thermal insulation performance of aerogel is decided by porosity and pore structure. As another proof of concept, Qin et al. reported a thermally super-insulating aerogel assembled by rGO and PI. By changing the mixing ratio of rGO and PI, the obtained aerogel exhibits different hierarchically aligned microstructures with high porosity. Under 30 wt% rGO content, nearly one-way lamellar microstructure in axial direction and honeycomb-like pore structure in radial direction were obtained. Due to the highly ordered microstructure and the existence of rGO nanosheets which decrease the volume shrinkage, the rGO/PI aerogel achieved an ultralow radial thermal conductivity of 12 $mWm^{-1}K^{-1}$ [351].

4.3. 3D isotropic structures

The above-mentioned works succeeded in minimizing gas conduction along the radial direction by implementing lamellar-aligned pore structures. However, these asymmetrical structures usually result in anisotropic thermal insulation properties with the radial direction exhibiting an ultralow thermal conductivity, whereas the axial direction a higher thermal conductivity. Although the elevated thermal conductivity in axial direction relieves the heat accumulation effect, it cannot satisfy the requirement of thermal insulation in all directions for specific

applications. To design all-directional thermal insulators, two critical factors should be considered. One is to minimize the solid conduction, which is typically conducted by reducing the content and wall thickness of the solid component. But this approach has faced its bottlenecks where further decrease of thermal conductivity leads to catastrophic deterioration of mechanical strength, and manufacturing feasibility. The other is to minimize the gas conduction and convection by reducing the pore size and creating isolated pores as much as possible, since closed pores are more effective in suppressing the heat transport of air, and thus results in lower thermal conductivity than mesoporous aerogels under the same solid fraction [352].

The emulsion templating is a facile approach in producing porous monoliths with both open and closed pores [353]. After the formation and solidification of an emulsion system, the external phase of the emulsion will turn into a solid skeleton and the internal phase will translate to voids with tunable size. Song et al. reported the fabrication of CNF/emulsion composite aerogel with quasi-closed micropores by the Pickering emulsion templating and solvent exchange techniques [354]. Massive droplets with diameter of 1–5 μm in the oil-in-water Pickering emulsion were formed and stabilized by 2,2,6,6-tetramethylpiperidine 1-oxyl (TEMPO)-oxidized CNF. The microemulsion structures were preserved by gelation and freeze-drying after a series of solvent exchange processes. Unlike traditional freeze-casting technique that creates open pore structures by the growth of ice crystals, the micropores produced by the Pickering emulsion templating are quasi-closed, which effectively suppress the gas conduction and convection. As a result, the CNF/emulsion aerogel exhibited an ultralow isotropic thermal conductivity of 15.5 $mWm^{-1}K^{-1}$, which is lower than previously reported cellulose-based aerogels, while maintaining durable flexibility and enhanced mechanical properties (specific modulus of 18.2 $kPa/(mg/cm^3)$) [329,347].

As another proof of closed cellular structure (CCS) concept, Yoo's group reported graphene-based CCS aerogels based on a microfluidic monodispersed synthesis approach [53]. As illustrated in Fig. 14a, under the gas-in-oil-in-water (G/O/W) interfacing condition, monodispersed microbubbles containing GO nanosheets were generated by a microfluidic device combining a hydrodynamic flow-focusing and co-flowing geometry. Then, these microbubbles were closely stacked by vacuum-assisted filtration and subjected to thermal annealing to form monolithic CCS (Fig. 14b-d). As a result, the obtained graphene bubble-assembled CCS (GBA-CCS) aerogel can better suppress the solid conduction as well as gaseous thermal transport than convectional open-pore aerogels (Fig. 14e). On one hand, the wall thickness of single GO microbubble as a building block can be minimized to even 50 nm (Fig. 14d), thus the solid conduction along the internal skeletons of GBA-CCS is efficiently suppressed. On the other hand, these closed pores would largely inhibit gas conduction and convection in all directions. consequently, the GBA-CCS demonstrated an extremely low, isotropic thermal conductivity of 5.75 $mWm^{-1}K^{-1}$, which is the lowest value among aerogel-based thermal insulators at the time. When the bottom of GBA-CCS block is heated to 200 ℃ for 60 min, the upper section of the block still maintains a lower temperature (~ 30 °C, Fig. 14f). Furthermore, owing to its structural interconnectivity and uniformity, this aerogel demonstrated fully elastic-responsive mechanical properties even after repeated tests of compression and recovery under torching-blowing conditions (Fig. 14g). The microfluidic-based technique provides a novel and general platform for preparing various highly CCS aerogels. Subsequently, Lee et al. also demonstrated that the distribution condition of GO nanosheets in the oil phase can be engineered by varying the GO concentration and size, and microbubble size. Thus, the GO nanosheets can be aligned into concentric, bipolar and transition morphologies [355]. By substituting the constituent materials with cellulose, ceramics or polymers, potential aerogels with elevated thermal insulating characteristics could be generated, which would boost the development of isotropic thermal-insulating materials, in our view.

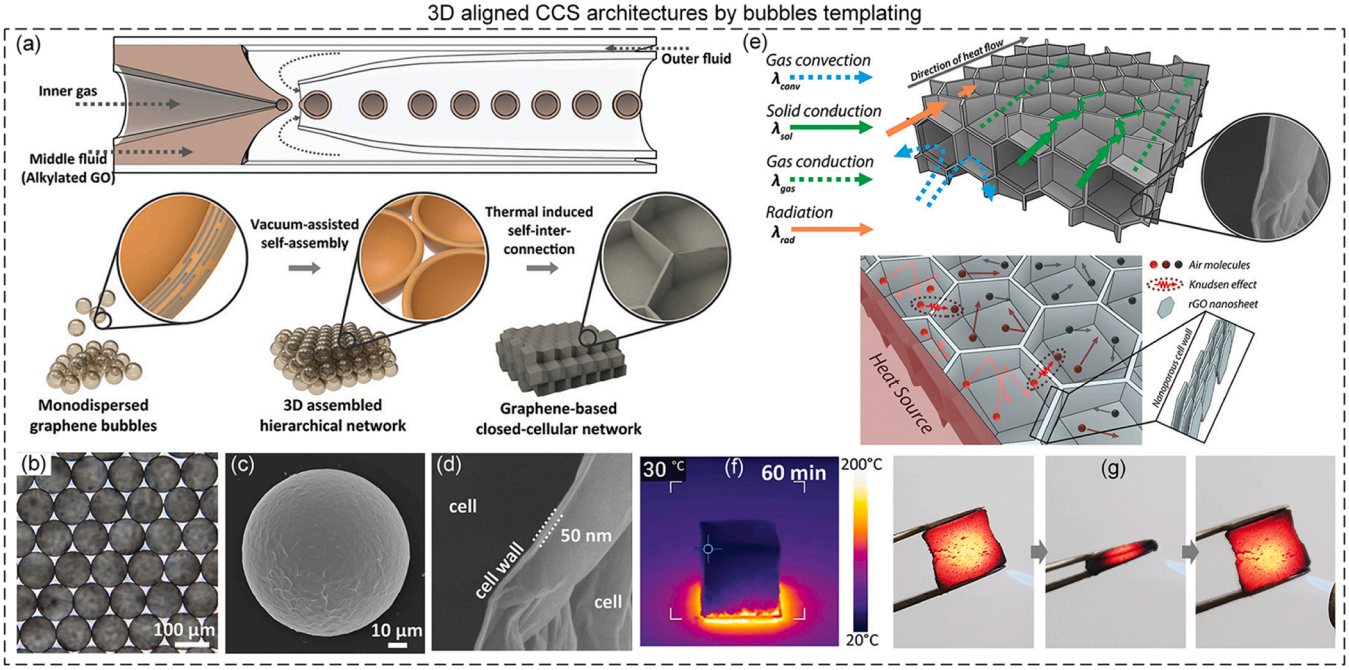

Fig. 14. Hierarchically aligned architectures for thermal insulation. a) Schematical fabrication process of GBA-CCS by the microfluidic synthesis of GO microbubbles, followed by the vacuum-assisted self-assembly and thermal reduction. b) Optical microscopic image of the 2D assembly of GO microbubbles. c) SEM image of the planar view of an individual GO microbubble. d) Cross-sectional SEM image of the GBA-CCS showing the interfacing wall after thermal reduction. e) Schematics showing the heat transfer mechanisms inside the GBA-CCS, and the restricted gas conduction by Kundsen effect through nanopores at the wall. f) Thermal image of the GBA-CCS heated on a hot plate of 200 ℃ for 60 min g) Repetition of the structural compression and recovery of GBA-CCS during the flame-retardant test. (a) Reproduced with permission [53]. Copyright 2021, Wiley-VCH.

5. Alignment engineering for thermal radiation

All objects with temperature above absolute 0 K uninterruptedly emit and absorb electromagnetic waves, which is also widely known as "thermal radiation". According to Wien's displacement law $\lambda_{max}T = 2.8976 \times 10^{-3}$ m K with λ_{max} the peak radiation wavelength and T the absolute surface temperature, thermal radiation wavelengths of most objects near room temperature on Earth fall into the infrared (IR) range (0.76–1000 μm), and thus cannot be perceived by the human eye which only respond to visible light ranging from 0.38 to 0.76 μm. Although invisible, thermal radiation are becoming increasingly indispensable to human beings from aspects of IR communication, climatology, thermography, thermal management, etc. Since thermal radiation can be considered a type of thermal energy emission from objects, two attractive phenomena, i.e., radiative thermal camouflage and radiative cooling have attracted much attention in thermal management field. Radiative thermal camouflage aims at hiding the IR radiation signature of a target into the background, by tuning the surface emissivity to make the detected thermal radiation power of the target close to that of its surroundings. [54,55] Differently, radiative cooling aims at maintaining a lower temperature of an object than that of its surroundings, by emitting heat to the ultracold outer space (~ 3 K) through the atmosphere transparency window ($\lambda \sim$ 3–5 and 8–14 μm) [56–58]. Though with distinct purposes, these two applications share similar design principles, i.e., engineering the thermal radiation properties of targeted objects by designing artificial materials including bio-inspired materials which mimic natural species, and metamaterials that are man-made inhomogeneous-structured materials. Surprisingly, alignment engineering approach has found its place in tuning the radiative properties of these distinctive thermal materials, by virtue of its superiority in constructing particular microstructures. In this Section, recent advances in radiative thermal camouflage and radiative cooling based on aligned structures are reviewed with an emphasis of the emerging strategies and materials.

5.1. Alignment engineering for radiative thermal camouflage

According to the Stefan-Boltzmann law, the radiative energy density Q of an object can be calculated by $Q = \varepsilon\sigma T$ [4], with ε the surface emissivity, σ the Stefan-Boltzmann constant and T the absolute temperature. Thus, thermal camouflaging can be realized by either dealing with temperature field or surface emissivity of targeted object, where the former is known as conductive thermal camouflage and the latter radiative thermal camouflage. Here we focus on the radiative thermal camouflage researches concerning alignment engineering techniques, and more comprehensive reviews regarding the recent progress of conductive, radiative, and dynamic thermal camouflage can be found in our other works. [54,356].

In most instances, the temperature of targeted object is higher than that of the background, and thus the requirement for radiative thermal camouflaging is to reduce the surface emissivity of the target. Many early researches focus on the design of low emissivity materials over the entire IR range, such as nanostructure-based surfaces or films, [357,358] so as to decrease the thermal radiation power. However, this will cause unexpected temperature rise of the object because the radiative thermal dissipation is suppressed, and thereby hinder the control of the IR signal. Moreover, low emissivity usually leads to high reflection, which will leave thermal signals in surrounding areas that can be detected. Therefore, the first priority is to maintain the equivalent thermal radiative energy between the target and the background. Considering that the mid-wavelength IR (MWIR) (3–5 μm) and long-wavelength IR (LWIR) (8–14 μm) signals feature high transmittance throughout the atmosphere, most IR detectors work in these two wavelength ranges (i.e., the atmospheric window) to cover a wide application field, while they are insensitive to the non-atmospheric window (5–8 μm). Thus, wavelength-selective emitters with low emissivity in the atmospheric window and high emissivity in the non-atmospheric window are expected to balance the IR stealth and radiative thermal dissipation [56, 359]. It should be noted that under circumstances where the background temperature is higher than the target temperature, the objective for emissivity is just opposite that the emissivity within the atmospheric window should be high to enhance the thermal radiation of the target, while the emissivity in other wavelengths should be low to reduce the radiative energy loss.

Following above design principles, various emissivity-engineered emitters were developed, including photonic crystals, plasmonic metasurfaces, phase-change materials, ferroelectric materials, etc. [348] Among these materials, aligned nanostructures are found to be effective in engineering the emissivity. Moghimi et al. reported on broadband IR stealth sheets based on the combination of vertically aligned silicon nanowires (SiNWs), randomly distributed silver nanoparticles (AgNPs) and a flexible polyimide substrate (Fig. 15 a1, a2). [360] The SiNWs act as reflection suppressant and scattering centers to disrupt the thermal emission, and AgNPs efficiently reduce the thermal transmission by virtue of their high absorption coefficient. As a result, 95% of the thermal radiation is absorbed by SiNWs and AgNPs and then turned into heat. Owing to the predesigned air-cooling channels below the substrate, the generated heat can be dissipated out without causing significant temperature rise. The IR stealth performance of this sheet is validated in Fig. 15 a3, a4, from which the thermal images of human model are easily captured without the stealth sheet. After covered by the sheet, the model is completely blended into its surroundings and is undetectable to the IR camera. Furthermore, by combining with addressable micro-emitters, the sheet is able to present false thermal signature to deceive IR detectors, indicating its multifunctional thermal camouflage properties. However, this IR stealth sheet features low emissivity across a wide range from 2.5 to 15.5 μm without wavelength-selective characteristics, which can only work at relatively low background temperature. To achieve better thermal camouflage performance, more subtle aligned nanostructures are demanded to fabricate wavelength-selective emitters. From this aspect, the state-of-the-art wavelength-selective emitters have provided much designing guidance, such as the periodic structures demonstrated by photonic crystals and metamaterials [361,362].

Recently, Ko et al. presented a polarization-dependent infrared emission regulator based on the non-volatile phase change material-$Ge_2Sb_2Te_5$ (GST) [363]. The self-aligned GST nanocolumns (SANCs) on Au substrate (Fig. 15 b1) were fabricated by a glancing angle deposition process. The fabricated structure shows polarization-sensitive thermal regulation through IR spectroscopic measurement. As a demonstration of thermal camouflage (Fig. 15 b2, b3), several SANCs were orthogonally placed onto the target object. Under unpolarized light, all SANCs show the same emissivity, thus exhibiting the same thermal emission (Fig. 15 b4). Whereas under polarized light, they display different emissivities corresponding to each position in the pre-arranged direction, which can unveil the encrypted information. Compared with other adaptive thermal camouflage systems that need extra energy input to tune the emissivity of the target object, this structure provides a facile emissivity regulation strategy without heat energy consumption, which may promote the development of adaptive thermal camouflaging materials.

5.2. Alignment engineering for radiative cooling

The concept of radiative cooling is proposed based on the radiative energy exchange between an object on Earth and the outer universe. Since the universe can be regarded as endless cold source due to its ~ 3 K temperature comparing with terrestrial objects on this planet (~ 300 K), terrestrial objects are able to deliver their heat into the universe in terms of thermal radiation and thus lower their temperature, as long as this thermal radiative pathway is unimpeded. This passive radiative cooling process sends excessive heat to the universe at no additional energy cost,

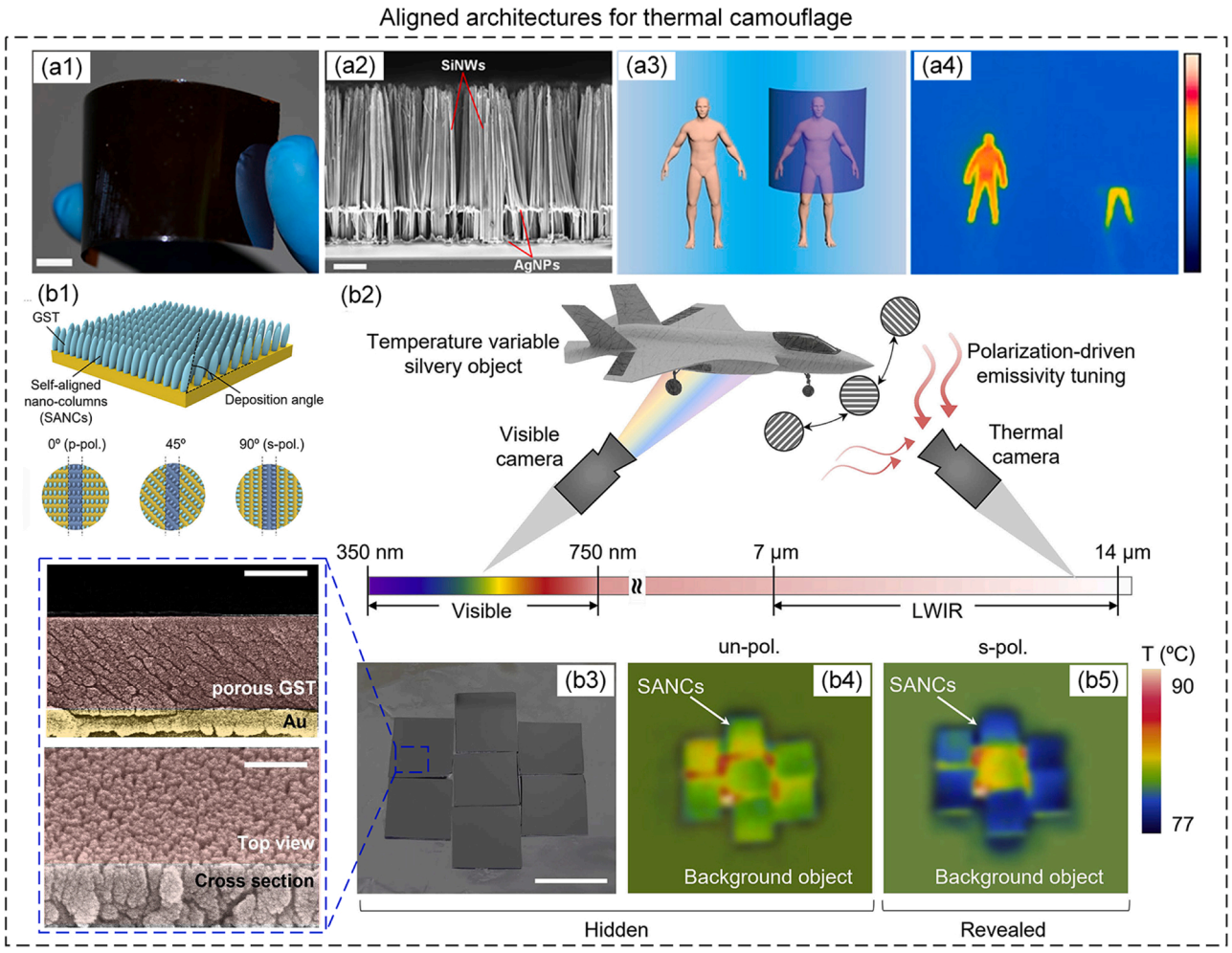

Fig. 15. IR stealth sheet with vertically aligned SiNWs arrays for thermal camouflage. a) Schematics of the stealth sheet with nanoscale absorbers, thermal insulation and micro-emitters. a1) Photograph and a2) SEM images of the stealth sheet. d) A human model with and without the stealth sheet. A3) IR images of the human model. The model without the stealth sheet is fully detectable while the top half of the model covered by the sheet is undetectable. b1) Schematic showing the self-aligned nanocolumns with top views according to different polarization angles. b2) Conceptional schematic showing the visibly and thermally camouflaged patch and patten indication process based on modulation of the polarization angle. b3) Photograph of SANCs on Au substrate attached on the surface of temperature variable object. Insets show the SEM images of the SANCs on Au layer with different viewing angles. b4) IR image of hidden state under unpolarized light. b5) IR image of the identified state based on application of linear polarization.
(a) Reproduced with permission [360]. Copyright 2018, Wiley-VCH. (b) Reproduced with permission [363]. Copyright 2023, Elsevier.

hence has emerged as a promising strategy to relieve urban heat islands effect and withstand global warming if it is widely happened.

However, the task of realizing passive radiative cooling, especially cooling an object to below its ambient temperature, is quite challenging. Considering the radiative cooling process in the presence of sunlight, the net radiative cooling power of an object ($P_{net}(T)$) is calculated as

$$P_{net}(T) = P_{rad}(T) - P_{atm}(T_{amb}) - P_{solar} - P_{cond+conv} \quad (3)$$

where $P_{rad}(T)$ is the radiative heat power emitted out to the universe, $P_{atm}(T_{amb})$ and P_{solar} is the radiative heat power absorbed from the atmosphere and the Sun, respectively, and $P_{cond+conv}$ is the conductive and convective heat power absorbed from the ambient. Therefore, two prerequisites should be satisfied before reaching this task. One is to maximize the surface emissivity within the atmospheric window to maximize the radiative energy output, and the other is to minimize the absorptivity within wavelengths at which solar energy is non-negligible (0.3–2.5 μm) to resist radiative energy input. However, meeting these requirements simultaneously is quite stringent because it calls for surface emissivity engineering of an object over a wide wavelength range which covers nearly two orders of magnitude.

Although some of the photonic materials, including photonic crystals and multilayered metamaterials, [56,364–366] have been demonstrated to realize efficient daytime radiative cooling ability, their expensive and sophisticated fabrication processes hinder their mass production and large-scale utilization. Fortunately, natural species give us some inspirations in engineering advanced materials that demonstrate sub-ambient daytime radiative cooling performances as well as advantage of easy fabrication. For instance, the Saharan silver ants successfully survive in one of the hottest lands on Earth, by virtue of their dense and locally aligned hairs that are uniformly covered on their body (Fig. 16 a1, a2). [27] These hairs feature a triangular cross-sectional microstructure with two corrugated top facets and a flat bottom facet facing their body (Fig. 16 a3). As incident angle of thermal radiation increased to a critical value of 30°, total internal reflection (TIR) occurs at the flat bottom facets of the hairs, resulting in strong enhancement of reflectivity. These unique structures of their hairs not only enhance their reflectivity within the visible and near infrared range to refuse input thermal radiation, but also reinforce their emissivity in the mid infrared range to efficiently dissipate heat back to the surroundings. Experiments have validated that, specimens covered with these hairs could keep lower body temperatures than those without hairs, demonstrating their

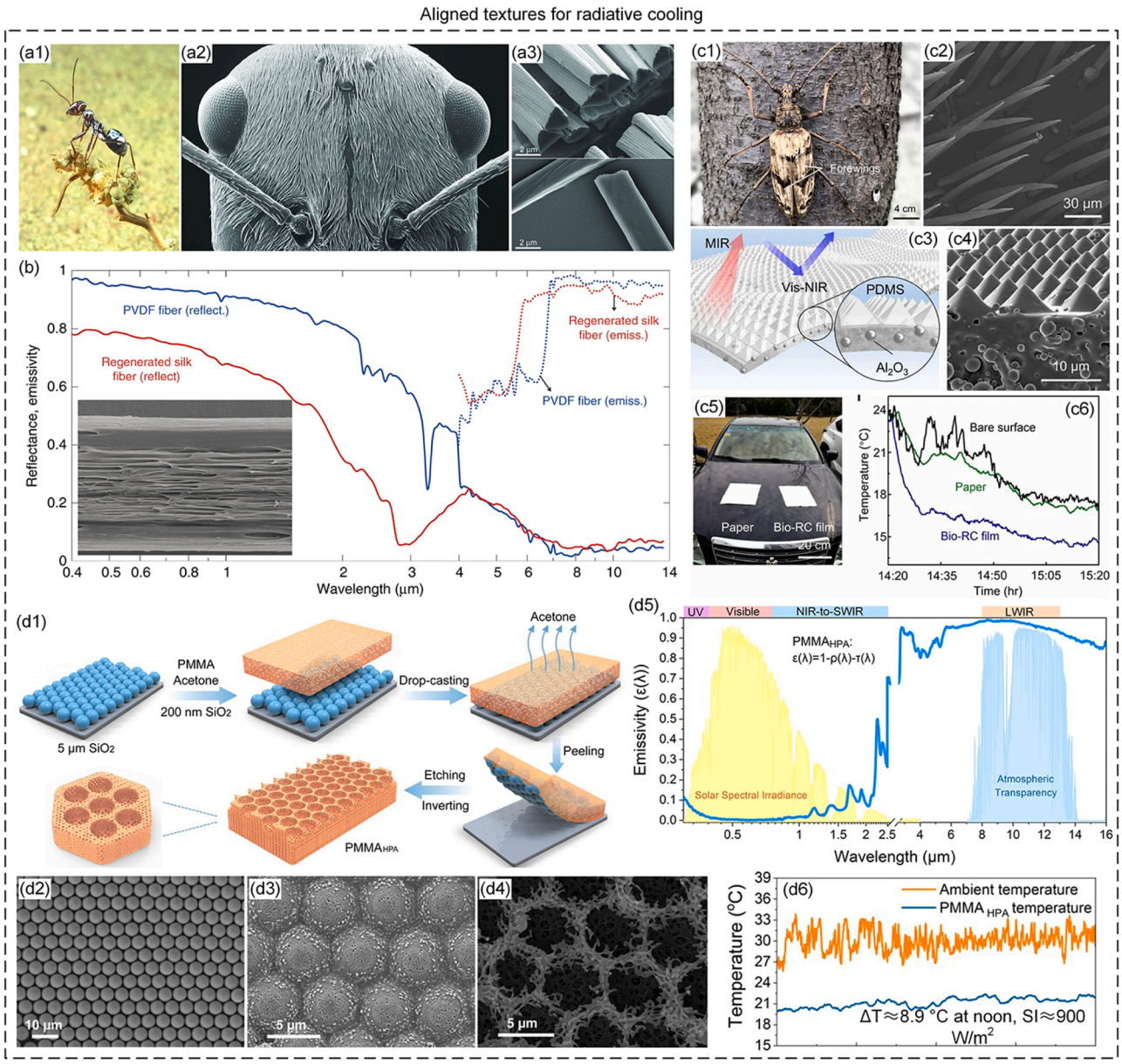

Fig. 16. Aligned textures for radiative cooling. a) Locally aligned hairs of Saharan silver ants for radiative cooling. a1) Photograph of a silver ant offloading heat on a top of dry vegetation. a2) SEM image showing the head of silver ant densely covered by hairs. a3) SEM images showing the cross-sectional morphologies of the hairs. b) Integrated hemispherical reflectance and emissivity spectra of regenerated silk fibers and PVDF fibers with high density of internal voids for radiative cooling. Inset shows the SEM image of longitudinal cross-section of a PVDF fiber, from which the high density aligned voids can be observed. c) Periodically aligned PDMS micro-pyramid arrays for radiative cooling. c1) Photograph of a male *Neocerambyx gigas*. c2) SEM image of the dense fluffs covering on the forewing of *Neocerambyx gigas*. c3) Schematic illustration of the Bio-RC film where ceramic particles are embedded in the PDMS matrix filled by compact arrays of micropyramids. c4) SEM image of the section of the Bio-RC film showing the micropyramids arrays. c5) Photograph and (c6) corresponding temperature variation of a piece of paper and the Bio-RC film on the surface of a car hood. d) Periodically aligned micropores array on PMMA film for radiative cooling. d1) Schematic illustration of the fabrication of $PMMA_{HPA}$ film with a hierarchically porous array. d2, d3) SEM images of hexagonally close-packed monolayer SiO_2 templates. d4) SEM image of $PMMA_{HPA}$ film showing an ordered symmetrical micropores array made of hierarchical randomized nanopores. d5) Spectral emissivity of the PMMAHPA film with ~160 μm effective thickness along with the normalized ASTM G173 Global solar spectrum and the LWIR atmospheric transparency window. d6) Temperature variation of the ambient and the PMMAHPA film under solar intensity (SI) of ~ 900 W m^{-2} and RH of ~ 44%.
(a) Reproduced with permission [27]. Copyright 2015, American Association for the Advancement of Science. (b) Reproduced with permission [367]. Copyright 2018, Nature Publishing Group. (c) Reproduced with permission [369]. Copyright 2020, National Academy of Science. (d) Reproduced with permission [370]. Copyright 2021, Nature Publishing Group.

effectiveness in daytime subambient radiative cooling. After that, more biophotonic alignment structures with excellent thermoregulatory functions were discovered from nature, such as the one-dimensional aligned porous silk of cocoon, [367] shell/hollow cylinder-like hairs of white beetles, [368] dual-scale fluffs of golden longicorn, [369] etc. These fascinating microstructures have shed light on the design and fabrication of advanced wavelength-selective materials for radiative cooling. It is easy to find that the powerful nature has shown us two ways for constructing advanced radiative cooling materials, one is based on fibers with filamentary-aligned pores, and the other is based on meta-surfaces with laminate-aligned surface textures.

Inspired by the longitudinal aligned voids structure in the silk

cocoon, Shi et al. fabricated biomimetic fibers with regenerated silk fibroin and PVDF by the wet-spinning technique. [367] The filamentary aligned air voids in these fibers have comparable sizes to visible and near-infrared light, leading to highly scattering and reflecting toward solar radiation. Meanwhile, the variety of chemical bonds in silk proteins intrinsically leads to high emissivity within the mid-infrared range. Based on the synergy effect of these characteristics, the nanostructured PVDF fibers demonstrate a solar reflectivity of 0.93 and an emissivity of 0.91 within the atmospheric window (Fig. 15b). It is a pity that they did not characterize the radiative cooling performance of these fibers. Nevertheless, took steps along this path, their group developed hierarchically porous poly(vinylidene fluoride-co-hexafluoropropene) [P(VdF-HFP)$_{HP}$] coatings with solar reflectivity of 0.96 and LWIR emissivity of 0.97. [359] The high solar reflectance is originated from the strong backscattering effect of micro/nano-pores toward sunlight, and the high LWIR emittance is due to the multiple extinction peaks of P(VdF-HFP) polymer in the LWIR window that are arise from the multiple vibrational modes of its molecular structure. The high solar reflectance and LWIR emissivity allow P(VdF-HFP)$_{HP}$ coatings to achieve subambient cooling of ~ 6 ºC and cooling power of 96 W m^{-2} under peak solar radiation intensity of ~ 890 W m^{-2}.

Mimicking the biological photonic structures with sequentially aligned surface textures is also a promising strategy for designing passive radiative cooling materials. For instance, Zhang et al. reported on a design of flexible hybrid photonic films by the microstamping method. [369] Mimicking the dual-scale triangular-shaped fluffs of longicorn beetle *Neocerambyx gigas* (Fig. 15 c1, c2), the bioinspired radiative cooling (Bio-RC) film consists of periodically aligned PDMS micro-pyramid arrays that are encapsulated by randomly distributed spherical ceramic particles (Fig. 15 c3, c4). Thanks to the TIR of the surface architecture and the scattering effect of these ceramic particles in the visible and NIR region, a 500-μm-thick film exhibits 0.95 solar reflectance as well as average MIR emissivity of 0.96, without the assistance of silver back-coating. As a result, this film achieved a passive temperature drop of 5.1 ºC with radiative cooling power of ~ 90.8 W m^{-2} under direct sunlight. The authors also demonstrated the applications of the film in electronic and motorized devices. As depicted in Fig. 16 c5, c6, when a piece of paper and the Bio-RC film were placed on to the surface of a car hood and exposed to the sunlight, the Bio-RC film reduced the average hood temperature by 3.8 ºC, whereas the white paper cooled the car hood by an average temperature of only 0.6 ºC. Such a cooling effect shows that the Bio-RC films are promising in various systems by virtue of their excellent interdisciplinary applicability. Similarly, Liu et al. fabricated a biomimetic photonic composite film featuring inner pores and single-directional aligned microhump-shape textures, by the microimprint and phase separation approach [60]. The composites exhibited a high solar reflectivity of 0.976 owing to the effective Mie scattering by micropores in the solar spectrum, and a high emissivity of 0.955 in the atmospheric window because of the antireflection of microhumps and phonon polarization resonances in the MIR range. Based on this composite film, radiative cooling performance with maximum temperature reduction of 6.6 ºC and cooling power of 78 W m^{-2} was demonstrated. This composite is also able to be processed into other forms including slabs, bulks as well as complicated architectures by the DIW technique, offering a feasible strategy for manufacturing radiative cooling materials with multiple sizes and forms. Unlike those radiative cooling materials with peak-shaped surface textures, Wang et al. demonstrated that the surface micropores and nanopores in polymer film also play essential roles for enhancing the solar reflectance and LWIR emissivity [370]. They fabricated a hierarchically porous array PMMA (PMMA$_{HPA}$) film with periodic aligned micropores array on the surface and abundant randomly distributed nanopores inside, by using a unidirectional rubbing assembly method (Fig. 16 d1-d4). The periodic ordered micropores (~ 4.6 μm) are able to scatter the solar irradiation, and the abundant nanopores further enhance the scattering of shorter visible wavelengths. Besides, the PMMA$_{HPA}$ film has its intrinsically high extinction coefficient in the LWIR range, resulting in high emissivity of atmospheric window. Combining these ideal features, the PMMA$_{HPA}$ film demonstrates high solar reflectance of 0.95 and LWIR emittance of 0.98 (Fig. 16 d5), along with subambient cooling performances of ~ 8.2 ºC during the night and ~ 8.9 ºC at noon (Fig. 16 c6). Moreover, after superhydrophobic modification by fluorosilane, the film still features high solar reflectance as well as LWIR emissivity, and can be adopted in various atmospheric humidity situations. For instance, a promising subambient temperature of ~ 5.5 ºC is achieved by this superhydrophobic porous PMMA film, under hot (solar irradiation of ~ 930 W m^{-2}) and moist (relative humidity of ~ 64%) subtropical marine monsoon climate. The study has provided a deeper insight into the easy fabrication of all-day and all-climate radiative cooling system.

Apart from aligned pore or surface texture structures, cellulose nanofibers were also found to be an effective base material in engineering the backscattering of solar radiation and emitting of MIR radiation. Li et al. developed a passive radiative cooling wood material by engineering the spectral responses of natural wood. [371] After delignified with boiling H_2O_2, the obtained cooling wood is composed of cellulose nanofibers partially aligned in the growth direction of the tree. The mesoporous cellulose structure results in effective scattering and hazy reflecting effects toward solar radiation in a hemispherical solid angle, which is beneficial for avoiding visual discomfort caused by strongly specular reflection. Meanwhile, the infrared emission of -OH association and C-H, C-O, and C-O-C stretching vibrations of the cooling wood coincidently lie in the atmospheric window, resulting in a near-unity infrared emissivity. Consequently, this cooling wood demonstrates a subambient radiative cooling temperature over 9 ºC during the night and 6 ºC during the midday. In addition, benefiting from the enlarged interaction area between exposed hydroxyl groups of the aligned cellulose nanofibers after lignin removal, the cooling wood shows robust mechanical properties with a tensile strength over 400 MPa and toughness of 3.7 MJ m^{-3}, which is 8.7 and 10.1 times that of natural wood, respectively. Therefore, the wood-based materials offer a promising strategy for largescale, energy-efficient, and sustainable fabrication of passive radiative cooling materials.

Recently, radiative cooling textiles with artificial structures for personal thermal management (PTM) have attracted increasing attentions because of the climate changing and global warming problems that have been worsening the living environment of human beings. Considering the multifunction of closing textiles including providing comfort and glamour as well as temperature maintenance to the human body, spectral response requirements for radiative cooling textiles are different with above-mentioned general radiative cooling materials. From the aspect of body thermal radiation, under normal skin temperature of 34 ºC, the human skin features high IR emissivity of 0.98, and emits thermal radiation with wavelength ranging from 7 to 14 μm, accounting for over 50% of the total body heat dissipation under indoor scenario. [1] In indoor environment, IR transparent textiles have been demonstrated to be efficient in transmitting the body radiative heat to realize passive cooling. [372] However, requirements for personal radiative cooling textiles in outdoor environment are rather stringent, because of the addition of external solar irradiation (~1000 W m^{-2}) and raised body heat generation (~100 W m^{-2}). Thus, textiles with selective transmittance and/or emittance in the solar spectrum and IR transparency window are needed for realizing multi-scenarios. From the aspect of wearing comfort, excellent air/moisture permeability, anti-electrification as well as touch comfort are essential properties for a passive radiative cooling textile. For this reason, those non-woven radiative cooling films are unsuitable for PTM, although they demonstrate good passive cooling performance. [58].

According to above designing guidelines, researchers have developed various types of passive radiative cooling textiles, most of which are composed of one-directional aligned nano/micro-fibers that first produced by gel-spinning or melt-spinning technique and then knitted

into interconnected lamellar structure. Cai et al. demonstrated the first spectrally selective nanocomposite textile for outdoor passive radiative cooling by combining the intrinsic material property of PE and structural photonic engineering of ZnO nanoparticles and pores (Fig. 17a). [373] PE is found to be IR transparent due to its intrinsically simple chemical bonds of C-C and C-H, and thus is beneficial to transmit human body radiation outward. To achieve a high solar reflectance, massive ZnO nanoparticles and air pores were introduced as Mie scattering centers. Thus, the ZnO-PE shows high solar reflectance over 90% and transmissivity of ~80% within the human body radiation range. Under direct sunlight irradiation, the ZnO-PE could reduce the surface temperature of simulated skin by 10 °C, and the temperature reduction is still over 8 °C even under sweat evaporation condition. This report has opened up a new way for fabricating composite fibric textiles with promising passive human body cooling properties. Following this strategy, Wang et al. demonstrated that a hybrid membrane radiator, consisting of PVDF/tetraethyl orthosilicate (TEOS) nanoporous fibers and randomly surface-distributed SiO_2 microspheres, also features high IR emissivity over 0.96 and solar reflectivity of 0.97. [374] Consequently, the radiator realized an average radiative cooling power of 61 W m^{-2} along with a temperature reduction up to 6 under peak solar irradiation of 1000 W m^{-2}. Zeng et al. designed a multilayer metafabric consisting of a TiO_2-PLA composite-woven textile laminated with a thin polytetrafluoroethylene (PTFE) layer (Fig. 17b). [375] By choosing the optimized nanoparticles with diameter ranging from 200 to 1000 nm and nanofibers with length of microns and a width less than 200 nm, the composite exhibits a broadband reflectivity of 92.4% within the solar irradiation range (0.3–2.5 μm). In the meantime, the PLA fibers provide rich emittance of 94.5% across the atmospheric transparent window due to their abundant -CH_3, -CH, C-O and C═O bonds. Owing to these features, the metafabric vest achieved a temperature reduction of ~ 4.8 °C when wore by a volunteer, comparing with tradition cotton vest. More impressively, when covered by this metafabric, the car model showed a surface temperature reduction of ~ 27 °C than that covered by a commercial vehicle cover. These results indicate the potential commercial applications in multiple complex scenarios of the textiles. Recently, Zhu et al. developed nanoprocessed silk fabrics for subambient daytime radiative cooling (Fig. 17c). To remedy the low reflectivity limitation of natural silk in the UV range (300–420 nm), they modified the natural silk fabrics by attaching Al_2O_3 nanoparticles onto their surfaces through the scalable coupling agent-assisted dip-coating method. [376] Owing to the minimum absorption and strong scattering properties of Al_2O_3 toward UV light, the nanoprocessed silks demonstrate 95% reflectivity in the solar irradiation range and high emissivity of ~ 0.9 in the 8–13 μm range. Under direct solar irradiance of 900 W m^{-2}, a subambient temperature of ~ 3.5 °C was achieved by the stand-alone nanoprocessed silks. Moreover, when covered with the nanoprocessed silk, the surface temperature of a simulated skin achieved a reduction of ~ 8 °C under sunlight. Plus, this cooling silk shares similar comfort and wearability with natural silk. Judging from current trend, more convenient, scalable, and sustainable fabrication techniques of cooling textiles for human body passive cooling are coming soon.

Human body passive cooling textiles are also getting smarter. As a proof of concept, Zhang et al. proposed an IR gating textile which can dynamically engineering its emissivity according to the surrounding environment of human body. [59] The textile is woven by numerous individual yarn which is composed of multiple single-directional aligned metafibers containing IR-active nanostructures. Under hot and wet condition, the yarn collapses into a tight bundle, resulting in an IR emissivity shift towards human body radiation and consequently an enhanced radiative cooling of the human body. While under cold and dry condition, opposite effect occurs and thus the radiative cooling of human body is suppressed. This pioneer research opens a pathway for designing self-adaptive passive radiative cooling clothes that may expand our ability of environmental adaptation.

6. Alignment engineering for thermal absorption

Different from those thermal radiation applications that dedicate to reject solar thermal energy, light-to-heat-conversion applications such as solar vapor generation (SVG), [377] solar energy storage, [378] photothermal therapy, [379] and photothermal actuators, [380] etc., regard the solar irradiation as priceless treasure due to its abundant and eco-friendly characteristics that superior to any other energies. In these applications, the solar absorber is the key component (or the sole component in partial SVG) for converting solar energy into thermal energy. To achieve high solar-thermal conversion efficiency, the absorbers should possess maximized absorbance within the solar irradiation wavelength range, while minimized heat dissipation to the surroundings for realizing local heating. Besides, an omnidirectional solar absorption regardless of incident light angle is also required from the aspect of various application scenarios. The past few decades have witnessed the rise of advanced solar absorbers designed for efficient solar-thermal conversion, especially through nanostructure design. We have noticed that different alignment techniques and aligned nanostructures are utilized in the rational design of solar absorbers. These unique structures, together with useful photothermal agents, have enabled materials that can effectively convert solar energy into heat. Therefore, in this Section, we summarize the alignment engineering of photothermal nanomaterials regarding the rational design of solar absorbers, based on some popular solar-thermal conversion applications.

Vertically aligned solar absorbers. Carbonaceous materials including amorphous carbon, graphene, and carbon nanotubes/nanofibers, are intrinsically absorbable toward broadband light due to their continuous energy levels, which are originated from the exist of hybrid bonds. [381] However, their absorptivity is limited to 0.8–0.85 due to the reflection at the air-dielectric interface [382]. Thus, numerous efforts have been paid to reduce the reflective energy loss, where an effect strategy is to increase the optical path length of incident irradiation within the materials. Through the nanostructure design, the refraction and scattering of incident light can be enhanced, especially when the dimension of the nanostructures is close to the incident light wavelength. For the first time, Yang et al. experimentally demonstrated that vertically aligned carbon nanotube arrays have an emissivity of 0.99 in the range of 457–633 nm. [382] Subsequently, Mizuno et al. reported a water-assisted CVD-grown vertically aligned SWCNTs forest (Fig. 18 a1, a2), featuring a near-unity emissivity of 0.98–0.99 within wavelength band of 200 nm to 200 μm. [383] There are two underlying mechanisms leading to this ultra-black material. One is that the homogenous sparseness distribution of SWCNTs decrease the electron density and permissivity, thus resulting in decreased refractive index and a drop of reflectance, according to Fresnel's law. The other is that the aligned structure increases the interaction between incident light and SWCNTs (Fig. 18 a3), thereby reducing the reflectance. Over a wide incident angle range of 11–70° and with a spectral range of 2–10 μm, the reflectance of the forest remains less than 2% (Fig. 18 a4), indicating its superiority in solar-thermal harvesting. One should be noted that, to achieve a sufficient absorption, the thickness of CNT forest should be finely tuned. According to Shi et al., when the thickness of CNT forest is 6.5 μm, the transmission is considerably large due to the insufficient absorption. After increasing the thickness to 70 μm, the forest demonstrates nearly undetectable reflection and transmission spectra. [384] Featuring this promising light trapping ability, the vertically aligned CNT array has been utilized in SVG by Yin et al. [385] By placing a layer of vertically aligned CNT array onto the surface of sea water, 99% solar energy in the range of 280–820 nm can be absorbed and converted into heat, resulting in a localized temperature rise at the top of water. Assisted by the array, the evaporation rate of water is 10 folds of that of bare water, and the solar-thermal conversion efficiency reaches 90%, under solar illumination of 15 kW m^{-2} (15-sun). This is the highest reported evaporation ratio enhancement at that time, which is ascribed to the synthetic effects by the strong optical absorption of vertically

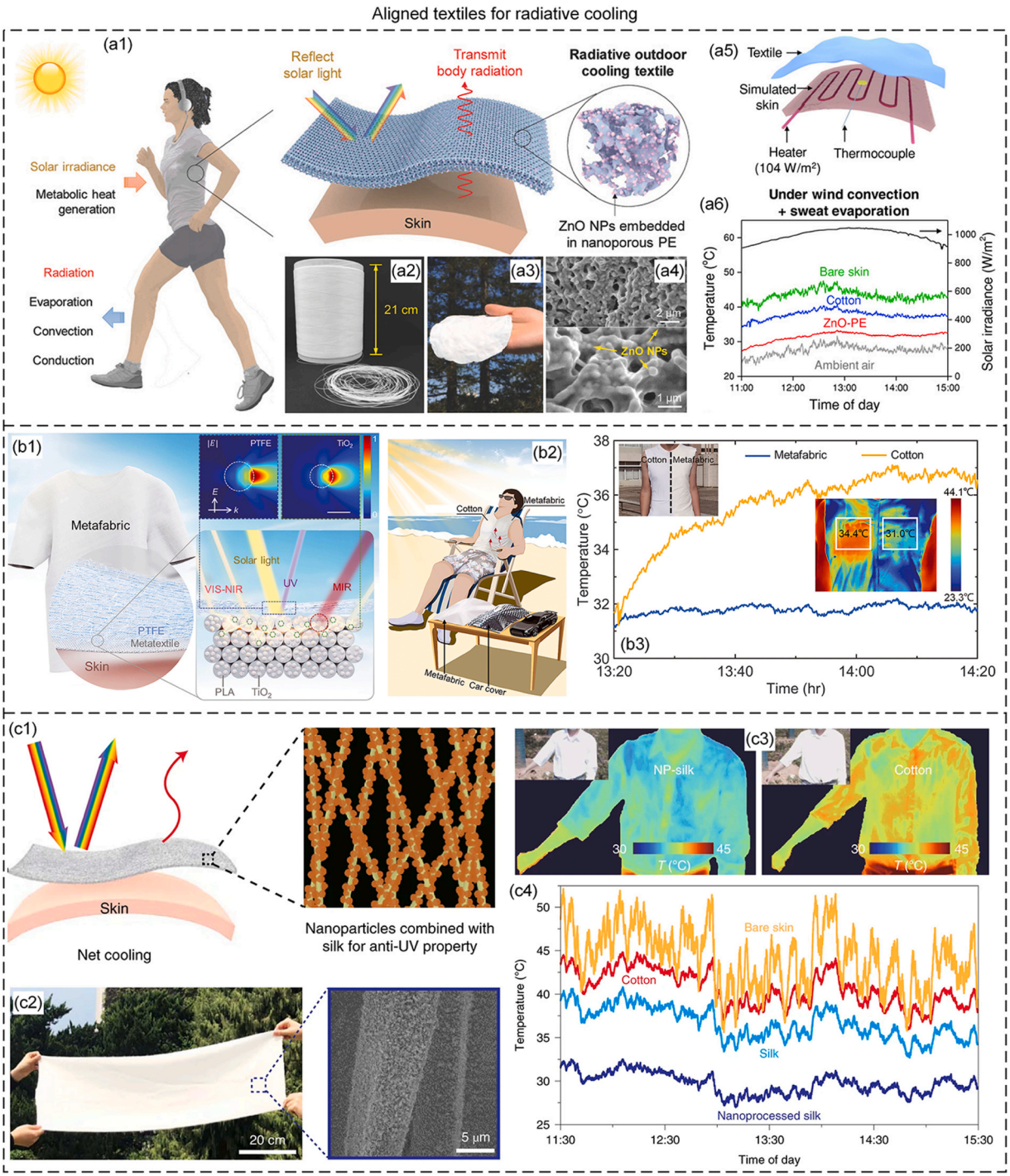

Fig. 17. Aligned textiles for radiative cooling. a) Nanocomposite textile for personal radiative cooling by combining PE and structural photonic engineering of ZnO nanoparticles. a1) Schematics showing the heat input and output pathways of human body under sunlight, and the radiative cooling mechanisms of the ZnO nanoparticle-embedded nanoporous PE textile. a2), a3) Photographs of a roll of ZnO-PE fibers and the ZnO-PE textile, respectively. a4) SEM images showing the cross-section of the ZnO-PE film and the morphology of individual ZnO particles. a5) Schematic of the thermal measurement setup consists of a heater simulating the skin, a thermocouple measuring skin temperature, and a textile sample covering the simulated skin. a6) Temperature variation of the ZnO-PE covered skin, cotton-covered skin, and bare skin under wind convection and sweat evaporation. b) Metafabric for daytime radiative cooling consisting of TiO_2-PLA composite-woven textile laminated with thin PTFE layer. b1) Schematic showing the structure of the metafabric. The blue, green, and red dashed boxes indicate the three-level hierarchical structure responding to the UV, VIS-NIR, and MIR bands, respectively. b2) Schematic of the metafabric cooling tests on the human body and model cars. b3) Temperature variation for human skin under different fabrics in direct sunlight in Guangzhou, China (23°5′32′ N, 113°23′45′ E). Insets show photographs and thermal images of a volunteer wearing a homemade vest. c) Al_2O_3 doped nanoprocessed silk fabric for subambient daytime cooling. c1) Schematic of the net cooling mechanism of nanoprocessed silk by enhancing UV reflectance. c2) Photograph and SEM images of an individual nanoprocessed silk yarn with Al_2O_3 particles bonded. c3) Temperature variation of bare skin and simulated skin covered with cotton, silk or nanoprocessed silk over a duration of 4 h under sunlight in Stanford, California. c4) Infrared images and photographs (insets) of a volunteer wearing shirts made from nanoprocessed silk fabric and cotton under sunlight in Nanjing, China.

Reproduced with permission [373]. Copyright 2018, Wiley-VCH. (b) Reproduced with permission [375]. Copyright 2021, American Association for the Advancement of Science. (c) Reproduced with permission [376]. Copyright Nature Publishing Group.

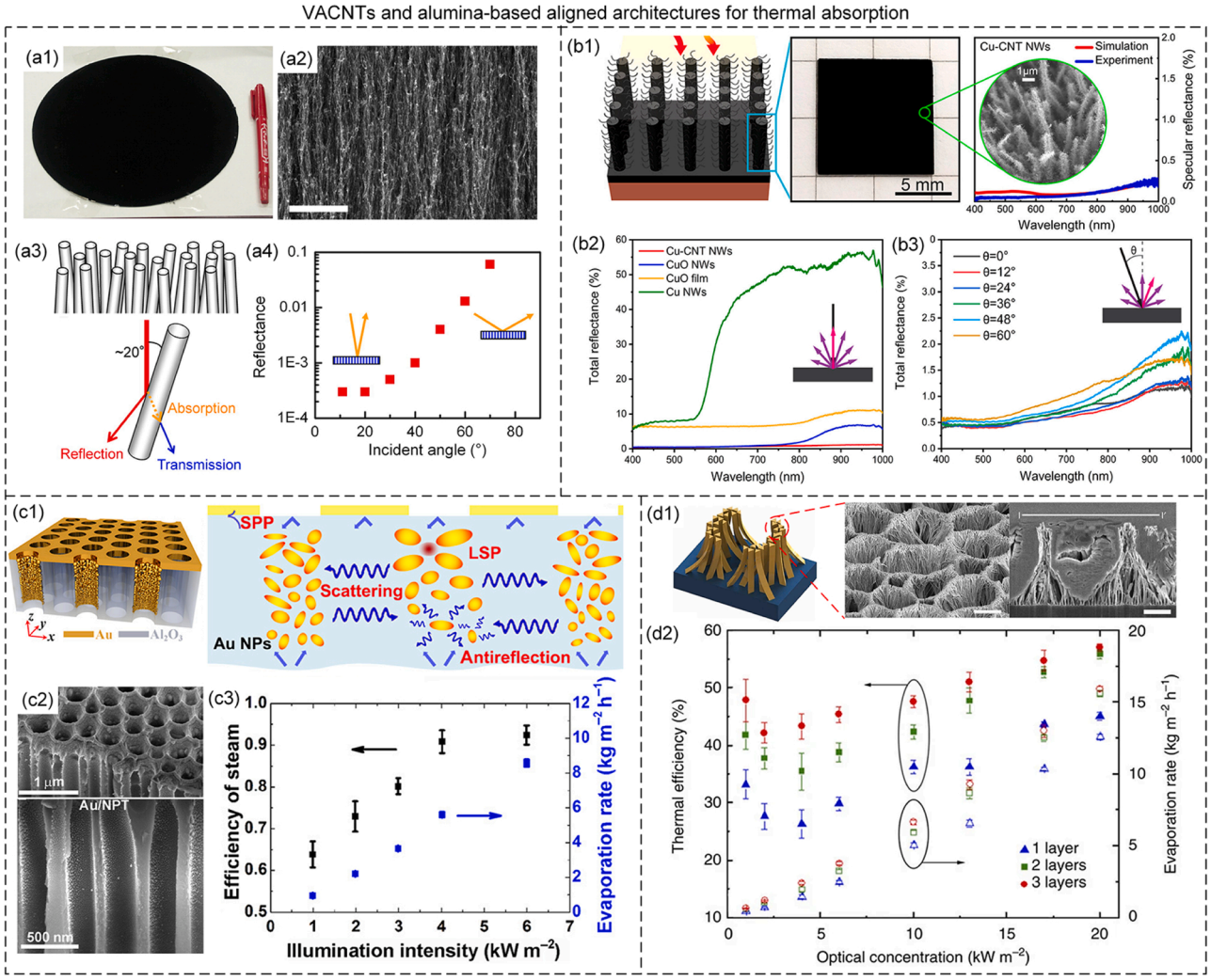

Fig. 18. CNTs- and alumina-based aligned architectures for thermal absorption. a) Vertically aligned SWCNTs forest. a1) Photograph and a2) SEM image of the forest standing on a silicon substrate. a3) Schematic illustrating the interaction between incident light and the vertically aligned SWCNTs array. a4) Specular reflectance of the SWCNTs forest as a function of incident angle. b) Cactus-like structure by combining Cu with vertically aligned CNTs. b1) Schematic, photograph, and specular reflectance curves of the Cu-CNTs nanowires. Inset shows the SEM image of the nanowires. b2) Total reflectance spectra of the CuO nanowires, CuO thin film, Cu nanowires, and Cu-CNTs nanowires at normal incidence. b3) Angle-resolved total reflectance spectra of the Cu-CNTs nanowires. c) Au-decorated vertically aligned porous alumina as a plasmonic absorber. c1) Schematic showing the structure and absorbing mechanism of the self-assembled plasmonic absorber. c2) SEM images of the gold-deposited nanoporous absorber. c3) Solar steam efficiency and evaporation rate with plasmonic absorber as a function of illumination intensity. d) Black gold membrane composited of Au-coated aligned alumina nanowires. d1) Schematic illustrating the structure and absorbing mechanism of the black gold membrane. d2) Solar steam efficiency and evaporation rate of vapor generation process generated by one, two or three layers of black gold membrane at different optical power density.

(a) Reproduced with permission [385]. Copyright 2017, American Chemical Society. (b) Reproduced with permission [391]. Copyright 2020, American Chemical Society. (c) Reproduced with permission [74]. Copyright 2016, American Association for the Advancement of Science. (d) Reproduced with permission [73]. Copyright 2015, Nature Publishing Group.

aligned CNT array, the localized heating at the water surface, and the fast water transport through the frictionless wall of CNTs. Although these vertically aligned nanostructures demonstrate superb wide-band absorptivity, their birefringent characteristic makes them angle- and polarization-sensitive, which hinders their practical application in capturing the solar energy whose incident angle is variable [383,386].

Hierarchically aligned solar absorbers. To remedy the angular sensitivity of vertically aligned nanostructures and achieve omnidirectional solar absorbers, researches have proposed hierarchically aligned nanostructures that combine materials of different scales, classes, and optical properties. The hierarchically aligned solar absorber contains holistically aligned structures and locally random-distributed elements that aim at increasing the light-matter interaction length, leading to increased multiple internal reflection within a wide wavelength range and thus reduced angle sensitivity. Previous works have reported hierarchical structures including vertically aligned CuO/graphdiyne nanowire arrays on 3D Cu foam, [387] carbon black nanoparticles on knife-like Al_2O_3 nanoplates, [388] graphene nanosheet arrays on 3D graphene foam, [389] and MWCNTs on Al_2O_3 nanostructured networks, [390] that exhibit improved solar incident angle independence up to

50°, within a broad wavelength band. To further enhance the omnidirectional absorptivity, more works were conducted. Kiani et al. reported a cactus-like hierarchical structure by combining the light-trapping abilities of Cu nanowires with the vertically aligned CNTs. [391] This hybrid structure exhibits synergistic properties where the microscale Cu nanowires structure creates a smoothly gradient refractive index that reduces specular reflections, and the nanoscale CNTs structure limits the diffuse reflections caused by the scattering of individual nanowires (Fig. 18 b1). As a result, the cactus-like structure features average specular reflection of < 0.1% and average total reflection of < 1% up to a 60° incident angle within 400–1000 nm (Fig. 18 b2, b3).

Hierarchically columnar structures containing vertically aligned

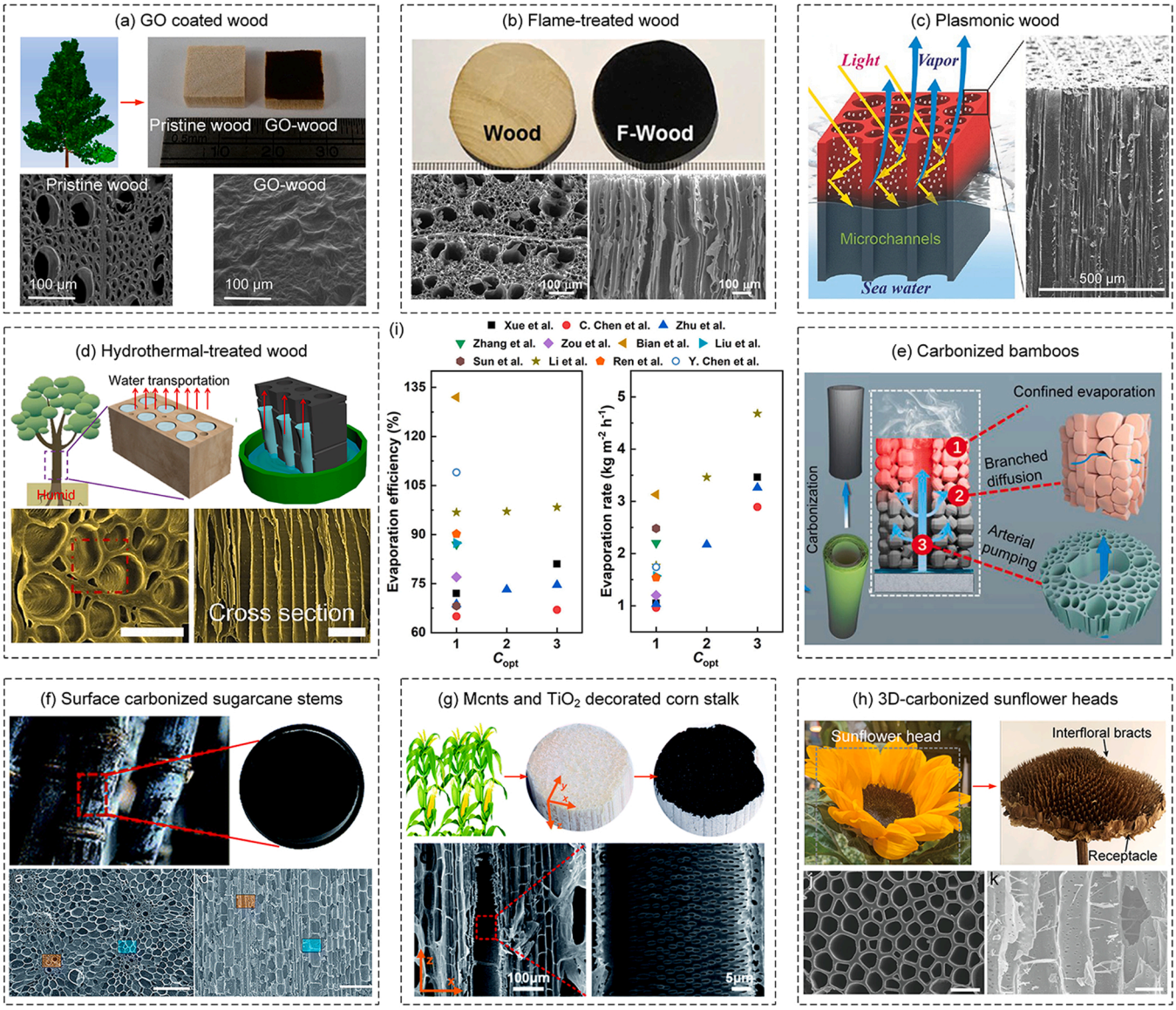

Fig. 19. Biomass-based aligned architectures for thermal absorption. a) Photographs and cross-sectional SEM images of the pristine wood and GO coated wood (GO-wood). b) Photographs of the pristine wood and flame-treated wood (F-wood), and SEM images of the F-wood in top and cross-sectional views. c) Schematic illustration and SEM image of the plasmonic wood. d) Schematic showing the solar steam generation within the hydrothermal-treated wood, and the top-down and cross-sectional SEM images of this wood. Scale bar, 50 μm. e) Schematic showing the microstructure and operating principle of the carbonized bamboos-based 3D solar absorber. Numerous aligned microchannels, such as the parenchyma cells and vascular bundles, act as highways for rapid water transport. f) Surface carbonized de-sugaring sugarcane stems as efficient solar steam generators. The obtained materials have abundant close chambers for thermal insulation and bundles of vertical channels for water transport. g) Multi-walled CNTs and TiO_2 decorated corn stalk as solar steam evaporator. The natural structural features of stem marrow of corn stalks, including scattered vascular bundles with super-hydrophilic properties enable high-speed water transportation, and the porous basic tissues with layer-by-layer biofiltration, porous cavities realize multi-stage filtration, transportation, and storage of seawater. h) Polypyrrole-decorated 3D array structural sunflower discs (PPy-SFD) as solar evaporator. The SFD can absorb a majority of incident light due to the light reflection from each natural 3D array structural unit, and a pyrrole polymerization treatment further improve its photothermal performance. i) Solar thermal conversion efficiency and solar vapor evaporation rate data of representative biomass-based solar absorbers.

(a) Reproduced with permission [393]. Copyright 2017, American Chemical Society. (b) Reproduced with permission [403]. Copyright 2017, American Chemical Society. (c) Reproduced with permission [72]. Copyright 2018, Wiley-VCH. (d) Reproduced with permission [396]. Copyright 2020, Elsevier. (e) Reproduced with permission. [398] Copyright 2019, Wiley-VCH. (f) Reproduced with permission [399]. Copyright 2019, The Royal Society of Chemistry. (g) Reproduced with permission [400]. Copyright 2020, The Royal Society of Chemistry. (h) Reproduced with permission [403]. Copyright 2020, American Chemical Society. (i) Data acquired from: Xue et al. [394] C. Chen et al. [395], Zhu et al. [72], Zhang et al. [396], Zou et al. [397], Bian et al. [398], Liu et al. [399], Sun et al. [400], Li et al. [401], Ren et al. [402], and Y. Chen et al. [403].

micropores and secondary nanostructures are also effective for achieving light-trapping effect. Zhou et al. reported on a plasmonic absorber which is fabricated by self-assembly of gold nanoparticles onto a vertical-aligned porous alumina template by a physical vapor deposition (PVD) process. [74] Gold nanoparticles with random sizes and distributions help to absorb light in a broad wavelength range by the high density of hybridized localized surface plasmon resonance (LSPR). The aligned porous template provides strong scattering and internal reflection that enable the extension of optical path lengths, and its large porosity results in strong antireflective properties due to the relatively low effective refractive index which further promotes the absorption efficiency (Fig. 18 c1, c2). Therefore, this structure achieved an average light absorptivity of ~ 99% across the visible to MIR regimes (400 nm to 10 μm), and over 90% solar-thermal conversion efficiency under 4-sun intensity (Fig. 18 c3). Interestingly, Bae et al. provide another fabrication strategy of hierarchically plasmonic solar absorber. [73] They obtained the vertically aligned AAO nanowire bundles by controlled wet etching of AAO templates, then the bundles were chemically etched to enlarge their nanoholes, followed by a self-aggregation process of the bundles. Finally, a 40-nm-thickness gold film was sputtered onto the nanowire surface to obtain the black gold membrane (Fig. 18 d1). The obtained hybrid bundles exhibit multiscale structure which contains a wide range of metallic nanoscale gaps and microscale funnel structures, resulting in a broadband absorption of 91% in the wavelength from 400 to 2500 nm and solar-thermal conversion efficiency of 57% under 20-sun illumination (Fig. 18 d2). As a more facile and low-cost fabrication strategy based on AAO template, Li et al. proposed a metal-free solar absorber by spraying carbon black nanoparticles onto 5-μm-thick AAO template with a nanoporous silicon films beneath. [392] The synergetic effect of light scattering by silicone nanoparticles, multiple internal reflections by porous AAO template, and absorption enhancement by gradient-refractive nanoporous silicon results in an average absorbance of 97.5% within the wavelength range of 2.5–15.3 μm. Although the absorber does not cover the solar spectrum, it may provide useful train of thought for the facile fabrication of solar absorbers.

Natural wood, with its vertically-aligned hierarchical and mesoporous structure, has attracted much research interest in thermophysics area, including the previously mentioned thermal insulation and radiative cooling applications. Undoubtably, these unique structures enable their potential application to solar absorber. Based on that, Liu et al. proposed a bilayer solar absorber by depositing a GO layer onto the pristine wood to achieve an enhanced solar absorption (Fig. 19a). Besides, the inherently low thermal conductivity and naturally aligned microchannels of wood favor the local heating and water transportation, respectively. Thus, the resulted wood-GO composites exhibit a solar thermal efficiency of ~83% under 12-sun illumination, which is 60% higher than that of pristine wood [393]. Nearly the same time, Zhou's group demonstrated that wood can be an ideal absorber after a simple flame treatment (Fig. 19b). [394] By directly burning the natural basswood on the flame of an alcohol lamp for few minutes, the surface of the wood is carbonized, and carbon nanoparticles are also deposited on the wood due to the incomplete combustion of alcohol. Thus, the flame-treated wood (F-wood) exhibits high absorptivity of ~99% toward standard air mass 1.5 global (AM 1.5 G) solar spectrum. The extraordinary characteristics including solar absorption, heat localization and water transport as well as rapid evaporation make the F-wood an excellent solar absorber, achieving a high solar-thermal conversion efficiency of ~81% under 3-sun illumination. Hu's group coated CNTs onto the natural wood and then obtained the wood/CNTs absorber. [395] The surface-coated CNTs, together with the rough hair-like wood surface created by electric saw significantly enhance the solar absorption as well as photothermal conversion efficiency. Meanwhile, chemical treatments toward natural Balsa wood create larger channels by connecting the vertically aligned lumens inside the wood, which facilitate the water transport. Owing to the systematic optimization of solar absorption, thermal conversion, and water transportation, this wood/CNTs membrane exhibits an absorption of ~98% within 300–1200 nm, and a photothermal conversion efficiency of 81% under 10-sun irradiation. Later on, they also reported a plasmonic wood by decorating metal (Pd, Au, or Ag) nanoparticles into the 3D microchannels of natural basswood. [72] Owing to the plasmonic effect of the metal nanoparticles and the waveguide effect of numerous aligned microchannels in the wood, this plasmonic wood demonstrated a high solar absorption of ~99% within the wavelength range from 200 to 2500 nm. Impressively, a high absorbance over 98% can be maintained under various incident angles from 0 ° to 60°, which may be attributed to the repeated light coupling within the plasmonic microstructures and elongated microchannels. Consequently, the plasmonic wood achieved a high solar-thermal conversion efficiency of 85% under 10-sun illumination and a promising cycling stability of 144 h without evident performance degradation. These pioneer works paved the way of wood-based solar absorbers. Since then, solar absorbers based on various biomass with aligned microchannels, including not only wood, [396,397] but also bamboos, [398] sugarcane stem, [399] corn stalk, [400,401] loofah sponge, [402] sunflower, [403,404] etc., have emerged, and their microstructures are displayed in Fig. 19c-h. Fig. 19i concludes the key performance data of these representative works. One should be noted that, considering the practicability of SVG architectures, only the properties under 1–3 sun illumination are gathered.

In addition to natural hierarchical materials, artificial lamellar materials provide a new approach to control the solar absorption process, by creating vertically or horizontally aligned nanostructures, based on solar absorption media. For instance, Zhang et al. reported a long-range vertically aligned graphene sheets membrane fabricated by an antifreeze-assisted freeze casting technique [168] Ethanol is properly added into the GO suspension to tuning the ice growth kinetics while freezing, thus resulting in a 3D graphene membrane with vertically aligned graphene sheets. These vertically open channels provide efficient pathways for water transport and vapor release. Meanwhile, the membrane exhibits absorption of 93%, 98% and nearly 100% in the UV, visible and NIR wavelength range, respectively. The absorption of the membrane is much higher than that of randomly freeze-dried GO film, which is mainly attributed to the aligned nanostructures that prolong the optical path length. Consequently, the membrane achieved excellent solar conversion efficiency of 86.5% under 1-sun and 94.2% under 4-sun irradiation, respectively. This is an efficient yet cost-effective strategy which is easy to be scaled up for regeneration of clean water. Horizontally aligned multilayer film is also able to create excellent light-trapping structures, as demonstrated by Lin et al. [405] They fabricated the multilayer polypyrrole (PPy) nanosheets with spontaneously formed surface wrinkles and ridges textures by a self-assembly approach. First of all, the base material PPy, as a representative photothermal conjugated polymer, features a broadband absorption spectrum originating from its π-conjugated backbones of sp^2-hybridized carbon [377]. Further, the sequential polymerization strategy of PPy on an air-laid paper substrate enable the formation of randomly distributed light-trapping schemes that substantially reduce the reflection and transmittance across a wide spectral and angular range. Hence, the as-fabricated 10-layer PPy nanosheets demonstrated over 99% absorbance toward solar energy and a maximum solar-thermal conversion efficiency up to 95.33% under 1-sun illumination. This polymerization-induced light confinement strategy has given some enlightenments to other polymers-based solar absorbers, such as polydopamine (PDA) and polyacrylonitrile (PAN) [406,407].

During a practical SVG process, the salinity on the surface of evaporator will increase with the water evaporation, and thus cause significant salt crystallization on the evaporator. The accumulation of salt crystals will reduce the solar energy absorption and resist the water transport channels, resulting in deterioration of solar-thermal conversion performance. Therefore, it is necessary to consider the prevention of salt-fouling problem when designing the solar absorbers. Typically, surface hydrophobization is adopted to solve the salt crystallization

issue. For example, the PPy coated stainless steel mesh with hydrophobicity self-clearing capability exhibits good stability and durability [408]. However, a hydrophobic surface may limit the efficient heat transfer from the solar absorber to the liquid due to their insufficient contact, and thus reduce the evaporation rate. Alternatively, we found two alignment strategies for dealing with this issue. One is to promote the salt transportation from the evaporation surface to the bulk water [409,410]. For example, the CNTs@SiO_2 nanofibrous aerogels composed of vertically aligned vessels and porous vessel walls, which provide shortest channels for salt to transport from the evaporation surface to the bulk water, under the driving force of salinity difference [409]. With this cellular architecture, the aerogels exhibit nearly no salt crystals accumulation on the evaporation surface even in 20% brine and under 6-sun illumination, as well as a high light absorbance of ~98% across a broad spectrum from 200 to 2500 nm. The other is to reject the salt ions from permeating the solar absorber. For instance, Ying et al. reported a double-layered nanocomposite membrane, which composed of a top sublayer based on laminated-aligned MXene nanostructures and a bottom sublayer based on horizontally aligned rGO nanosheets [411]. The top sublayer is utilized to reduce light reflection and thus improve the solar-thermal efficiency, while the bottom rGO nanosheets is designed to have narrowed interlayer spacing between adjacent rGO. Thus, the water molecules could permeate the sublayer while salts with larger size could not. This selectively permeation ability of rGO nanosheets is essential to prevent salt accumulation on the evaporator. As a result, the membrane shows a solar-thermal efficiency of 85.2% at 1-sun, and the efficiency remains 81.4% after 40 cycles in seawater, which may provide new insights for designing self-cleaning solar absorbers.

7. Conclusions and outlooks

In this review, we provide a state-of-the-art account on recent developments of aligned thermal materials with an emphasis on the alignment mechanisms, architecture-function interactions, and thermal applications. We first discussed the different methods developed to fabricate materials with aligned structures for regulating thermal conduction, insulation, radiation, and absorption properties. External fields-, mechanical forces-, templates-, and 3D printing-based approaches were utilized to prepare various ordered architectures. The correlations between alignment approaches and aligned structures have enabled the formulation of the fundamental principles for thermal materials engineering. Generally, the alignment direction of microstructures in thermal materials strongly depends on the direction of driving forces. Specifically, external fields are able to realize 1D-aligned architectures, and mechanical forces excel at realizing 1D- and/or 2D-aligned microstructures. For templates-based approaches, the aligned microstructures are mainly determined by the template architecture. The light- and ink-based 3DP methods are versatile in building complicated alignment structures owing to their wider degree of manufacturing freeform over other methods.

Whereas, from the aspect of thermal functionalities, each aligned structure has its own abilities and advantages when faced with specific thermal applications. For thermal fillers in TIMs that are sandwiched between a heat source and a heat sink, 1D-aligned architecture is highly desired so as to quickly dissipate the heat from source to sink. However, for heat spreaders aiming at relieving the local heat accumulation, 2D-laminate-aligned structures featuring high thermal conductivity within the in-plane direction are preferred. For thermal insulators, aerogels with 2D-aligned planar pore structures or 3D-aligned isotropic pore structures are beneficial for blocking the potential heat transfer process. Moreover, the required architectures are more complex in thermal radiation and absorption applications, where multi-scale aligned microstructures are designed. Overall, the best alignment architecture is determined by the targeted thermal purpose, as well as in collaboration with the thermal properties of constituents.

Then, we focused on the progress in each specific thermal application with aligned thermal materials. In thermal conduction field, two hot topics regarding the alignment engineering are discussed. One is the alignment engineering of polymers, and the other is the composites. It is inspiring to see that polymer can also be made into highly thermal-conductive matrix by using reasonable alignment techniques, which is quite inconceivable before. The composite material, which is the ideal candidate of TIMs, have taken full advantage of each alignment method to reinforce the orderliness of thermal fillers within the matrix materials. Thus, efficient heat transfer pathways were established and interfacial thermal resistance is minimized. As a result, a TCE over 2400% with per 1 vol% filling load can be achieved [214]. In thermal insulation field, alignment techniques are used to construct complicated heat transfer barriers inside thermal insulators. These barriers include aligned tiny pores as well as solid walls. Aerogel films or blocks with 2D- or 3D-aligned nanostructures are the common form of thermal insulators, while synthetic hollow fibers with various aligned pore structures are also developed for personal thermal insulation. Here we highlight the graphene aerogel with closed cellular structure which features excellent thermal insulating ability, by virtue of the closed pores that inhibit gas conduction/convection in all directions, and the ultrathin walls that suppress the solid conduction [53]. In thermal radiation applications, alignment structures are constructed to realize selective surface emissivity within different wavelength ranges, which has enabled the development of radiative thermal camouflage, daytime radiative cooling as well as personal thermal management. It is interesting to find that, many fantastic alignment structures used for thermal radiation regulation are learned from natural species such as Sahara silver ants, [27] white beetles, [368] golden longicorn, [369] etc., which have already shown their masterly thermal management abilities. Besides, solar-thermal conversion applications call for efficient solar absorbers, in which vertically aligned and hierarchically aligned architectures are built to enhance the solar energy trapping effect. Both top-down and bottom-up synthesis routes can be utilized for the construction of efficient light-matter structures.

Although breakthrough has been made in the alignment engineering of thermal materials, there are still rooms worthy of further exploring. Here, we present some thinking on future directions of alignment engineering of thermal materials.

First, an efficient and direct structural design method towards desired thermal materials is still lacking. Current design approaches of thermal materials still rely on the try-and-error interactions between predefined micro/nano-structures and targeted thermal properties. High-throughput screening (HTS), which combines basic heat transfer theory with advanced optimization algorithms may be a promising solution in dealing with this issue. However, how to establish a relationship between aligned structures and desired thermal properties still remains challenging, especially for those thermal materials where thermal transport phenomena are trans-scale.

Second, high-precision alignment of multi-material components needs further exploring. Currently, a single alignment approach (except for 3DP) can usually achieve a homogeneously, macroscopically aligned structure, which are not enough to meet future requirements on intricate thermal micro-/nanostructures. Therefore, different alignment methods are expected to combine with each other or extra driving forces to acquire more precise control. Progress has been made, for example, freeze-spinning, [51] 3D magnetic printing, [100] and local-heating based stretching [227]. Whereas the pursuit of non-uniformly aligned nanostructures with two or more types of basic architecture is still under development.

Third, there is a growing interest to dynamically change thermal emissivity on demand. However, majority of aligned thermal radiation structures, including photonic crystals, composite architectures, and nanoporous films, are nonresponsive to environmental changes, thus restricting their practicalities. For instance, radiative thermal camouflaging materials are designed to achieve distinct emissivity in the atmospheric window and other wavelengths, and thus both IR stealth and

thermal equilibrium are achieved. Once background temperature is changed, this thermal equilibrium will be broken and the target will be exposed to IR detector. Therefore, dynamic controlling of surface emissivity in response to environmental variation are meaningful, yet challenging. Light-driven polymer actuators are promising candidates for dynamically tuning their emissivity without an extra energy input, [412] since pioneer work has been conducted [59].

In addition, although alignment techniques and structures have been extensively used in photothermal materials to improve solar absorption, heat localization, and vapor transportation, solar absorbers have reached their bottleneck in energy conversion efficiency, because it is challenging to fully eliminate the energy loss to surroundings during SVG. To break this bottleneck, rational design of photothermal materials and evaporators is critical. Recently developed 3D solar absorbers with interconnected nanostructures and tailored geometries such as spiral-like and heatsink-like shapes, have demonstrated extremely high solar-thermal efficiency (excesses the physical limit of planar absorbers) and water evaporation rate (up to 4.35 kg m^{-2} h^{-1} under 1-sun illumination) [413–415]. These works show us a prospective direction. One should be noted that, an ideal 3D solar absorber is not functioned by just expanding more energy input channels, but by their subtle 3D structures that facilitate better light-matter interactions, efficient water/salt transportations, and long-term sustainability [416].

Declaration of Competing Interest

The authors declare that they have no known competing financial interests or personal relationships that could have appeared to influence the work reported in this paper.

Data Availability

No data was used for the research described in the article.

Acknowledgements

This work was financially supported by the National Key R&D Program from Ministry of Science and Technology of China (2022YFA1203100), and National Natural Science Foundation of China (52106089, 52076087, 52211540005).

References

[1] J.D. Hardy, E.F. Dubois, Proc. Natl. Acad. Sci. U. S. A. 23 (1937) 624.
[2] D.G. Cahill, W.K. Ford, K.E. Goodson, G.D. Mahan, A. Majumdar, H.J. Maris, R. Merlin, S.R. Phillpot, J. Appl. Phys. 93 (2003) 793.
[3] A. Berut, A. Arakelyan, A. Petrosyan, S. Ciliberto, R. Dillenschneider, E. Lutz, Nature 483 (2012) 187.
[4] H.S. Roh, Int. J. Heat. Mass Transf. 64 (2013) 661.
[5] Y. Tian, C. Zhao, Energy 36 (2011) 5539.
[6] T. Luo, J.R. Lloyd, Adv. Funct. Mater. 22 (2012) 2495.
[7] P.J. O'Brien, S. Shenogin, J. Liu, P.K. Chow, D. Laurencin, P.H. Mutin, M. Yamaguchi, P. Keblinski, G. Ramanath, Nat. Mater. 12 (2013) 118.
[8] Y. Si, J. Yu, X. Tang, J. Ge, B. Ding, Nat. Commun. 5 (2014) 5802.
[9] G. Shen, Y. Bando, B. Liu, D. Golberg, C. Lee, Adv. Funct. Mater. 16 (2006) 410.
[10] T. Han, X. Bai, D. Gao, J.T.L. Thong, B. Li, C.-W. Qiu, Phys. Rev. Lett. 112 (2014), 054302.
[11] W. Yu, Z. Duan, G. Zhang, C. Liu, S. Fan, Nano Lett. 18 (2018) 1770.
[12] Z. Sun, R. Fan, F. Yan, T. Zhou, N. Zheng, Int. J. Heat. Mass Transf. 145 (2019), 118739.
[13] Y. Yu, L. Wang, Int. J. Heat. Mass Transf. 145 (2019), 118714.
[14] Z. Wu, C. Xu, C. Ma, Z. Liu, H.-M. Cheng, W. Ren, Adv. Mater. 31 (2019) 1900199.
[15] M. Ferraiuolo, O. Manca, Int. J. Therm. Sci. 53 (2012) 56.
[16] T. Ji, R. Zhang, B. Sunden, G. Xie, Appl. Therm. Eng. 70 (2014) 957.
[17] H. Lin, B.C.P. Sturmberg, K.-T. Lin, Y. Yang, X. Zheng, T.K. Chong, C.M. de Sterke, B. Jia, Nat. Photonics 13 (2019) 270.
[18] Q. Liao, P. Zhang, H. Yao, H. Cheng, C. Li, L. Qu, Adv. Sci. 7 (2020) 1903125.
[19] K.-T. Lin, H. Lin, T. Yang, B. Jia, Nat. Commun. 11 (2020) 1389.
[20] K. Tang, X. Wang, K. Dong, Y. Li, J. Li, B. Sun, X. Zhang, C. Dames, C.-W. Qiu, J. Yao, J. Wu, Adv. Mater. 32 (2020) 1907071.
[21] R. Hu, S. Zhou, Y. Li, D.-Y. Lei, X. Luo, C.-W. Qiu, Adv. Mater. 30 (2018) 1707237.
[22] Y. Zhai, Y. Ma, S.N. David, D. Zhao, R. Lou, G. Tan, R. Yang, X. Yin, Science 355 (2017) 1062.
[23] Y. Peng, J. Chen, A.Y. Song, P.B. Catrysse, P.-C. Hsu, L. Cai, B. Liu, Y. Zhu, G. Zhou, D.S. Wu, Nat. Sustain. 1 (2018) 105.
[24] X. Huang, G. Liu, X. Wang, Adv. Mater. 24 (2012) 1482.
[25] C. Dawson, J.F.V. Vincent, G. Jeronimidis, G. Rice, P. Forshaw, J. Theor. Biol. 199 (1999) 291.
[26] T. Stegmaier, M. Linke, H. Planck, Philos. Trans. R. Soc. A 367 (2009) 1749.
[27] N.N. Shi, C.C. Tsai, F. Camino, G.D. Bernard, N. Yu, R. Wehner, Science 349 (2015) 298.
[28] Z. Lin, Y. Liu, S. Raghavan, K.-S. Moon, S.K. Sitaraman, C.-P. Wong, ACS Appl. Mater. Interfaces 5 (2013) 7633.
[29] S. Xu, S. Wang, Z. Chen, Y. Sun, Z. Gao, H. Zhang, J. Zhang, Adv. Funct. Mater. 30 (2020) 2003302.
[30] C. Yu, J. Zhang, Z. Li, W. Tian, L. Wang, J. Luo, Q. Li, X. Fan, Y. Yao, Compos. Part A 98 (2017) 25.
[31] O.H. Kwon, T. Ha, D.-G. Kim, B.G. Kim, Y.S. Kim, T.J. Shin, W.-G. Koh, H.S. Lim, Y. Yoo, ACS Appl. Mater. Interfaces 10 (2018) 34625.
[32] Z. Tian, Y. Zhao, S. Wang, G. Zhou, N. Zhou, C.-P. Wong, J. Mater. Chem. A 8 (2020) 1724.
[33] J. Garemark, X. Yang, X. Sheng, O. Cheung, L. Sun, L.A. Berglund, Y. Li, ACS Nano 14 (2020) 7111.
[34] Z. Hu, S. Yan, X. Li, R. You, Q. Zhang, D.L. Kaplan, ACS Nano 15 (2021) 8171.
[35] X. Hu, W. Xu, L. Zhou, Y. Tan, Y. Wang, S. Zhu, J. Zhu, Adv. Mater. 29 (2017) 1604031.
[36] Y. Yang, Z. Chen, X. Song, Z. Zhang, J. Zhang, K.K. Shung, Q. Zhou, Y. Chen, Adv. Mater. 29 (2017) 1605750.
[37] A. Gurijala, R. Zando, J.L. Faust, J.R. Barber, L. Zhang, R.M. Erb, Matter 2 (2020) 1015.
[38] J. Jing, Y. Chen, S. Shi, L. Yang, P. Lambin, Chem. Eng. J. 402 (2020), 126218.
[39] L.M. Guiney, N.D. Mansukhani, A.E. Jakus, S.G. Wallace, R.N. Shah, M. C. Hersam, Nano Lett. 18 (2018) 3488.
[40] M.G. Cooper, B.B. Mikic, Int. J. Heat. Mass Transf. 12 (1969) 279.
[41] R. Prasher, Proc. IEEE 94 (2006) 1571.
[42] A. Yu, P. Ramesh, M.E. Itkis, E. Bekyarova, R.C. Haddon, J. Phys. Chem. C 111 (2007) 7565.
[43] Z. Wang, J.A. Carter, A. Lagutchev, Y.K. Koh, N.H. Seong, D.G. Cahill, D.D. Dlott, Science 317 (2007) 787.
[44] V. Singh, T.L. Bougher, A. Weathers, Y. Cai, K. Bi, M.T. Pettes, S.A. McMenamin, W. Lv, D.P. Resler, T.R. Gattuso, D.H. Altman, K.H. Sandhage, L. Shi, A. Henry, B. A. Cola, Nat. Nanotechnol. 9 (2014) 384.
[45] Y. Xu, d Kraemer, B. Song, Z. Jiang, J. Zhou, J. Loomis, J. Wang, M. Li, H. Ghasemi, X. Huang, X. Li, G. Chen, Nat. Commun. 10 (2019) 1771.
[46] N. Bruger, A. Laachachi, B. Mortazavi, M. Ferriol, M. Lutz, V. Toniazzo, D. Ruch, Int. J. Heat. Mass Transf. 89 (2015) 505.
[47] J. Han, G. Du, W. Gao, H. Bai, Adv. Funct. Mater. 29 (2019) 1900412.
[48] J. Ying, X. Tan, L. Lv, X. Wang, J. Gao, Q. Yan, H. Ma, K. Nishimura, H. Li, J. Yu, T.-H. Liu, R. Xiang, R. Sun, N. Jiang, C.-P. Wong, S. Maruyama, C.-T. Lin, W. Dai, ACS Nano 15 (2021) 12922.
[49] X. Xu, S. Fu, J. Guo, H. Li, Y. Huang, X. Duan, Mater. Today 42 (2021) 162.
[50] A. Du, H. Wang, B. Zhou, C. Zhang, X. Wu, Y. Ge, T. Niu, X. Ji, T. Zhang, Z. Zhang, G. Wu, J. Shen, Chem. Mater. 30 (2018) 6849.
[51] Y. Cui, H. Gong, Y. Wang, D. Li, H. Bai, Adv. Mater. 30 (2018) 1706807.
[52] Y. Si, X. Wang, L. Dou, J. Yu, B. Ding, Sci. Adv. 4 (2018) eaas8925.
[53] M.J. Oh, J.H. Lee, P.J. Yoo, Adv. Funct. Mater. 31 (2021) 2007392.
[54] T. Han, X. Bai, J.T.L. Thong, B. Li, C.W. Qiu, Adv. Mater. 26 (2014) 1731.
[55] Y. Li, X. Bai, T. Yang, H. Luo, C.W. Qiu, Nat. Commun. 9 (2018) 273.
[56] A.P. Raman, M.A. Anoma, L. Zhu, E. Rephaeli, S. Fan, Nature 515 (2014) 540.
[57] E. Rephaeli, A. Raman, S. Fan, Nano Lett. 13 (2013) 1457.
[58] P.C. Hsu, A.Y. Song, P.B. Catrysse, C. Liu, Y. Peng, J. Xie, S. Fan, Y. Cui, Science 353 (2016) 1019.
[59] X. Zhang, S. Yu, B. Xu, M. Li, Z. Peng, Y. Wang, S. Deng, X. Wu, Z. Wu, M. Ouyang, Y. Wang, Science 363 (2019) 619.
[60] X. Liu, C. Xiao, P. Wang, M. Yan, H. Wang, P. Xie, G. Liu, H. Zhou, D. Zhang, T. Fan, Adv. Opt. Mater. 9 (2021) 2101151.
[61] J. Yang, G. Qi, L. Tang, R. Bao, L. Bai, Z. Liu, W. Yang, B. Xie, M. Yang, J. Mater. Chem. A 4 (2016) 9625.
[62] Z. Wang, Z. Tong, Q. Ye, H. Hu, X. Nie, C. Yan, W. Shang, C. Song, J. Wu, J. Wang, H. Bao, P. Tao, T. Deng, Nat. Commun. 8 (2017) 1478.
[63] L. Zhou, Y. Tan, J. Wang, W. Xu, Y. Yuan, W. Cai, S. Zhu, J. Zhu, Nat. Photonics 10 (2016) 393.
[64] X. Li, W. Xu, M. Tang, L. Zhou, B. Zhu, S. Zhu, J. Zhu, Proc. Natl. Acad. Sci. U. S. A. 113 (2016) 13953.
[65] H. Ghasemi, G. Ni, A.M. Marconnet, J. Loomis, S. Yerci, N. Miljkovic, G. Chen, Nat. Commun. 5 (2014) 4449.
[66] Y. Li, T. Gao, Z. Yang, C. Chen, W. Luo, J. Song, E. Hitz, C. Jia, Y. Zhou, B. Liu, B. Yang, L. Hu, Adv. Mater. 29 (2017) 1700981.
[67] M. Gao, L. Zhu, C.K. Peh, G.W. Ho, Energy Environ. Sci. 12 (2019) 841.
[68] S. Lee, G. Hwang, T.H. Kim, S.J. Kwon, J.U. Kim, K. Koh, B. Park, H. Hong, K. J. Yu, H. Chae, Y. Jung, J. Lee, T.I. Kim, ACS Nano 12 (2018) 6756.
[69] W. Guo, C. Guo, N. Zheng, T. Sun, S. Liu, Adv. Mater. 29 (2017) 1604157.
[70] C.M. Hessel, V.P. Pattani, M. Rasch, M.G. Panthani, B. Koo, J.W. Tunnell, B. A. Korgel, Nano Lett. 11 (2011) 2560.
[71] P. Vijayaraghavan, C.H. Liu, R. Vankayala, C.S. Chiang, K.C. Hwang, Adv. Mater. 26 (2014) 6689.

[72] M. Zhu, Y. Li, F. Chen, X. Zhu, J. Dai, Y. Li, Z. Yang, X. Yan, J. Song, Y. Wang, T. Hitz, W. Luo, M. Lu, B. Yang, L. Hu, Adv. Energy Mater. 8 (2018) 1701028.
[73] K. Bae, G. Kang, S.K. Cho, W. Park, K. Kim, W.J. Padilla, Nat. Commun. 6 (2015) 10103.
[74] L. Zhou, Y. Tan, D. Ji, B. Zhu, P. Zhang, J. Xu, Q. Gan, Z. Yu, J. Zhu, Sci. Adv. 2 (2016), e1501227.
[75] K. Yamamoto, S. Akita, Y. Nakayama, J. Phys. D. Appl. Phys. 31 (1998) L34.
[76] S.J. Papadakis, Z. Gu, D.H. Gracias, Appl. Phys. Lett. 88 (2006), 233118.
[77] X. Chen, T. Saito, H. Yamada, K. Matsushige, Appl. Phys. Lett. 78 (2001) 3714.
[78] C.A. Martin, J.K.W. Sandler, A.H. Windle, M.K. Schwarz, W. Bauhofer, K. Schulte, M.S.P. Shaffer, Polymer 46 (2005) 877.
[79] A.I. Oliva-Aviles, F. Aviles, V. Sosa, A.I. Oliva, F. Gamboa, Nanotechnology 23 (2012), 465710.
[80] T. Prasse, J.Y. Cavaille, W. Bauhofer, Compos. Sci. Technol. 63 (2003) 1835.
[81] C.A. Martin, J.K.W. Sandler, M.S.P. Shaffer, M.K. Schwarz, W. Bauhofer, K. Schulte, A.H. Windle, Compos. Sci. Technol. 64 (2004) 2309.
[82] M. Monti, M. Natali, L. Torre, J.M. Kenny, Carbon 50 (2012) 2453.
[83] E.M. Remillard, Q. Zhang, S. Sosina, Z. Branson, T. Dasgupta, C.D. Vecitis, Carbon 100 (2016) 578.
[84] Y. Zhu, C. Ma, W. Zhang, R. Zhang, N. Koratkar, J. Liang, J. Appl. Phys. 105 (2009), 054319.
[85] F. Besharat, M. Manteghian, G. Gallone, A. Lazzeri, Nanotechnology 31 (2020), 155701.
[86] C. Ma, W. Zhang, Y. Zhu, L. Ji, R. Zhang, N. Koratkar, J. Liang, Carbon 46 (2008) 706.
[87] C. Park, J. Wilkinson, S. Banda, Z. Ounaies, K.E. Wise, G. Sauti, P.T. Lillehei, J. S. Harrison, J. Polym. Sci. Part B: Polym. Phys. 44 (2006) 1751.
[88] R.M. Erb, R. Libanori, N. Rothfuchs, A.R. Studart, Science 335 (2012) 199.
[89] J.M.D. Coey, Magnetism and magnetic materials, Cambridge University Press, Cambridge, 2010.
[90] K. Ni, Q. Peng, E. Gao, K. Wang, Q. Shao, H. Huang, L. Xue, Z. Wang, ACS Nano 15 (2021) 4747.
[91] C. Yuan, B. Duan, L. Li, B. Xie, M. Huang, X. Luo, ACS Appl. Mater. Interfaces 7 (2015) 13000.
[92] S.J. Park, S. Kim, S. Lee, Z.G. Khim, K. Char, T. Hyeon, J. Am. Chem. Soc. 122 (2000) 8581.
[93] L.M. Parkes, R. Hodgson, L.T. Lu, L.D. Tung, I. Robinson, D.G. Fernig, N.T. K. Thanh, Contrast Media Mol. Imaging 3 (2008) 150.
[94] J.F. Bondi, K.D. Oyler, X. Ke, P. Schiffer, R.E. Schaak, J. Am. Chem. Soc. 131 (2009) 9144.
[95] Y.L. Hou, S. Gao, J. Mater. Chem. 13 (2003) 1510.
[96] K. Liu, L. Han, P. Tang, K. Yang, D. Gan, X. Wang, K. Wang, F. Ren, L. Fan, Y. Xu, Z. Lu, X. Lu, Nano Lett. 19 (2019) 8343.
[97] M. Reches, E. Gazit, Nat. Nanotechnol. 1 (2006) 195.
[98] Y. Huangfu, C. Liang, Y. Han, H. Qiu, P. Song, L. Wang, J. Kong, J. Gu, Compos. Sci. Technol. 169 (2019) 70.
[99] R.M. Erb, K.H. Cherenack, R.E. Stahel, R. Libanori, T. Kinkeldei, N. Munzenrieder, G. Troster, A.R. Studart, ACS Appl. Mater. Interfaces 4 (2012) 2860.
[100] J.J. Martin, B.E. Fiore, R.M. Erb, Nat. Commun. 6 (2015) 86411.
[101] J. Yan, S.C. Bae, K. Granick, Adv. Mater. 27 (2015) 874.
[102] F. Lin, G. Yang, C. Niu, Y. Wang, Z. Zhu, H. Luo, C. Dai, D. Mayerich, Y. Hu, J. Hu, X. Zhou, Z. Liu, Z.M. Wang, J. Bao, Adv. Funct. Mater. 28 (2018) 1805255.
[103] C. Liu, J. Cai, D. Gong, W. Zhang, D. Zhang, J. Magn. Magn. Mater. 484 (2019) 472.
[104] R. Sheparovych, Y. Sahoo, M. Motornov, S. Wang, H. Luo, P.N. Prasad, I. Sokolov, S. Minko, Chem. Mater. 18 (2006) 591.
[105] Y.I. Frenkel, Kinetic theory of liquids, Dover Publications, Mineola, NY, USA, 1955.
[106] L. Liang, P. Xu, Y. Wang, Y. Shang, J. Ma, F. Su, Y. Feng, G. He, Y. Wang, C. Liu, Chem. Eng. J. 395 (2020), 125209.
[107] C. Yu, W. Gong, W. Tian, Q. Zhang, Y. Xu, Z. Lin, M. Hu, X. Fan, Y. Yao, Compos. Sci. Technol. 160 (2018) 199.
[108] S. Shen, A. Henry, J. Tong, R. Zheng, G. Chen, Nat. Nanotechnol. 5 (2010) 251.
[109] S. Ronca, T. Igarashi, G. Forte, S. Rastogi, Polymer 123 (2017) 203.
[110] R. Zhang, Z. Huang, Z. Huang, M. Zhong, D. Zang, A. Lu, Y. Lin, B. Millar, G. Garet, J. Turner, Compos. Sci. Technol. 196 (2020), 108154.
[111] A. Peterlin, Colloid Polym. Sci. 265 (1987) 357.
[112] N.A.J.M. Van Aerle, A.W.M.A. Braam, J. Mater. Sci. 23 (1988) 4429.
[113] X. Pan, L. Shen, A.P.H.J. Schenning, C.W.M. Bastiaansen, Adv. Mater. 31 (2019) 1904348.
[114] K. Zhao, S. Li, M. Huang, X. Shi, G. Zheng, C. Liu, K. Dai, C. Shen, R. Yin, J.Z. Guo, Chem. Eng. J. 358 (2019) 924.
[115] W. Song, M. Cao, M. Lu, J. Yang, H. Ju, Z. Hou, J. Liu, J. Yuan, L. Fan, Nanotechnology 24 (2013), 115708.
[116] G. Yang, X. Zhang, Y. Shang, P. Xu, D. Pan, F. Su, Y. Ji, Y. Feng, Y. Liu, C. Liu, Compos. Sci. Technol. 201 (2021), 108521.
[117] F. Zeng, C. Xue, H. Ma, C.-T. Lin, J. Yu, N. Jiang, Materials 13 (2020) 46.
[118] G. Yuan, X. Li, Z. Dong, A. Westwood, Z. Cui, Y. Cong, H. Du, F. Kang, Carbon 50 (2012) 175.
[119] J. Hu, Y. Huang, X. Zeng, Q. Li, L. Ren, R. Sun, J. Xu, C.-P. Wong, Compos. Sci. Technol. 160 (2018) 127.
[120] W.A. Deheer, W.S. Bacsa, A. Chatelain, T. Gerfin, R. Humphrey-Baker, L. Forro, D. Ugarte, Science 268 (1995) 845.
[121] Z. Wu, Z. Chen, X. Du, J.M. Logan, J. Sippel, M. Nikolou, K. Kamaras, J. R. Reynolds, D.B. Tanner, A.F. Hebard, A.G. Rinzler, Science 305 (2004) 1273.
[122] Z. Bo, C. Ying, H. Zhu, X. Wei, H. Yang, J. Yan, K. Cen, Appl. Therm. Eng. 150 (2019) 1016.
[123] X. Wang, P. Wu, ACS Appl. Mater. Interfaces 11 (2019) 21946.
[124] X. Wang, P. Wu, ACS Appl. Mater. Interfaces 10 (2018) 34311.
[125] Z. Wang, Y. Yang, Z. Zheng, R. Lan, K. Dan, L. Xu, H. Huang, J. Tang, J. Xu, Z. Li, Compos. Sci. Technol. 194 (2020), 108190.
[126] L. Jia, Y. Jin, J. Ren, L. Zhao, D. Yan, Z. Li, J. Mater. Chem. C. 9 (2021) 2904.
[127] X. He, W. Gao, L. Xie, B. Li, Q. Zhang, S. Lei, J.M. Robinson, E.H. Haroz, S. K. Doorn, W. Wang, R. Vajtai, P.M. Ajayan, W.W. Adams, R.H. Hauge, J. Kono, Nat. Nanotechnol. 11 (2016) 633.
[128] R.S. McLean, X. Huang, C. Khripin, A. Jagota, M. Zheng, Nano Lett. 6 (2006) 55.
[129] Z. Ling, C.E. Ren, M. Zhao, J. Yang, J.M. Giammarco, J. Qiu, M.W. Barsoum, Y. Gogotsi, Proc. Natl. Acad. Sci. U. S. A. 111 (2014) 16676.
[130] Y. Xu, W. Hong, H. Bai, C. Li, G. Shi, Carbon 47 (2009) 3538.
[131] S. Wan, J. Peng, Y. Li, H. Hu, L. Jiang, Q. Cheng, ACS Nano 9 (2015) 9830.
[132] F. Shahzad, M. Alhabeb, C.B. Hatter, B. Anasori, S.M. Hong, C.M. Koo, Y. Gogotsi, Science 353 (2016) 1137.
[133] Y. Wu, Y. Xue, S. Qin, D. Liu, X. Wang, X. Hu, J. Li, X. Wang, Y. Bando, D. Golberg, Y. Chen, Y. Gogotsi, W. Lei, ACS Appl. Mater. Interfaces 9 (2017) 43163.
[134] S. Wan, Y. Li, J. Peng, H. Hu, Q. Cheng, L. Jiang, ACS Nano 9 (2015) 708.
[135] J. Feng, D. Zhang, M. Zhu, C. Gao, J. Mater. Chem. B 5 (2017) 5176.
[136] L. Li, S.K. Hong, Y. Jo, M. Tian, C.Y. Woo, S.H. Kim, J.-M. Kim, H.W. Lee, ACS Appl. Mater. Interfaces 11 (2019) 16223.
[137] Y. Fang, J. Dong, X. Zhao, T. Chen, L. Xiang, Y. Xie, Q. Zhang, Compos. Part B 199 (2020), 108281.
[138] K. Lee, M. Do, Y.C. Seo, H. Lee, Adv. Mater. Interfaces 5 (2018) 1800585.
[139] X. Zhang, J. Jiang, Z. Shen, Z. Dan, M. Li, Y. Lin, C.-W. Nan, L. Chen, Y. Shen, Adv. Mater. 30 (2018) 1707269.
[140] Y. Lu, X. Xiao, Y. Zhan, C. Huan, S. Qi, H. Cheng, G. Xu, ACS Appl. Mater. Interfaces 10 (2018) 12759.
[141] X. Zhang, B. Wang, N. Wu, C. Han, Y. Wang, Chem. Eng. J. 410 (2021), 128304.
[142] W. Takarada, K. Sugimoto, H. Nakajima, H.A. Visser, G.J.M. Gruter, T. Kikutani, Materials 14 (2021) 1172.
[143] J. Liang, Polym. Test. 77 (2019), 105926.
[144] J. Vasiljevic, A. Demsar, M. Leskovsek, B. Simoncic, N. Celan Korosin, I. Jerman, M. Sobak, G. Zitko, N. Van de Velde, M. Colovic, Polymers 12 (2020) 1787.
[145] A.R. Bhattacharyya, T.V. Sreekumar, T. Liu, S. Kumar, L.M. Ericson, R.H. Hauge, R.E. Smalley, Polymer 44 (2003) 2373.
[146] Y. Shen, H. Orelma, A. Sneck, K. Kataja, J. Salmela, P. Qvintus, A. Suurnakki, A. Harlin, Cellulose 23 (2016) 3393.
[147] L.K.J. Hauru, M. Hummel, A. Michud, H. Sixta, Cellulose 24 (2017) 3109.
[148] Z. Xu, Y. Zhang, P. Li, C. Gao, ACS Nano 6 (2012) 7103.
[149] Z. Liu, J. Lyu, D. Fang, X. Zhang, ACS Nano 13 (2019) 5703.
[150] G. Li, G. Hong, D. Dong, W. Song, X. Zhang, Adv. Mater. 30 (2018) 1801754.
[151] Y. Wang, Y. Cui, Z. Shao, W. Gao, W. Fan, T. Liu, H. Bai, Chem. Eng. J. 390 (2020), 124623.
[152] S. Deville, E. Saiz, R.K. Nalla, A.P. Tomsia, Science 311 (2006) 515.
[153] F. Qian, P.C. Lan, M.C. Freyman, W. Chen, T. Kou, T.Y. Olson, C. Zhu, M. A. Worsley, E.B. Duoss, C.M. Spadaccini, T. Baumann, T.Y.-J. Han, Nano Lett. 17 (2017) 7171.
[154] Y. Yao, X. Zhu, X. Zeng, R. Sun, J. Xu, C.-P. Wong, ACS Appl. Mater. Interfaces 10 (2018) 9669.
[155] J. Bai, Y. Huang, Q. Gong, X. Liu, Y. Li, J. Gao, M. Zhao, Y. Shao, D. Zhuang, J. Liang, Carbon 137 (2018) 493.
[156] B. Wicklein, A. Kocjan, G. Salazar-Alvarez, F. Carosio, G. Camino, M. Antonietti, L. Bergstrom, Nat. Nanotechnol. 10 (2015) 277.
[157] Z. Wang, X. Shen, N.M. Han, X. Liu, Y. Wu, W. Ye, J.-K. Kim, Chem. Mater. 28 (2016) 6731.
[158] X. Zeng, L. Ye, S. Yu, R. Sun, J. Xu, C.-P. Wong, Chem. Mater. 27 (2015) 5849.
[159] X. Zeng, Y. Yao, Z. Gong, F. Wang, R. Sun, J. Xu, C.P. Wong, Small 11 (2015) 6205.
[160] H. Bai, Y. Chen, B. Delattre, A.P. Tomsia, R.O. Ritchie, Sci. Adv. 1 (2015), e1500849.
[161] Y. Wu, Z. Wang, X. Shen, X. Liu, N.M. Han, Q. Zheng, Y. Ma, J.-K. Kim, ACS Appl. Mater. Interfaces 10 (2018) 26641.
[162] N. Zhao, M. Yang, Q. Zhao, W. Gao, T. Xie, H. Bai, ACS Nano 11 (2017) 4777.
[163] C. Wang, X. Chen, B. Wang, M. Huang, B. Wang, Y. Jiang, R.S. Ruoff, ACS Nano 12 (2018) 5816.
[164] N.M. Han, Z. Wang, X. Shen, Y. Wu, X. Liu, Q. Zheng, T.-H. Kim, J. Yang, J.-K. Kim, ACS Appl. Mater. Interfaces 10 (2018) 6580.
[165] J. Hu, Y. Huang, Y. Yao, G. Pan, J. Sun, X. Zeng, R. Sun, J. Xu, B. Song, C.-P. Wong, ACS Appl. Mater. Interfaces 9 (2017) 13544.
[166] Y. Yao, J. Sun, X. Zeng, R. Sun, J. Xu, C.-P. Wong, Small 14 (2018) 1704044.
[167] J. Zou, H. Xiong, Y. Huang, Z. Wang, J. Wen, W. Du, J. Cao, Ceram. Int. 47 (2021) 27386.
[168] P. Zhang, J. Li, L. Lv, Y. Zhao, L. Qu, ACS Nano 11 (2017) 5087.
[169] S. Wu, C. Zhu, Z. He, H. Xue, Q. Fan, Y. Song, J.S. Francisco, X. Zeng, J. Wang, Nat. Commun. 8 (2017) 15154.
[170] H. Yao, J. Ge, C. Wang, X. Wang, W. Hu, Z. Zheng, Y. Ni, S. Yu, Adv. Mater. 25 (2013) 6692.
[171] C. Wu, X. Huang, X. Wu, R. Qian, P. Jiang, Adv. Mater. 25 (2013) 5658.
[172] X. Wang, P. Wu, Chem. Eng. J. 348 (2018) 723.
[173] D.D. Nguyen, N.-H. Tai, S.-B. Lee, W.-S. Kuo, Energy Environ. Sci. 5 (2012) 7908.
[174] M. Karthik, A. Faik, P. Blanco-Rodriguez, J. Rodriguez-Aseguinolaza, B. D'Aguanno, Carbon 94 (2015) 266.

[175] Z. Wang, X. Liu, X. Shen, N.M. Han, Y. Wu, Q. Zheng, J. Jia, N. Wang, J.-K. Kim, Adv. Funct. Mater. 28 (2018) 1707043.
[176] A. Reina, X. Jia, J. Ho, D. Nezich, H. Son, V. Bulovic, M.S. Dresselhaus, J. Kong, Nano Lett. 9 (2009) 30.
[177] X. Li, W. Cai, J. An, S. Kim, J. Nah, D. Yang, R. Pnier, A. Velamakanni, I. Jung, E. Tutuc, S.K. Banerjee, L. Colombo, R.S. Ruoff, Science 324 (2009) 1312.
[178] A. Ismach, H. Chou, D.A. Ferrer, Y. Wu, S. McDonnell, H.C. Floresca, A. Covacevich, C. Pope, R. Piner, M.J. Kim, R.M. Wallace, L. Colombo, R.S. Ruoff, ACS Nano 6 (2012) 6378.
[179] L. Song, L. Ci, H. Lu, P.B. Sorokin, C. Jin, J. Ni, A.G. Kvashnin, D.G. Kvashnin, J. Lou, B.I. Yakobson, P.M. Ajayan, Nano Lett. 10 (2010) 3209.
[180] Y. Shi, N. Li, L.-J. Li, Chem. Soc. Rev. 44 (2015) 2744.
[181] Z. Chen, W. Ren, L. Gao, B. Liu, S. Pei, H. Cheng, Nat. Mater. 10 (2011) 424.
[182] M.C. Vu, W.-K. Choi, S.G. Lee, P.J. Park, D.H. Kim, M.A. Islam, S.-R. Kim, ACS Appl. Mater. Interfaces 12 (2020) 23388.
[183] L. Lv, P. Zhang, H. Cheng, Y. Zhao, Z. Zhang, G. Shi, L. Qu, Small 12 (2016) 3229.
[184] H. Yang, Z. Li, B. Lu, J. Gao, X. Jin, G. Sun, G. Zhang, P. Zhang, L. Qu, ACS Nano 12 (2018) 11407.
[185] X. Zhang, T. Zhang, Z. Wang, Z. Ren, S. Yan, Y. Duan, J. Zhang, ACS Appl. Mater. Interfaces 11 (2019) 1303.
[186] J. Li, F. Li, X. Zhao, W. Zhang, S. Li, Y. Lu, L. Zhang, ACS Appl. Electron. Mater. 2 (2020) 1661.
[187] B. Xie, Y. Wang, H. Liu, J. Ma, S. Zhou, X. Yu, W. Lan, K. Wang, R. Hu, X. Luo, Chem. Eng. J. 427 (2022), 130958.
[188] R.L. Truby, J.A. Lewis, Nature 540 (2016) 371.
[189] R.D. Farahani, M. Dube, Adv. Eng. Mater. 20 (2018) 1700539.
[190] R.D. Farahani, M. Dube, D. Therriault, Adv. Mater. 28 (2016) 5794.
[191] M.K. Gupta, F. Meng, B.N. Johnson, Y.L. Kong, L. Tian, Y.-W. Yeh, N. Masters, S. Singamaneni, M.C. McAlpine, Nano Lett. 15 (2015) 5321.
[192] J. Malda, J. Visser, F.P. Melchels, T. Jungst, W.E. Hennink, W.J.A. Dhert, J. Groll, D.W. Hutmacher, Adv. Mater. 25 (2013) 5011.
[193] G. Villar, A.D. Graham, H. Bayley, Science 340 (2013) 48.
[194] T. Gissibl, S. Thiele, A. Herkommer, H. Giessen, Nat. Photonics 10 (2016) 554.
[195] B.J. de Gans, P.C. Duineveld, U.S. Schubert, Adv. Mater. 16 (2004) 203.
[196] Y.L. Kong, M.K. Gupta, B.N. Johnson, M.C. McAlpine, Nano Today 11 (2016) 330.
[197] K. Fu, Y. Yao, J. Dai, L. Hu, Adv. Mater. 29 (2017) 1603486.
[198] S.-N. Kwon, S.-W. Kim, I.-G. Kim, Y.-K. Hong, S.-I. Na, Adv. Mater. Technol. 4 (2019) 1800500.
[199] N.S. Hmeidat, J.W. Kemp, B.G. Compton, Compos. Sci. Technol. 160 (2018) 9.
[200] A.E. Jakus, E.B. Secor, A.L. Rutz, S.W. Jordan, M.C. Hersam, R.N. Shah, ACS Nano 9 (2015) 4636.
[201] U.G.K. Wegst, H. Bai, E. Saiz, A.P. Tomsia, R.O. Ritchie, Nat. Mater. 14 (2015) 23.
[202] M.E. Launey, M.J. Buehler, R.O. Ritchie, Annu. Rev. Mater. Res. 40 (2010) 25.
[203] L.J. Gibson, J. R. Soc. Interface 9 (2012) 2749.
[204] H. Kodama, Rev. Sci. Instrum. 52 (1981) 1770.
[205] R.D. Goodridge, C.J. Tuck, R.J.M. Hague, Prog. Mater. Sci. 57 (2012) 229.
[206] D. Kokkinis, M. Schaffner, A.R. Studart, Nat. Commun. 6 (2015) 8643.
[207] B.G. Compton, J.A. Jewis, Adv. Mater. 26 (2014) 5930.
[208] I. Zein, D.W. Hutmacher, K.C. Tan, S.H. Teoh, Biomaterials 23 (2002) 1169.
[209] W.E. King, A.T. Anderson, R.M. Ferencz, N.E. Hodge, C. Kamath, S.A. Khairallah, A.M. Rubenchik, Appl. Phys. Rev. 2 (2015), 041304.
[210] Z. Liang, Y. Pei, C. Chen, B. Jiang, Y. Yao, H. Xie, M. Jiao, G. Chen, T. Li, B. Yang, L. Hu, ACS Nano 13 (2019) 12653.
[211] P.K. Penumakala, J. Santo, A. Thomas, Compos. Part B 201 (2020), 108336.
[212] H.C. Guo, H. Zhao, H. Niu, Y. Ren, H. Fang, X. Fang, R. Lv, M. Maqbool, S. Bai, ACS Nano 15 (2021) 6917.
[213] N. Nguyen, J.G. Park, S. Zhang, R. Liang, Adv. Eng. Mater. 20 (2018) 1700876.
[214] W. Dai, L. Lv, T. Ma, X. Wang, J. Ying, Q. Yan, X. Tan, J. Gao, C. Xue, J. Yu, Y. Yao, Q. Wei, R. Sun, Y. Wang, T.-H. Liu, T. Chen, R. Xiang, N. Jiang, Q. Xue, C.-P. Wong, S. Maruyama, C.-T. Lin, Adv. Sci. 8 (2021) 2003734.
[215] G. Lewis, Biomaterials 22 (2001) 371.
[216] T. Feng, A. Rai, D. Hun, S.S. Shrestha, Int. J. Heat. Mass Transf. 164 (2021), 120459.
[217] X. Wei, Z. Wang, Z. Tian, T. Luo, J. Heat. Transf. 143 (2021), 072101.
[218] A. Henry, Annu. Rev. Heat. Transf. 17 (2014) 485.
[219] A.A. Balandin, Nat. Mater. 10 (2011) 569.
[220] A. Henry, G. Chen, Phys. Rev. Lett. 101 (2008), 235402.
[221] J. Liu, R. Yang, Phys. Rev. B 86 (2012), 104307.
[222] C.L. Choy, Y. Fei, T.G. Xi, J. Polym. Sci. Part B: Polym. Phys. 31 (1993) 365.
[223] P. Smith, P.J. Lemstra, J. Mater. Sci. 15 (1980) 505.
[224] C.L. Choy, W.H. Luk, F.C. Chen, Polymer 19 (1978) 155.
[225] H. Fujishiro, M. Ikebe, T. Kashima, A. Yamanaka, Jpn. J. Appl. Phys. 37 (1998) 1994.
[226] B. Zhu, J. Liu, T. Wang, M. Han, S. Valloppilly, S. Xu, X. Wang, ACS Omega 2 (2017) 3931.
[227] R. Shrestha, P. Li, B. Chatterjee, T. Zheng, X. Wu, Z. Liu, T. Luo, S. Choi, K. Hippalgaonkar, M.P. de Boer, S. Sheng, Nat. Commun. 9 (2018) 1664.
[228] A. Shanker, C. Li, G.-H. Kim, D. Gidley, K.P. Pipe, J. Kim, Sci. Adv. 3 (2017), e1700342.
[229] Z. Zhong, M.C. Wingert, J. Strzalka, H.-H. Wang, T. Sun, J. Wang, R. Chen, Z. Jiang, Nanoscale 6 (2014) 8283.
[230] C. Canetta, S. Guo, A. Narayanaswamy, Rev. Sci. Instrum. 85 (2014), 104901.
[231] J. Ma, Q. Zhang, A. Mayo, Z. Ni, H. Yi, Y. Chen, R. Mu, L.M. Bellan, D. Li, Nanoscale 7 (2015) 16899.
[232] O. Ero-Philips, M. Jenkins, A. Stamboulis, Polymers 4 (2012) 1331.
[233] Y. Yao, Z. Ye, F. Huang, X. Zeng, T. Zhang, T. Shang, M. Han, W. Zhang, L. Ren, R. Sun, J. Xu, C.-P. Wong, ACS Appl. Mater. Interfaces 12 (2020) 2892.
[234] C. Guan, Y. Qin, B. Wang, L. Li, M. Wang, C.-T. Lin, X. He, K. Nishimura, J. Yu, J. Yi, N. Jiang, Compos. Part B 198 (2020), 108167.
[235] T. Wang, T. Fan, D. Zhang, G. Zhang, D. Xiong, Mater. Lett. 61 (2007) 1849.
[236] W. Yang, L. Zhou, K. Peng, J. Zhu, L. Wan, Compos. Part B 55 (2013) 1.
[237] T. Oya, T. Nomura, M. Tsubota, N. Okinaka, T. Akiyama, Appl. Therm. Eng. 61 (2013) 825.
[238] K.M.F. Shahil, A.A. Balandin, Nano Lett. 12 (2012) 861.
[239] V. Datsyuk, S. Trotsenko, S. Reich, Carbon 52 (2013) 605.
[240] L.C. Herrerz-Ramirez, M. Cano, R.G. de Villoria, Compos. Sci. Technol. 151 (2017) 211.
[241] J.C.M. Garnett, Philos. Trans. R. Soc. A 203 (1904) 385.
[242] W. Woodside, J.H. Messmer, J. Appl. Phys. 32 (1961) 1688.
[243] Y.A.T. Uno, J. Appl. Polym. Sci. 32 (1986) 5705.
[244] R.L. Hamilton, et al., Ind. Eng. Chem. Fundam. 1 (1962) 187.
[245] T.B. Lewis, L.E. Nielsen, J. Appl. Polym. Sci. 14 (1970) 1449.
[246] S.C. Cheng, R.I. Vachon, Int. J. Heat. Mass Transf. 12 (1969) 249.
[247] S.C. Cheng, R.I. Vachon, Int. J. Heat. Mass Transf. 13 (1970) 537.
[248] M. Wang, N. Pan, Mater. Sci. Eng. R. 63 (2008) 1.
[249] P. Bonnet, D. Sireude, B. Garnier, O. Chauvet, Appl. Phys. Lett. 91 (2007), 201910.
[250] J. Zhang, Y. Chen, Z. Nie, Z. Chen, J. Gao, Sci. Rep. 10 (2020) 20843.
[251] X. Ye, J. Hu, B. Li, M. Hong, Y. Zhang, Chem. Eng. J. 361 (2019) 1110.
[252] K. Uetani, S. Ata, S. Tomonoh, T. Yamada, M. Yumura, K. Hata, Adv. Mater. 26 (2014) 5857.
[253] H. Huang, C. Liu, Y. Wu, S. Fan, Adv. Mater. 17 (2005) 1652.
[254] J. He, H. Wang, Z. Su, Y. Guo, Q. Qu, T. Qin, X. Tian, ACS Appl. Polym. Mater. 1 (2019) 2807.
[255] C. Fu, C. Yan, L. Ren, X. Zeng, G. Du, R. Sun, J. Xu, C.-P. Wong, Compos. Sci. Technol. 177 (2019) 118.
[256] E.S. Choi, J.S. Brooks, D.L. Eaton, M.S. Al-Haik, M.Y. Hussaini, H. Garmestani, D. Li, K. Dahmen, J. Appl. Phys. 94 (2003) 6034.
[257] Z. Xu, G. Lin, G. Sui, J. Appl. Polym. Sci. 137 (2020), e49212.
[258] B. Vigolo, A. Penicaud, C. Coulon, C. Sauder, R. Pailler, C. Journet, P. Bernier, P. Poulin, Science 290 (2000) 1331.
[259] T. Kimura, H. Ago, M. Tobita, S. Ohshima, M. Kyotani, M. Yumura, Adv. Mater. 14 (2002) 1380.
[260] H. Garmestani, M.S. Al-Haik, D. Dahmen, R. Tannenbaum, D.S. Li, S.S. Sablin, M. Y. Hussaini, Adv. Mater. 15 (2003) 1918.
[261] D. Shi, P. He, P. Zhao, F. Guo, F. Wang, C. Huthh, X. Chaud, S.L. Bud'ko, J. Lian, Compos. Part B 42 (2011) 1532.
[262] S.G. Prolongo, B.G. Meliton, G. Del Rosario, A. Urena, Compos. Part B 46 (2013) 166.
[263] T. Chatterjee, C.A. Mitchell, V.G. Hadjiev, R. Krishnamoorti, Macromolecules 45 (2012) 9357.
[264] A. Sulong, J. Park, J. Compos. Mater. 45 (2011) 931.
[265] S. Abbasi, P.J. Carreau, A. Derdouri, Polymer 51 (2010) 922.
[266] A.E. Eken, E.J. Tozzi, D.J. Klingenberg, W. Bauhofer, J. Appl. Phys. 109 (2011), 084342.
[267] T. Tong, Y. Zhao, L. Delzeit, A. Kashani, M. Meyyappan, A. Majumdar, IEEE Trans. Compon. Packag. Technol. 30 (2007) 92.
[268] A.M. Marconnett, N. Yamamoto, M.A. Panzer, B.L. Wardle, K.E. Goodson, ACS Nano 5 (2011) 4818.
[269] I. Ivanov, A. Puretzky, G. Eres, H. Wang, Z. Pan, H. Cui, R. Jin, J. Howe, D. B. Geohegan, Appl. Phys. Lett. 89 (2006), 223110.
[270] D. Hu, W. Gong, J. Di, R. Li, W. Lu, B. Gu, B. Sun, Q. Li, Carbon 118 (2017) 659.
[271] C. Liu, S. Fan, Appl. Phys. Lett. 86 (2005), 123106.
[272] A. Yu, M.E. Itkis, E. Bekyarova, R.C. Haddon, Appl. Phys. Lett. 89 (2006), 133102.
[273] F.H. Gojny, M.H.G. Wichmann, B. Fiedler, I.A. Kinloch, W. Bauhofer, A.H. Windle, K. Schulte, Polymer 47 (2006) 2036.
[274] K. Wu, J. Fang, J. Ma, R. Huang, S. Chai, F. Chen, Q. Fu, ACS Appl. Mater. Interfaces 9 (2017) 30035.
[275] T. Ma, Y. Zhao, K. Ruan, X. Liu, J. Zhang, Y. Guo, X. Yang, J. Kong, J. Gu, ACS Appl. Mater. Interfaces 12 (2020) 1677.
[276] H. Zeng, J. Wu, Y. Ma, Y. Ye, J. Liu, X. Li, Y. Wang, Y. Liao, Y. Wang, Y. Liao, X. Luo, X. Xie, Y. Mai, ACS Appl. Mater. Interfaces 10 (2018) 41690.
[277] Q. Liang, X. Yao, W. Wang, Y. Liu, C.-P. Wong, ACS Nano 5 (2011) 2392.
[278] Y. Yao, X. Zeng, F. Wang, R. Sun, J. Xu, C.-P. Wong, Chem. Mater. 28 (2016) 1049.
[279] S. Yamaguchi, I. Tsunekawa, N. Komatsu, G. Gao, T. Shiga, T. Kodama, J. Kono, J. Shiomi, Appl. Phys. Lett. 115 (2019), 223104.
[280] D. Rozmanov, P.G. Kusalik, Anisotropy in the crystal growth of hexagonal ice, I-h, J. Chem. Phys. 137 (2012), 094702.
[281] M. Marcellini, C. Noirjean, D. Dedovets, J. Maria, S. Deville, ACS Omega 1 (2016) 1019.
[282] K.L. Scotti, D.C. Dunand, Prog. Mater. Sci. 94 (2018) 243.
[283] H. Zhao, Y. Yue, L. Guo, J. Wu, Y. Zhang, D. Li, S. Mao, X. Han, Adv. Mater. 28 (2016) 5099.
[284] H. Bai, F. Walsh, B. Gludovata, B. Delattre, C. Huang, Y. Chen, A.P. Tomsia, R. O. Ritchie, Adv. Mater. 28 (2016) 50.
[285] T. Terao, C. Zhi, Y. Bando, M. Mitome, C. Tang, D. Golberg, J. Phys. Chem. C 114 (2010) 4340.
[286] J. Chen, X. Huang, B. Sun, Y. Wang, Y. Zhu, P. Jiang, ACS Appl. Mater. Interfaces 9 (2017) 30909.

[287] L. Bai, Z. Zhang, J. Pu, C. Feng, X. Zhao, R. Bao, Z. Liu, M. Yang, W. Yang, Polymer 194 (2020), 122390.
[288] V. Wable, P.K. Biswas, R. Moheimani, N. Aliahmad, P. Omole, A.P. Siegal, M. Agarwal, H. Dalir, Compos. Sci. Technol. 213 (2021), 108941.
[289] J. Chen, H. Wei, H. Bao, P. Jiang, X. Huang, ACS Appl. Mater. Interfaces 11 (2019) 31402.
[290] G. Yang, X. Zhang, D. Pan, W. Zhang, Y. Shang, F. Su, Y. Ji, C. Liu, C. Shen, ACS Appl. Mater. Interfaces 13 (2021) 32285.
[291] J. Chen, X. Huang, B. Sun, P. Jiang, ACS Nano 13 (2019) 337.
[292] L. Fan, S. Zhang, G. Zhao, Q. Fu, Compos. Part A 143 (2021), 106282.
[293] C. Yuan, B. Xie, M. Huang, R. Wu, X. Luo, Int. J. Heat. Mass Transf. 94 (2016) 20.
[294] J. Yuan, X. Qian, Z. Meng, B. Yang, Q. Liu, ACS Appl. Mater. Interfaces 11 (2019) 17915.
[295] J. Geng, Y. Men, C. Liu, X. Ge, C. Yuan, RSC Adv. 11 (2021) 16592.
[296] J. He, H. Wang, Q. Qu, Z. Su, T. Qin, X. Tian, Compos. Part A 139 (2020), 106062.
[297] S.-H. Chung, H. Kim, S.W. Jeong, Carbon 140 (2018) 24.
[298] H. Wang, Z. Huang, J. Li, F. Wang, Z. Feng, H. Tian, H. Zhao, C. Li, Appl. Phys. Lett. 118 (2021), 131903.
[299] M. Liu, S.-W. Chiang, X. Chu, J. Li, L. Gan, Y. He, B. Li, F. Kang, D. Du, Ceram. Int. 46 (2020) 20810.
[300] J. Liu, W. Li, Y. Guo, H. Zhang, Z. Zhang, Compos. Part A 120 (2019) 140.
[301] N. Burger, A. Laachachi, M. Ferriol, M. Lutz, V. Toniazzo, D. Ruch, Prog. Polym. Sci. 61 (2016) 1.
[302] M. Zhou, T. Lin, F. Huang, Y. Zhong, Z. Wang, Y. Tang, H. Bi, D. Wan, J. Lin, Adv. Funct. Mater. 23 (2013) 2263.
[303] L. Zhang, Q. Wei, J. An, L. Ma, K. Zhou, W. Ye, Z. Yu, X. Gan, C.-T. Lin, J. Luo, Chem. Eng. J. 380 (2020), 122551.
[304] X. Shen, Z. Wang, Y. Wu, X. Liu, Y.-B. He, Q. Zheng, Q.-H. Yang, F. Kang, J.-K. Kim, Mater. Horiz. 5 (2018) 275.
[305] L. Zhang, K. Zhou, Q. Wei, L. Ma, W. Ye, H. Li, B. Zhou, Z. Yu, C.-T. Lin, J. Luo, X. Gan, Appl. Energy 233 (2019) 208.
[306] Y.A. Samad, Y. Li, A. Schiffer, S.M. Alhassan, K. Liao, Small 11 (2015) 2380.
[307] M. Qin, Y. Xu, R. Cao, W. Feng, L. Chen, Adv. Funct. Mater. 28 (2018) 1805053.
[308] X. Xu, R. Hu, M. Chen, J. Dong, B. Xiao, Q. Wang, H. Wang, Chem. Eng. J. 397 (2020), 125447.
[309] X. Chen, L.S.K. Lim, W. Yan, F. Guo, Y. Liang, H. Chen, A. Lambourne, X. Hu, ACS Appl. Mater. Interfaces 12 (2020) 16987.
[310] J. Li, X. Zhao, W. Wu, X. Ji, Y. Lu, L. Zhang, Chem. Eng. J. 415 (2021), 129054.
[311] F.E. Alam, W. Dai, M. Yang, S. Du, X. Li, J. Yu, N. Jiang, C.-T. Lin, J. Mater. Chem. A 5 (2017) 6164.
[312] X. Wang, P. Wu, ACS Appl. Mater. Interfaces 9 (2017) 19934.
[313] L. Cao, J. Wang, J. Dong, X. Zhao, H.-B. Li, Q. Zhang, Compos. Part B 188 (2020), 107882.
[314] L. Peng, H. Yu, C. Chen, Q. He, H. Zhang, F. Zhao, M. Qin, Y. Feng, W. Feng, Adv. Sci. 10 (2023) 2205962.
[315] X. Zhou, S. Xu, Z. Wang, L. Hao, Z. Shi, J. Zhao, Q. Zhang, K. Ishizaki, B. Wang, J. Yang, Adv. Sci. 9 (2022) 2103592.
[316] C. Wu, D. Kang, P. Chen, Y. Tai, MEMS thermal flow sensors, Sens. Actuators A 241 (2016) 135.
[317] X. Sun, W. Luo, J. Meng, X. Qing, W. Fu, Y. Shuai, C. Wu, Sens. Actuators A 228 (2015) 69.
[318] S. Lv, M. Liu, W. He, X. Li, W. Gong, S. Shen, Energy Convers. Manag. 207 (2020), 112516.
[319] N.P. Padture, M. Gell, E.H. Jordan, Science 296 (2002) 280.
[320] ransition to sustainable buildings: Strategies and opportunities to 2050, International Energy Agency, Paris 2013.
[321] X. Lu, M.C. Arduini-Schuster, J. Kuhn, O. Nilsson, J. Fricke, R.W. Pekala, Science 255 (1992) 971.
[322] V. Apostolopoulou-Kalkavoura, P. Munier, L. Bergstrom, Adv. Mater. 33 (2020) 2001839.
[323] L. Chen, D. Rende, L.S. Schadler, R. Ozisik, J. Mater. Chem. A 1 (2013) 3837.
[324] B. Notario, J. Pinto, E. Solorzano, J.A. de Saja, M. Dumon, M.A. Rodriguez-Perez, Polymer 56 (2015) 57.
[325] M. Koebel, A. Rigacci, P. Achard, Aerogel-based thermal superinsulation: an overview, J. Sol. -Gel Sci. Technol. 63 (2012) 315.
[326] G. Chen, Phonon heat conduction in nanostructures, Int. J. Therm. Sci. 39 (2000) 471.
[327] S.S. Shrestha, J. Tiwari, A. Rai, D.E. Hun, D. Howard, A.O. Desjarlais, M. Francoeur, T. Feng, Int. J. Therm. Sci. 187 (2023), 108164.
[328] Z. Shao, Y. Wang, H. Bai, A superhydrophobic textile inspired by polar bear hair for both in air and underwater thermal insulation, Chem. Eng. J. 397 (2020), 125441.
[329] J. Zhou, Y.-L. Hsieh, Nano Energy 68 (2020), 104305.
[330] W. Gu, G. Wang, M. Zhou, T. Zhang, G. Ji, ACS Appl. Mater. Interfaces 12 (2020) 48246.
[331] S. Zhao, Z. Zhang, G. Sebe, R. Wu, R.V.R. Virtudazo, P. Tingaut, M.M. Koebel, Adv. Funct. Mater. 25 (2015) 2326.
[332] L.R. Meza, S. Das, J.R. Greer, Science 345 (2014) 1322.
[333] G. Li, M. Zhu, W. Gong, R. Du, A. Eychmuller, T. Li, W. Lv, X. Zhang, Adv. Funct. Mater. 29 (2019) 1900188.
[334] L. Su, H. Wang, M. Niu, X. Fan, M. Ma, Z. Shi, S. Guo, ACS Nano 12 (2018) 3103.
[335] L. Su, H. Wang, M. Niu, S. Dai, Z. Cai, B. Yang, H. Huyan, X. Pan, Sci. Adv. 6 (2020) eaay6689.
[336] X. Zhang, F. Wang, L. Dou, X. Cheng, Y. Si, J. Yu, B. Ding, ACS Nano 14 (2020) 15616.
[337] X. Xu, Q. Zhang, M. Hao, Y. Hu, Z. Lin, L. Peng, T. Wang, X. Ren, C. Wang, Z. Zhao, C. Wan, H. Fei, L. Wang, J. Zhu, H. Sun, W. Chen, T. Du, B. Deng, G. Cheng, I. Shakir, C. Dames, T.S. Fisher, X. Zhang, H. Li, Y. Huang, X. Duan, Science 363 (2019) 723.
[338] H. Wang, X. Zhang, N. Wang, Y. Li, X. Feng, Y. Huang, C. Zhao, Z. Liu, M. Fang, G. Ou, H. Gao, X. Li, H. Wu, Sci. Adv. 3 (2017), e1603170.
[339] J. Yang, K.Y. Chan, H. Venkatesan, E. Kim, M.H. Adegun, J.H. Lee, X. Shen, J. K. Kim, Nano-Micro Lett. 14 (2022) 54.
[340] B.P. Jelle, Energy Build. 43 (2011) 2549.
[341] M. Hamedi, E. Karabulut, A. Marais, A. Herland, G. Nystrom, L. Wagberg, Angew. Chem. Int. Ed. 52 (2013) 12038.
[342] C. Jin, Y. Jiang, T. Niu, J. Huang, J. Mater. Chem. 22 (2012) 12562.
[343] H. Guan, Z. Cheng, X. Wang, ACS Nano 12 (2018) 10365.
[344] J. Zhang, Y. Cheng, C. Xu, M. Gao, M. Zhu, L. Jiang, Adv. Funct. Mater. 31 (2021) 2009349.
[345] R.H. White, Effect of lignin content and extractives on the higher heating value of wood, Wood Fiber Sci. 19 (1987) 446.
[346] J. Song, C. Chen, Z. Yang, Y. Kuang, T. Li, Y. Li, H. Huang, I. Kierzewski, B. Liu, S. He, T. Gao, S.U. Yuruker, A. Gong, B. Yang, L. Hu, ACS Nano 12 (2018) 140.
[347] T. Li, J. Song, X. Zhao, Z. Yang, G. Pastel, S. Xu, C. Jia, J. Dai, C. Chen, A. Gong, F. Jiang, Y. Yao, T. Fan, B. Yang, L. Wagberg, R. Yang, L. Hu, Sci. Adv. 4 (2018) eaar3724.
[348] D. Raps, N. Hossieny, C.B. Park, V. Altstadt, Polymer 56 (2015) 5.
[349] P. Ruckdeschel, A. Philipp, M. Retsch, Adv. Funct. Mater. 27 (2017) 1702256.
[350] X. Zhang, X. Zhao, T. Xue, F. Yang, W. Fan, T. Liu, Chem. Eng. J. 385 (2020), 123963.
[351] Y. Qin, Q. Peng, Y. Zhu, X. Zhao, Z. Lin, X. He, Y. Li, Nanoscale Adv. 1 (2019) 4895.
[352] K. Sakai, Y. Kobayashi, T. Saito, A. Isogai, Sci. Rep. 6 (2016) 20434.
[353] S.D. Kimmins, N.R. Cameron, Adv. Funct. Mater. 21 (2011) 211.
[354] M. Song, J. Jiang, H. Qin, X. Ren, F. Jiang, ACS Appl. Mater. Interfaces 12 (2020) 45363.
[355] J.Y. Lee, M.J. Oh, P.J. Yoo, J. Mater. Chem. C. 9 (2021) 8947.
[356] R. Hu, W. Xi, Y. Liu, K. Tang, J. Song, X. Luo, J. Wu, C.-W. Qiu, Mater. Today 45 (2020) 120.
[357] C. Xu, G.T. Stiubianu, A.A. Gorodetsky, Science 359 (2018) 1495.
[358] L. Xiao, H. Ma, J. Liu, W. Zhao, Y. Jia, Q. Zhao, K. Liu, Y. Wu, Y. Wei, S. Fan, K. Jiang, Nano Lett. 15 (2015) 8365.
[359] J. Mandal, Y. Fu, A.C. Overvig, M. Jia, K. Sun, N.N. Shi, H. Zhou, X. Xiao, N. Yu, Y. Yang, Science 362 (2018) 315.
[360] M.J. Moghimi, G. Lin, H. Jiang, Adv. Eng. Mater. 20 (2018) 1800038.
[361] T. Kim, J.-Y. Bae, N. Lee, H.H. Cho, Adv. Funct. Mater. 29 (2019) 1807319.
[362] Z.J. Coppens, J.G. Valentine, Adv. Mater. 29 (2017) 1701275.
[363] J.H. Ko, D.H. Kim, S.H. Hong, S.K. Kim, Y.M. Song, iScience 26 (2023), 105780.
[364] L. Zhu, A.R. Raman, S. Fan, Proc. Natl. Acad. Sci. U. S. A. 112 (2015) 12282.
[365] M.M. Hossain, B. Jia, M. Gu, Adv. Opt. Mater. 3 (2015) 1047.
[366] S.-Y. Heo, G.J. Lee, H. Kim, Y.J. Kim, S. Ishii, M.S. Kim, T.J. Seok, B.J. Lee, H. Lee, Y.M. Song, Sci. Adv. 6 (2020) eabb1906.
[367] N.N. Shi, C.-C. Tsai, M.J. Carter, J. Mandal, A.C. Overvig, M.Y. Sfeir, M. Lu, C. L. Craig, G.D. Bernard, Y. Yang, N. Yu, Light Sci. Appl. 7 (2018) 37.
[368] D. Xie, Z. Yang, X. Liu, S. Cui, H. Zhou, T. Fan, Soft Matter 15 (2019) 4294.
[369] H. Zhang, K.C.S. Ly, X. Liu, Z. Chen, M. Yan, Z. Wu, X. Wang, Y. Zheng, H. Zhou, T. Fan, Proc. Natl. Acad. Sci. U. S. A. 117 (2020) 14657.
[370] T. Wang, Y. Wu, L. Shi, X. Hu, M. Chen, L. Wu, Nat. Commun. 12 (2021) 365.
[371] T. Li, Y. Zhai, S. He, W. Gan, Z. Wei, M. Heidarinejad, D. Dalgo, R. Mi, X. Zhao, J. Song, J. Dai, C. Chen, A. Aili, A. Vellore, A. Martini, R. Yang, J. Srebric, X. Yin, L. Hu, Science 364 (2019) 760.
[372] A. Yang, L. Cai, R. Zhang, J. Wang, P.-C. Hsu, H. Wang, G. Zhou, J. Xu, Y. Cui, Nano Lett. 17 (2017) 3506.
[373] L. Cai, A.Y. Song, W. Li, P.-C. Hsu, D. Lin, P.B. Catrysse, Y. Liu, Y. Peng, J. Chen, H. Wang, J. Xu, A. Yang, S. Fan, Y. Cui, Adv. Mater. 30 (2018) 1802152.
[374] X. Wang, X. Liu, Z. Li, H. Zhang, Z. Yang, H. Zhou, T. Fan, Adv. Funct. Mater. 30 (2020) 1907562.
[375] S. Zeng, S. Pian, M. Su, Z. Wang, M. Wu, X. Liu, M. Chen, Y. Xiang, J. Wu, M. Zhang, Q. Cen, Y. Tang, X. Zhou, Z. Huang, R. Wang, A. Tunuhe, X. Sun, Z. Xia, M. Tian, M. Chen, X. Ma, L. Yang, J. Zhou, H. Zhou, Q. Yang, X. Li, Y. Ma, G. Tao, Science 373 (2021) 692.
[376] B. Zhu, W. Li, Q. Zhang, D. Li, X. Liu, Y. Wang, N. Xu, Z. Wu, J. Li, X. Li, P. B. Catrysse, W. Xu, S. Fan, J. Zhu, Nat. Nanotechnol. 16 (2021) 1342.
[377] F. Zhao, Y. Guo, X. Zhou, W. Shi, G. Yu, Nat. Rev. Mater. 5 (2020) 388.
[378] L. Kumar, M. Hasanuzzaman, N.A. Rahim, Energy Convers. Manag. 195 (2019) 885.
[379] C. Xu, K.Y. Pu, Chem. Soc. Rev. 50 (2021) 1111.
[380] Y. Hu, Z. Li, T. Lan, W. Chen, Adv. Mater. 28 (2016) 10548.
[381] Q. Zhao, T. Fan, J. Ding, D. Zhang, Q. Guo, M. Kamada, Carbon 49 (2011) 877.
[382] Z. Yang, L. Ci, J.A. Bur, S.-Y. Lin, P.M. Ajayan, Nano Lett. 8 (2008) 446.
[383] K. Mizuno, J. Ishii, H. Kishida, Y. Hayamizu, S. Yasuda, D.N. Futaba, M. Yumura, K. Hata, Proc. Natl. Acad. Sci. U. S. A. 106 (2009) 6044.
[384] H. Shi, J.G. Ok, H.W. Baac, J.J. Guo, Appl. Phys. Lett. 99 (2011), 211103.
[385] Z. Yin, H. Wang, M. Jian, Y. Li, K. Xia, M. Zhang, C. Wang, Q. Wang, M. Ma, Q.-S. Zheng, Y. Zhang, ACS Appl. Mater. Interfaces 9 (2017) 28596.
[386] F.J. Garcia-Vidal, J.M. Pitarke, J.B. Pendry, Phys. Rev. Lett. 8 (1997) 4289.
[387] X. Gao, H. Ren, J. Zhou, R. Du, C. Yin, R. Liu, H. Peng, L. Tong, Z. Liu, J. Zhang, Chem. Mater. 29 (2017) 5777.
[388] N. Xu, J. Li, Y. Wang, C. Fang, X. Li, Y. Wang, L. Zhou, B. Zhu, Z. Wu, S. Zhu, J. Zhu, Sci. Adv. 5 (2019) eaaw7013.

[389] Y. Wang, L. Zhang, P. Wang, ACS Sustain. Chem. Eng. 4 (2016) 1223.
[390] K. Cui, B.L. Wardle, ACS Appl. Mater. Interfaces 11 (2019) 35212.
[391] F. Kinai, F. Sterl, T.V. Tsoulos, K. Weber, H. Giessen, G. Tagliabue, ACS Photonics 7 (2020) 366.
[392] H. Li, L. Wu, H. Zhang, W. Dai, J. Hao, H. Wu, F. Ren, C. Liu, ACS Appl. Mater. Interfaces 12 (2020) 4081.
[393] K. Liu, Q. Jiang, S. Tadepallifit, R. Raliya, P. Biswas, R.R. Naik, S. Singamaneni, ACS Appl. Mater. Interfaces 9 (2017) 7675.
[394] G. Xue, K. Liu, Q. Chen, P. Yang, J. Li, T. Ding, J. Duan, B. Qi, J. Zhou, ACS Appl. Mater. Interfaces 9 (2017) 15052.
[395] C. Chen, Y. Li, J. Song, Z. Yang, Y. Kuang, E. Hitz, C. Jia, A. Gong, F. Jiang, J. Y. Zhu, B. Yang, J. Xie, L. Hu, Adv. Mater. 29 (2017) 1701756.
[396] X. Zhang, L. Yang, B. Dang, Nano Energy 78 (2020), 105322.
[397] Y. Zou, P. Yang, L. Yang, N. Li, G. Duan, X. Liu, Y. Li, Polymer 217 (2021), 123464.
[398] Y. Bian, D. Du, K. Tang, Y. Shen, L. Hao, D. Zhou, X. Wang, Z. Xu, H. Zhang, L. Zhao, S. Zhu, J. Ye, H. Lu, Y. Yang, R. Zhang, Y. Zheng, S. Gu, Adv. Mater. Technol. 4 (2019) 1800593.
[399] J. Liu, Q. Liu, D. Ma, Y. Yuan, J. Yao, W. Zhang, H. Su, Y. Su, J. Gu, D. Zhang, J. Mater. Chem. A 7 (2019) 9034.
[400] Z. Sun, W. Li, W. Song, L. Zhang, Z. Wang, J. Mater. Chem. A 8 (2020) 349.
[401] J. Li, X. Zhou, P. Mu, F. Wang, H. Sun, Z. Zhu, J. Zhang, W. Li, A. Li, ACS Appl. Mater. Interfaces 12 (2020) 798.
[402] L. Ren, X. Yi, Z. Yang, D. Wang, L. Liu, J. Ye, Nano Lett. 21 (2021) 1709.
[403] Y. Chen, G. Zhao, L. Ren, H. Yang, X. Xiao, W. Xu, ACS Appl. Mater. Interfaces 12 (2020) 46653.
[404] P. Sun, W. Zhang, I. Zada, Y. Zhang, J. Gu, Q. Liu, H. Su, D. Pantelic, B. Jelenkovic, D. Zhang, ACS Appl. Mater. Interfaces 12 (2020) 2171.
[405] X. Wang, Q. Liu, S. Wu, B. Xu, H. Xu, Adv. Mater. 31 (2019) 1807716.
[406] Y. Liu, H. Liu, J. Xiong, A. Li, R. Wang, L. Wang, X. Qin, J. Yu, Chem. Eng. J. 427 (2022), 131539.
[407] Z. Liu, Z. Zhou, N. Wu, R. Zhang, B. Zhu, H. Jin, Y. Zhang, M. Zhu, Z. Chen, ACS Nano 15 (2021) 13007.
[408] L. Zhang, B. Tang, J. Wu, R. Li, P. Wang, Adv. Mater. 27 (2015) 4889.
[409] X. Dong, L. Cao, Y. Si, B. Ding, H. Deng, Adv. Mater. 32 (2020) 1908269.
[410] H. Liu, B. Chen, Y. Chen, M. Zhou, F. Tian, Y. Li, J. Jiang, W. Zhai, Adv. Mater. (2023) 2301596.
[411] P. Ying, B. Ai, W. Hu, Y. Geng, L. Li, K. Sun, S.C. Tan, W. Zhang, M. Li, Nano Energy 89 (2021), 106443.
[412] X. Qian, R. Yang, Mater. Sci. Eng. R. 146 (2021), 100642.
[413] M.R.A. Bhatti, A. Kernin, M. Tausif, H. Zhang, D. Papageorgiou, E. Bilotti, T. Peijs, C.W.M. Bastiaansen, Adv. Opt. Mater. 10 (2022) 2102186.
[414] X. Wu, Z. Wu, Y. Wang, T. Gao, Q. Li, H. Xu, Adv. Sci. 8 (2021) 2002501.
[415] Y. Wang, X. Wu, Nano Energy 79 (2021), 105477.
[416] Z. Lei, S. Zhu, X. Sun, S. Yu, X. Liu, K. Liang, X. Zhang, L. Qu, L. Wang, X. Zhang, Adv. Funct. Mater. 32 (2022) 2205790.

Bin Xie is currently a Lecturer in School of Mechanical Science and Engineering, Huazhong University of Science and Technology (HUST). He received his Ph.D. in Engineering Thermophysics from HUST in 2019. His research concentrates on functional thermal materials for electronic packaging and thermal management, from synthesizing materials to understanding their underlying physics.

Weixian Zhao is currently a master student in School of Energy and Power Engineering, HUST. He received his Bachelor's degree from HUST in 2020. His current research focuses on thermal management design and fabrication toward optoelectronics, under the supervision of Prof. Run Hu and Dr. Bin Xie.

Xiaobing Luo is currently the Dean of School of Energy and Power Engineering and the Chinese Co-Dean of Joint School of China-Europe for Clean and Renewable Energy, HUST. He received his Ph.D. in Engineering Thermophysics from Tsinghua University in 2002. Prof. Luo's research areas including extreme thermal management design and devices, optoelectronic device packaging (LED and quantum dots), micropumps.

Run Hu is currently an Associated Professor of School of Energy and Power Engineering, HUST. He received his Ph.D. in Engineering Thermophysics from HUST in 2016. His research focuses on thermal management for electronics and thermal metamaterials.